Cardiff University

PhD Program of the Cardiff School of Chemistry 09/2023

Università degli Studi di Torino

Doctoral School of the University of Torino

PhD Program in Chemical and Materials Sciences XXXIVth Cycle

Paramagnetic Species in Catalysis Research: An EPR investigation into the photochemistry and reactivity of Cr(I) complexes.

David Fioco

Supervisors:

Prof. Damien M. Murphy

Prof. Mario Chiesa

Acknowledgments

I am grateful to the European Union for the funding and support granted us through the Horizon 2020 research and innovation programme under the Marie Skłodowska-Curie grant agreement No 813209.

A special thanks to all those who helped in making this PhD Thesis possible, including but not limited to the amazing people of the EPR groups of Cardiff, Torino and Antwerpen and their supervisors: Prof. Damien M. Murphy, Prof. Mario Chiesa and Prof. Sabine Van Doorslaer.

To my family and friends who are always there for me, whatever physical distance divides us.

In loving memory of my uncle William and great aunt Ugolina who passed away shortly before they could celebrate the conclusion of this endeavour with me.

Abstract

In recent years, chromium complexes bearing a bis(diphenylphosphino) ligand have been widely studied for their potential use as catalysts in ethylene oligomerization. These systems are typically activated using a suitable co-cocatalyst such as triethylaluminium (TEA) or modified methylaluminoxane (MMAO). However, despite their potential use as catalysts and the large amount of research conducted on them to date, there is still no consensus regarding the mechanism of operation, the intermediates and active state of the catalyst and even the actual oxidation state of active chromium species. Whilst Cr(III) centres have dominated the ethylene oligomerization research literature, the Cr(I) analogues have received far less attention (primarily due to their paramagnetism and hence difficulties in characterisation by conventional methods). Considering these Cr(I) display a fascinating photochemical activity (and hence potential for photochemical assisted activation) this sparsity for Cr(I) studies is unusual. As Cr(I) is a paramagnetic metal center, EPR is an ideal choice as the primary investigative technique for these systems.

In this Thesis $[Cr(CO)_4(Ph_2P(C_3H_6)PPh_2)]^+$ (using the 1,3 bis-(diphenylphosphino)-propane ligand $Ph_2P(C_3H_6)PPh_2$ = **dppp**) was found to be converted into a *trans*-$[Cr(CO)_2(dppp)_2]^+$ complex following UV irradiation in dichloromethane (at 365 nm). The intermediate species involved in this transformation, *mer*-$[Cr(CO)_3(\kappa^1\text{-dppp})(\kappa^2\text{-dppp})]^+$, can be identified by EPR following low temperature (140 K) UV radiation. This transformation was found to be wavelength, temperature and concentration dependent. When irradiated with UV light at 380 nm the starting complex only converts to the *trans*-species, with no evidence for formation of the *mer*-complex. When irradiated at low temperature in frozen solution and low concentration, the product from an intramolecular reaction $[Cr(CO)_2(dppp\text{-}\eta^6\text{-arene})]^+$ becomes the main species observed whilst UV irradiation in the presence of 1-hexene was found to produce a stable $[Cr(CO)_3(dppp)(1\text{-hexene})]^+$ complex.

Whilst the common bis-(diphenylphosphino)-propane family of ligands, such as $Ph_2P(C_3H_6)PPh_2$, dominate the literature and this field of study, a novel complex bearing a bis[2-(diphenylphosphino)ethyl]amine pincer ligand (= **PNP**), $[Cr(CO)_3(PNP)]^+$ was synthesized for the first time and examined by EPR and HYSCORE spectroscopy to determine its electronic structure. Similar to the

$Ph_2P(C_3H_6)PPh_2$ ligand and its associated Cr(I) complex, this new pincer type Cr(I) complex can also be activated chemically and photochemically to react with 1-hexene, forming a stable $[Cr(CO)_3(PNP)(1\text{-hexene})]^+$ complex.

The results presented in this work show for the first time that the key step in the activation of the Cr(I) based complexes, namely the removal of the Cr-CO carbonyl groups by TEA or MAO co-catalysts, can potentially be achieved by selective photochemical steps, opening up the possibility for future research opportunities that incorporate UV radiation to enhance or even supplement in a controlled way, the activation and catalysis of these important Cr(I) catalysts for ethylene oligomerisation.

Contents

Chapter 1

Introduction - The Chemistry of Selective Ethylene Oligomerisation

1.1 The Importance of Liner Alpha Olefins (LAO's)

Ethylene is one of the most produced chemicals in the world with annual production figures measured in the hundreds of millions of tons. It is used in a wide array of industrial applications [1] and even plays a significant biochemical role, especially in plants where it acts as hormone, regulating the ripening and development of plants [2]. As a precursor molecule it plays an arguably even larger role following its polymerization, and specifically oligomerization reactions, while its oxide is widely used in many important organic chemistry reactions [3]. Ethylene polymerization is likely the most famous reaction involving ethylene with polyethylene and many other ethylene containing polymers being omnipresent as polymeric materials in consumer industries [4]. The oligomerization reactions of ethylene are used specifically to synthesize short chained alkenes [5] which are then used as precursors and monomers in a variety of applications. These short chain compounds are collectively referred to as **Linear Alpha Olefins** (abbreviated hereafter as LAO's) and have a generic formula of C_XH_{2X} (with chain lengths ranging from C_4-C_{30}). While there is no strict upper limit or boundary between oligomerization and polymerization products, the LAO's are commonly categorized as short (up to C_{18}) and long (up to C_{30}) with the shortest chains (C_4-C_8) accounting for most of the industrial production [5]. 1-butene (C_4), 1-hexene (C_6) and 1-octene (C_8) are the most sought-after compounds (Figure 1.1) produced by oligomerization of ethylene and see widespread use in many industrial applications such as the monomers for polymerization, resins, cosmetics, and fatty acids [6]. Collectively they are commercially important intermediates in the production of detergents (with chain length C_{10}-C_{14}), synthetic lubricants (C_{16}-C_{18}), and in the manufacture of plasticiser alcohols (C_4-C_8 alkenes). The C_4-C_8 fraction (notably 1-hexene) is used as a co-monomer, along with ethylene, in the production of linear low-density polyethylene (LLDPE). This type of polyethylene has a range of applications in many types of plastic products, including the manufacture of plastic

bags, covering of cables and flexible tubing. For this reason, obtaining 1-hexene to act as a precursor for this polymer, through novel catalytic processes, is highly significant and important from an industrial perspective (Scheme 1.1).

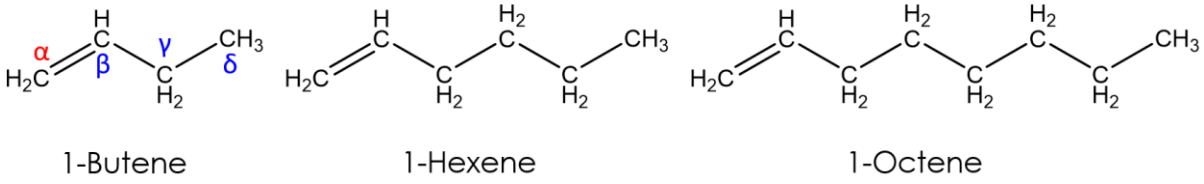

Figure 1.1: Structure of the shortest LAO's: 1-bButene, 1-hexene, 1-octene**.**

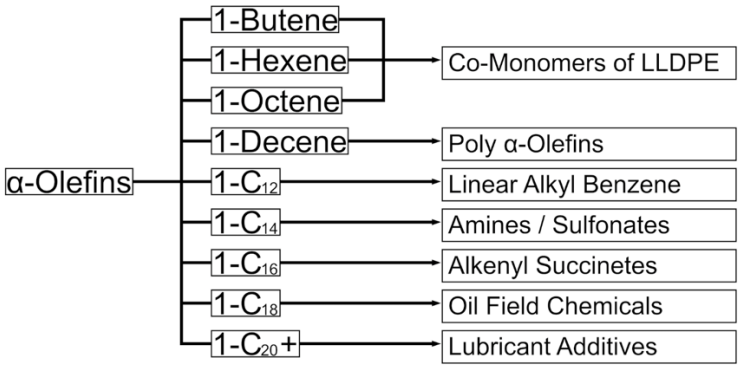

Scheme 1.1: Examples of LAO's uses based on chain length [6].

Historically, LAO's have been synthesized in a variety of ways and some of the more traditional routes have now been discontinued, such as the chlorination / dehydrochlorination reactions of linear paraffins (Figure 1.2) [5].

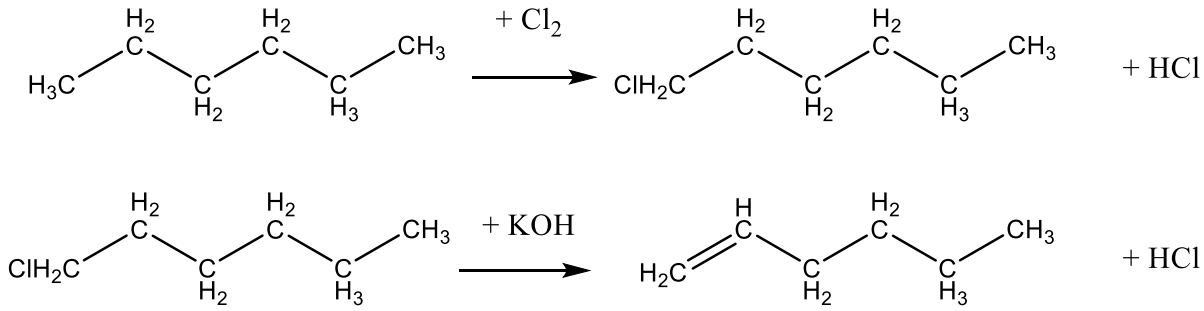

Figure 1.2: Chlorination and base induced dehydrochlorination of an alkane to produce an alkene.

Chlorination and halogenation reactions of alkanes and paraffins are notoriously inefficient processes, prone to producing a wide variety of compounds at different levels of halogenation. This is due to the already halogenated compounds reacting more readily to further halogenation. Thermal cracking of paraffins has also been considered for this process, particularly as long chained solid alkanes such as paraffins (C_{20} to C_{120}) are a by-product of the Fisher-Tropsh process and generally their production exceeds demand. This process also leads to a wide variety of products, including inorganic impurities originating from the Fisher-Tropsh process [7].

The Fisher-Tropsh process [8] was historically used to convert solid hydrocarbons (such as coal) into liquid hydrocarbons for use as fuels. This reaction saw immediate use during World War II. The production of LAO's was not the primary intent of the Fisher Tropsh process but, the process produces a wide range of products from which LAO's products can be separated. The Fisher Tropsh process uses CO (obtained from coal, and later from oil) as the primary feedstock. The gaseous feed of CO and H_2 is reacted with a cobalt based catalyst, namely methylidynetricobaltnonacarbonyl (Figure 1.3).

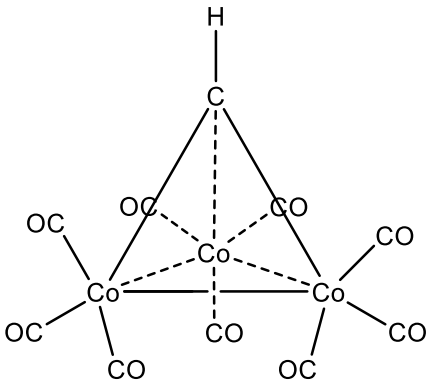

Figure 1.3: Methylidynetricobaltnonacarbonyl, an organocobalt cluster with the formula $HCCo_3(CO)_9$ employed in the Fisher Tropsh Process.

Limiting the scope of our attention to the synthesis of LAO's the stoichiometric formula is given as [9]:

$$(2n+1)\,H_2 + n\,CO \longrightarrow C_nH_{2n+2} + H_2O \qquad (1.1)$$

Compared to ethylene oligomerization processes, odd numbered LAOs can be produced through this path. These processes aren't generally selective towards

specific classes of products but instead follow a Flory–Schulz distribution [10, 11]. This type of distribution is found in several chemical processes linked to chain growth mechanisms such as polymerization and oligomerization.

$$w_a(k) = a^2k(1\text{-}a)^{k\text{-}1} \tag{1.2}$$

In this equation, $w_a(k)$ is the probability mass function while k is the chain length expressed as the number of constituent monomers and a is an empirical factor that describes the concentration of free monomer. In this particular case the output describes the probability of formation for a chain of a specified length. The function has a geometric progression which results in ever diminishing probabilities as the number of monomers included in the chain increases [10, 11].

There are several processes that specifically produce LAO's from the oligomerization of ethylene. Most of these are not selective towards a particular chain length but will produce statistical distributions of LAO's depending on the process type and conditions. Typically, these are reported as being variants of the Ziegler catalyst for ethylene oligomerization in which the modifications preclude the possibility of growing the ethylene chain indefinitely [12].

Industrial standards and preferences make it undesirable for any reaction to have multiple products as these complicate the process and require additional distillation and separation steps which increase cost and complexity. As can be expected there has been a constant push to find innovative and novel catalysts and reaction paths targeted at LAO's of specific chain lengths or, failing that, with as narrow of a distribution as possible [5].

Finally, it is worth noting that the most common method of manufacturing the highly desirable 1-hexene monomer is *via* metal-catalysed oligomerisation of ethylene, as summarised later (sections 1.4-1.6). This is delivered either through a 'full-range' process, resulting in a distribution of LAO's, or through an 'on-purpose' route which selectively produces predominantly 1-hexene. The main commercial full-range producers are Shell, BP Amoco and Chevron Phillips. However, as noted above the distribution of oligomers is inconvenient by industrial standards, and the fractions must be subsequently separated by distillation. It therefore proved essential to develop a catalytic route of selectively producing only the desired chain length. Such 'on-

purpose' routes have been developed, but they are rare and currently the only commercial-scale trimerisation plant is run by Chevron Phillips. There is clearly a need for more research into novel catalysts for this selective reaction, and thus more research is required into the fundamental mechanistic studies of such systems (i.e., the basis of this Thesis).

1.2 The Shell Higher Olefin Process (SHOP)

As the demand for LAO's increased during the second half of the twentieth century, the Shell Higher Olefin Process (SHOP) was proposed as a feasible industrial scale route to satisfy the growing demand. At the time, ethylene was produced as a by-product of hydrocarbon cracking and production had outpaced demand. With the relative availability and affordability of ethylene, attention turned to the use of this raw material as a primary feed stock for oligomerization and polymerization [13]. An early example of a catalytic system for this reaction, promoting early chain termination employs a nickel-phosphine based catalyst (Figure 1.4) [14, 15]. The reaction is typically carried out between 353 K and 393 K at *ca*. 70-140 bar. As this oligomerization reaction progresses by linking C_2 units (ethylene), only even numbered olefins are produced. The statistical distribution of lengths which peaks between C_{12} and C_{18} (40% to 50%) is the fraction most used for the synthesis of fatty acids [16].

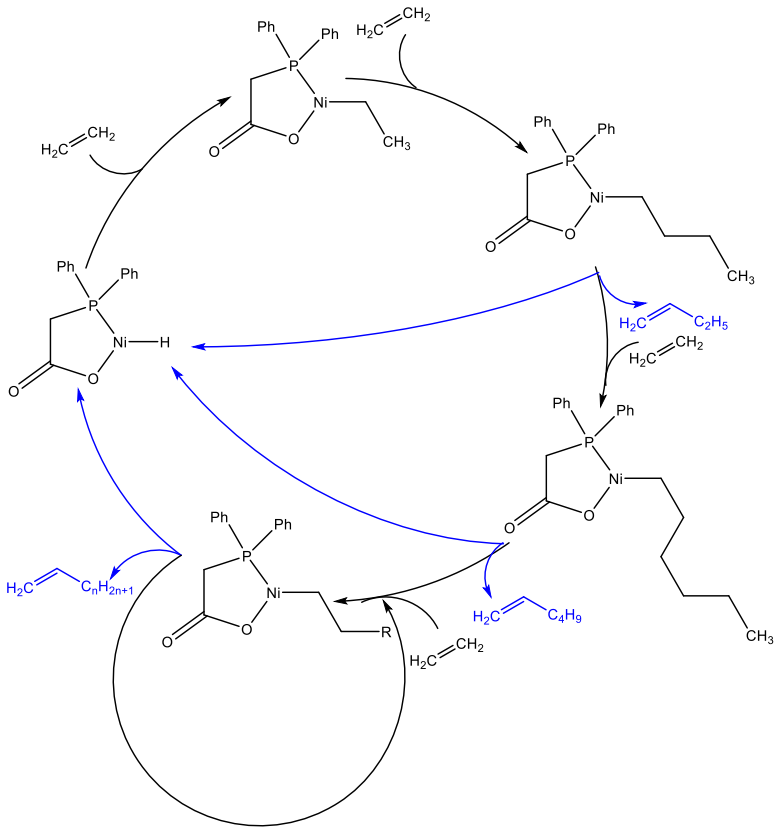

Figure 1.4: Schematic illustration of the Shop process; black = pathways leading to increased chain lengths, blue = termination pathways in which the formed LAO detaches from the Ni centre, restoring the precursor to its original state.

The SHOP process offered a considerable step forward in commercial oligomerisation, greatly improving the ability of chemical industries to direct their focus towards specific chain lengths. However, it still delivers a largely statistical distribution of products, and a separation stage is still necessary. As the highest demand for LAO's lies with its shorter chains, it was desirable to seek alternative catalytic systems to selectively produce these specifically.

1.3 Ethylene Dimerization

Karl Ziegler and Heinz Martin first observed that titanium and zirconium alkoxides can catalyse the oligomerization of ethylene in the presence of $AlEt_3$ (the cocatalyst). This reaction was found to produce 1-butene with high selectivity. Later the process was refined by Chauvin *et al.*, in the Alphabutol process which uses a $Ti(OBu)_4/AlEt_3$ [17, 18]. Zirconium based catalytic systems, similar to the Alphabutol process, are also possible but they appear to be generally slower than the titanium-based systems [19]. Reported selectivities are <90% with the primary competing reaction being the newly

produced 1-butene. When this happens co-dimerization of ethylene and 1-butene occurs which can lead to the formation of 1-hexene and branched hexenes. The easiest solution to this problem is to control the conversion speed and working with high concentration of ethylene so that the co-dimerization is statistically less likely to occur. There has been some dispute over the years over the nature of the reaction pathways with some sources proposing a metalacyclic process or a Cossee-Arlman mechanism, as illustrated below in Figure 1.5 [5, 20, 21].

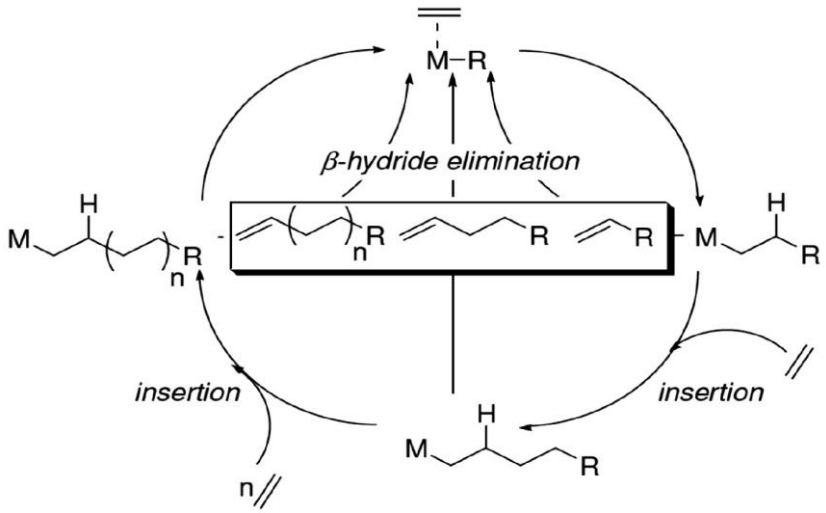

Figure 1.5: Schematic illustration of the Cossee-Arlman mechanism for ethylene oligomerization [21, 6].

Other metals, other than titanium and zirconium, have proven capable of catalysing the dimerization of ethylene, including nickel, platinum, palladium, cobalt, iron and vanadium. They all possess varying degrees of catalytic activity, with nickel having proven the most successful among these to date [20].

1.4 The Phillips System

In 1991 the Chevron-Phillips company patented an industrial process that employs a homogeneous metal catalyst based on chromium or titanium complexes capable of selectively producing 1-hexene [22]. The original Chevron-Phillips catalyst was based on a $CrCl_3$ complex combined with 2,5-dimethylpyrrole in conjunction with a suitable co-catalyst such as triethylaluminium (TEA), methylaluminoxane (MAO) or modified methylaluminoxane (MMAO). These components were combined in solution to generate the active catalyst capable of coordinating two molecules of ethylene (Figure 1.6).

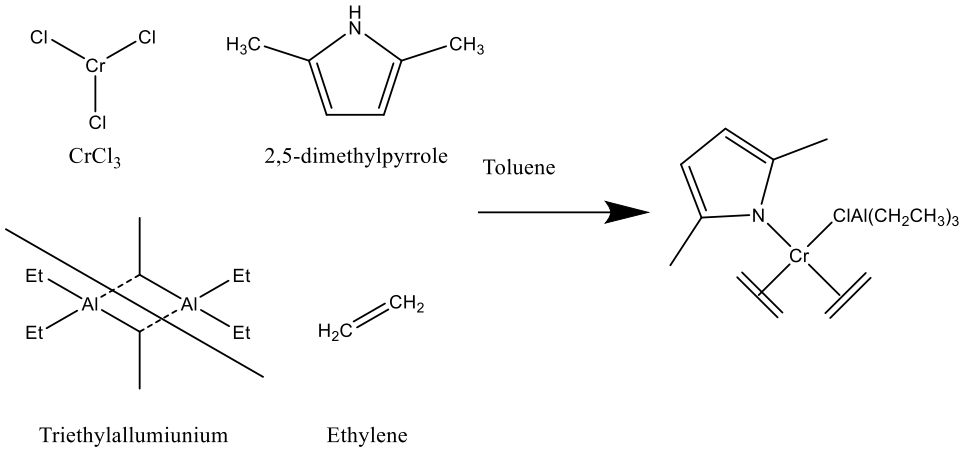

Figure 1.6: The Chevron-Phillips catalyst for ethylene oligomerization [5].

The precise mechanistic pathway for the operating activated catalyst is still poorly understood. What is clear is that all reagents are required to be in large excess relative to the chromium source. The use of the pyrrole ligand and the halogen compound were the main changes to the original Cr-based system proposed by Manyik *et al*., [23]. The discovery of the ligand's effect arose as part of a study into Cr-based pyrrolide complexes. The cyclopentadienyl ligand, which was already used extensively during ethylene polymerisation had been investigated for oligomerisation activity but was only active for polymerisation. However, the pyrrolide ligand being the closest heterocyclic analogue to cyclopentadienyl, both in electronic and steric terms, was also investigated. Other Cr-pyrrolide complexes were tested for ethylene oligomerisation upon activation with triethylaluminium and found to be active and selective towards trimerisation. However, by 1999, the Phillips based system had produced a catalyst yielding 93% overall 1-hexene formation. It incorporated 2,5-dimethylpyrrole as the ligand of choice (Figure 1.6) due to its high light, air and temperature stability. Later on, a Cr(III) 2-ethylhexanoate, diethylaluminium chloride (the halogen compound also increasing the activity and selectivity) and Et_3Al in toluene, was found to deliver this unprecedented selectivity.

Overall, the cocatalysts are essential for the operation of the Chevron-Phillips system and are largely regarded as alkylating agents. Though this is likely their most defining feature, it is not the only property they exhibit, especially in the number of equivalents in most reactions that see their use. It is well understood that these agents also

stabilize the active site and might have a redox effect on the chromium centre. At any rate, they typically generate a wide variety of products.

Another very important consideration, often overlooked in the optimisation steps for these catalysts is the choice of solvent, since it was later shown that toluene could lead to deactivation of the catalyst. Although the precise reasons for this deactivation are still unclear, one possible explanation is provided through EPR spectroscopy. A number of EPR studies have found that a toluene-based Cr-sandwich complex can be formed via η^6-coordination in solution. Cr(I) is a paramagnetic centre with S = 1/2 spin ground state (see Section 1.7). Owing to the presence of the 10-equivalent protons from the two coordinated toluene rings, and 11-line (super)hyperfine pattern was observed in the EPR spectrum (Figure 1.7). The pattern was more easily resolved in the first derivative signal. Whilst it was later shown that this signal could also arise through the coordinated phenyl group of the ligand system, via ligand slippage, this original study thus demonstrated that any leached or free Cr(I) released into solution could be quickly coordinated with toluene, and thus potentially deactivating the system [24].

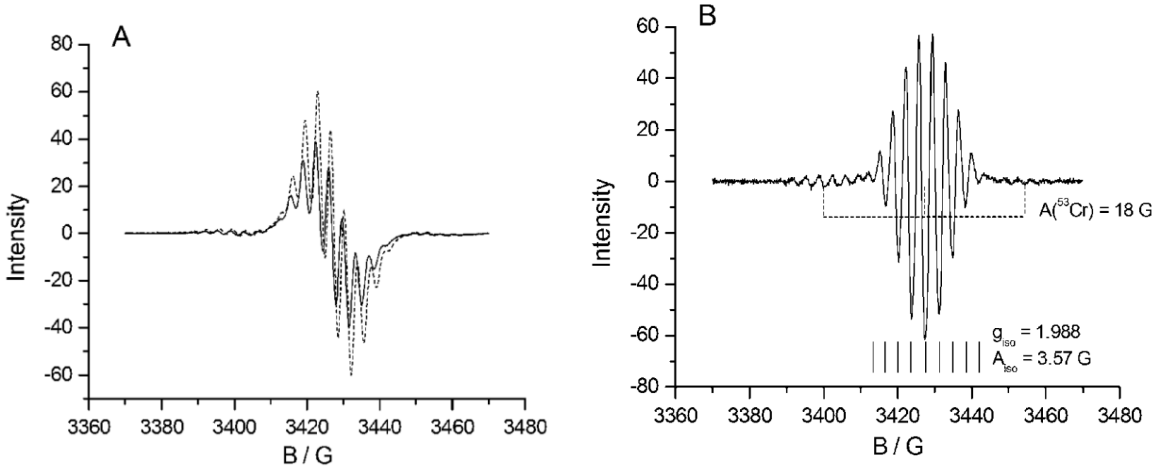

Figure 1.7: (A) Isotropic CW-EPR spectra of $[(PNP)CrCl_2(\mu\text{-}Cl)]_2$ in toluene after 5 min (solid line) and 15 min (dashed line) contact with MMAO; (B) second derivative EPR spectrum after 15 min exposure to MMAO highlighting the observable couplings [24].

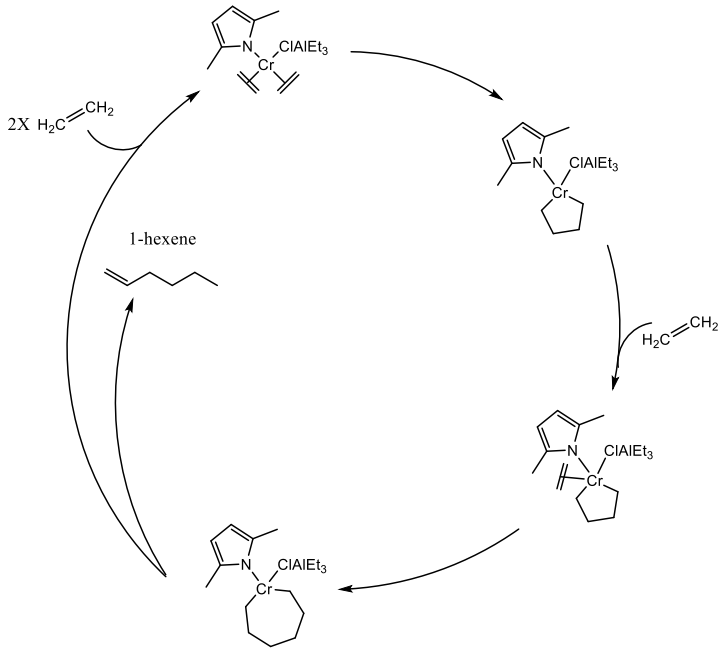

Figure 1.8: Schematic illustration of the proposed metalacyclic pathway for the Chevron-Phillips process [5].

It was originally believed that the metal centre switches between oxidation states of II (when coordinating the two ethylene molecules through their double bond) and IV when the system is coordinating the growing metallacycle [25]. However other research groups proposed the possibility of I and III as the catalytically active centres [26, 27], while others reported on the difficulties of this determination, this will be examined in greater detail in Section 1.7. Agapie *et al*. provided evidence for the metalacyclic pathway using isotopic labelling [28]. An investigation into the oxidation state of the catalytically active Cr-complexes for oligomerisation was conducted by Brukner *et al*. [24]. They evaluated the EPR spectra of $Cr(acac)_3$/PNP mixture (PNP = $Ph_2PN(i\text{-}Pr)PPh_2$; acac = acetylacetonate) in cyclohexane and toluene respectively (Figure 1.7) and evidenced the change in oxidation state from Cr(III) to Cr(I) upon exposure to MMAO. The changes in signal intensity for the Cr-centres was found to be dependent on the nature of the ligand in the order Cr-ac/PNP < Cr-ac << $[(PN\text{-}P)CrCl_2(\mu\text{-}Cl)]_2$ (ac = acetyl). This suggests that a significant percentage of the Cr(III) is rendered EPR silent, either by reduction to Cr(II) or by the formation of anti-ferromagnetic Cr(I) dimers. Introducing ethylene into the Cr-ac/PNP/MMAO reaction mixture leads to the observation of a transient broadening of the EPR signal, which the authors assigned to the PNP-containing Cr(I) complex. This species, only evident

under reaction conditions, was detected for the spectrum assigned to the PNP-free Cr(I) complex. This broadening was believed to be linked to fluctuations of the Cr valence state between +1 and +3 due to a redox cycle. While this was suggestive of a Cr(I) / Cr (III) pathway, it was not believed to be robust enough to make definite conclusions. In the final step 1-hexene is released and two more ethylene molecules enter the coordination sphere. This restores the oxidation state to either I or II and the cycle can begin anew. Through all of this the role of the pyrrolic ring is to alternate between an η^5 and a η^1 configuration to accommodate for changes in the oxidation state in the system.

Manyik *et al*., [23] proposed a new mechanism for the operation of the catalyst which crucially accounted for the unusual rate dependences of 1-hexene formation on temperature and pressure (these were considered to be inconsistent with the expected linear chain growth mechanism). The proposed mechanism required the co-ordination of two ethylene molecules to Cr, followed by metallacyclopentane formation (Figure 1.8). The rate-determining step was assigned as this rearrangement of the co-ordinated alkenes to form a metallacyclopentane, to account for the second order dependence on ethylene pressure. A β-hydrogen transfer from the metallacycle to a third co-ordinated ethylene molecule was suggested with 1-hexene formed *via* a reductive elimination of this intermediate.

Briggs [29] then modified the catalyst system to account for a slightly revised mechanism. In this case, instead of a β-hydrogen transfer to ethylene, insertion of ethylene into the metallacyclopentane was proposed to occur yielding a metallacycloheptane (which is faster than decomposition of the metallacycle to 1-butene). Ring opening was then proposed to occur to form a Cr-hexenyl hydride, which reductively eliminates to yield 1-hexene and the active species again. This ring opening process was suggested to be faster than further ethylene insertion into the metallacycloheptane, which would form a larger ring.

The proposed presence of metallacycles was not unusual, as their existence had previously been evidenced by McDermott *et al*., [30, 31] in the 1970's, thereby adding weight to the Cr-metalacyclic intermediates during the oligomerisation process. It was also shown that the metallacycle intermediates were particularly resistant to β-hydrogen elimination, adding weight to the Briggs' model. Crystal structures of 5- and

7-membered chromacycles were subsequently published, and the 7-membered species decomposed more rapidly than the five-membered chromacycles, producing 1-hexene.

Some debate still remains over the exact decomposition pathway of the metallacycloheptane. A single, concerted step was proposed by Yu and Houk [32] compared to the 2-step route postulated by Briggs [29]. An agostic-assisted β-hydride shift leading directly to the alkene was calculated as the lowest energy pathway for the metallacycloheptane decomposition. Interestingly, this led the authors to suggest an explanation for why dimerisation is disfavoured, *i.e.*, the concerted process cannot occur in the metallacyclopentane due to geometric constraints of the small ring, and the 2-step decomposition mechanism would have to occur instead, which is less favourable than ring expansion followed by the single-step decomposition mechanism.

Throughout all these exploratory mechanistic studies, a wide variety of Cr-based complexes and ligands have been studied. A brief summary of these systems, simply to highlight the diversity of systems used is shown below in Figure 1.9 and Table 1.1.

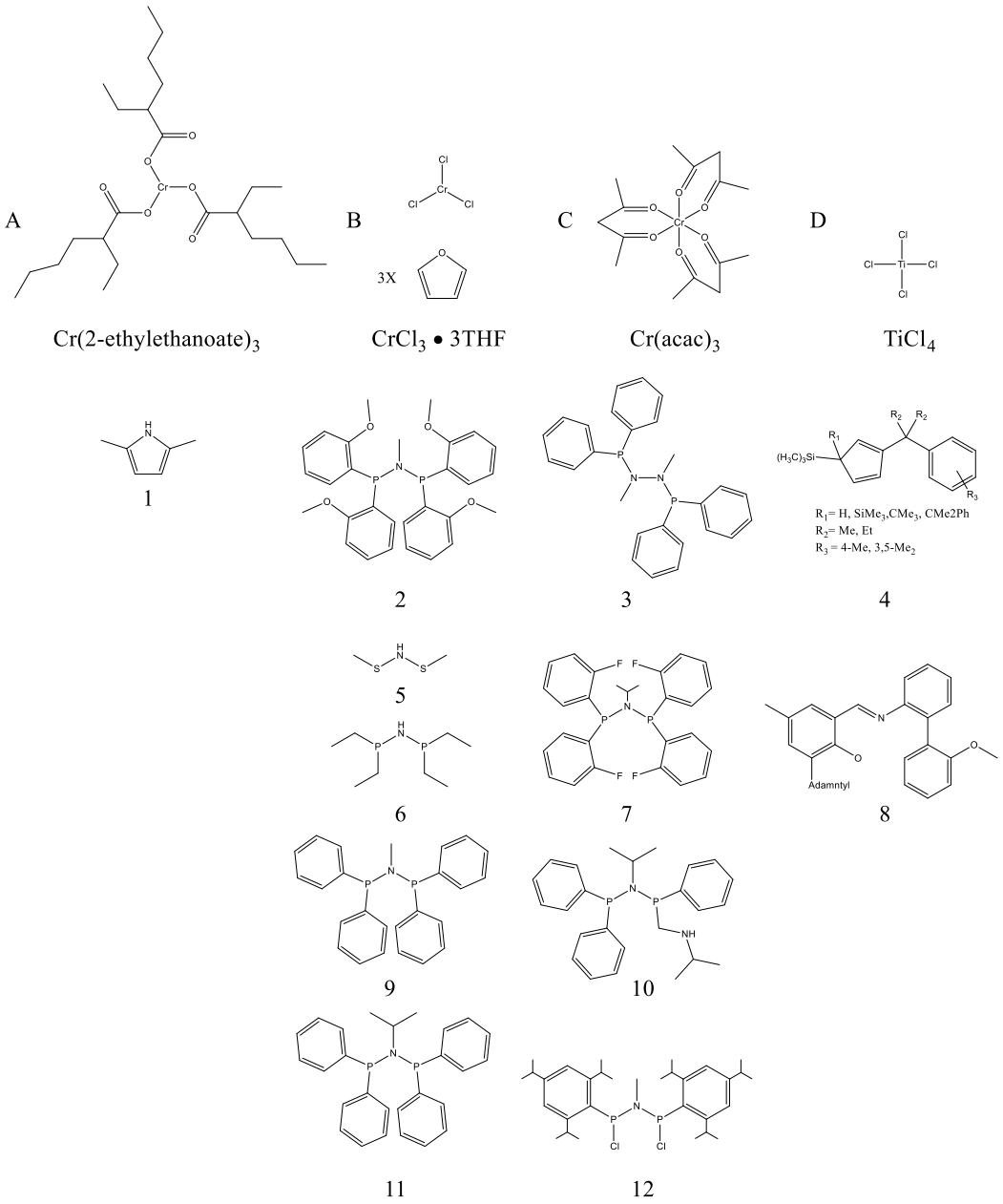

Figure 1.9: A selection of Cr-based complexes and ligands successfully tested for ethylene oligomerization [6].

Precursor	Cocatalyst	Ligand	Products	Ref
A	$AlEt_3$ + $AlEt_2Cl$	1	C_6 = 93 C_8 = 0,3 C_{10} = 6,5 PE = 0,2	[22]
A	$AlEt_3$ + CCl_4	1	C_6 = 93 C_8 = 0,3 C_{10} = 6,5 PE = 0,2	[33]
B	MAO	2	C_6 = 90 C_8 = 1,5 C_{10} = 8,5 PE = -	[34]
D	MAO	4	C_6 = 83 C_8 = ND C_{10} = 14 PE = 1,8	[35]
B		5	C_6 = 95 C_8 = - C_{10} = 4,6 PE = 0,32	[36]
B		6	C_6 = 98 C_8 = - C_{10} = 1,3 PE = 0,7	[37]
B	MAO	9	C_6 = 24,8 C_8 = 59 C_{10} = 14,8 PE = 1,4	[38]
B	MAO	11	C_6 = 16,9 C_8 = 68,3 C_{10} = 13,7 PE = 1,1	[39]
C	MAO	3	C_6 = 25,2 C_8 = 58,8 C_{10} = 13,7 PE = 8	[38]
C	MAO	7	C_4 = 0,25 C_6 = 23,7 C_8 = 70 C_{10} = 5,7 PE = 0,78	[40]
C	MAO	10	C_6 = 28,7 C_8 = 61,8 C_{10} = 8,5 PE = 1	[41]
C	MAO	12	C_6 = 94,6 C_8 = - C_{10} = 4,4 PE = ND	[42]

Table 1.1: A selection of Cr complexes and ligands that have been successfully tested for the purpose of ethylene oligomerization.

One of the limits of the Phillips based catalyst is that the experimental preparation conditions can be very empirical when optimising the reaction conditions. This is also not aided by the varying configurations and quality of the MMAO co-catalyst. As a

result, owing to the complexity in studying the catalyst mixture, the oxidation state of the Cr-centres also remains uncertain with arguments for a Cr (I) / Cr (III) system and for a Cr (II) / Cr (IV) metalacyclic persisting. While the majority of complexes reported in Table 1.1 are based on Cr (III) oxidation state, other oxidation states are also possible (see Section 1.7).

Finally, it is worth noting that titanium-based catalysts are also believed to operate through a metalacyclic process, though unlike chromium-based catalysts there is a degree of uncertainty on whether it operates through a Cossee-Arlman mechanism like ethylene dimerization [21]. Other metals, such as zirconium [43, 44] and tantalum [45, 46] have also been tested for this purpose.

1.5 Chromium Diphosphazane ($R_2PN(R)PR_2$) Complexes

As stated in the last section, the original Phillips catalyst employed a chromium source in conjunction with 2,5-dimethylpyrrole and a co-catalyst such triethylaluminium or modified methylaluminoxane. However, in the early 2000's this was the only homogeneous ethylene oligomerization process available that was fully commercialised. Nevertheless, in the subsequent years many research groups considered other variations on the ligand structure responsible for stabilising the Cr-centres. The vast array of ligands used was reviewed by Dixon *et al.*, providing a very timely picture on the state of research as of 2003 and the truly remarkable avenues of research pursued to obtain a better catalytic system [47].

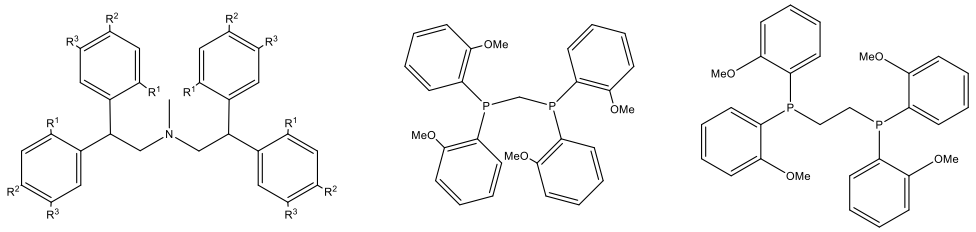

1: R^1 = MeO, R^2 = R^3 = H
2: R^1 = Et, R^2 = R^3 = H
3: R^1 = R^3 = H, R^2 = MeO
4: R^1 = R^3 = MeO, R^2 = H
5: R^1 = MeO, R^2 = H, R^3 = F

6 **7**

$CrCl_3$ + MAO + $(PhOMe)_2P)_2NMe$ = ? → One or more catalytically active species

Figure 1.10: Illustration of the varying ligand structures used in the study of Cr-based oligomerisation, with some combinations showing no activity. Figure adapted from [34].

Among these numerous ligands used (Figure 1.10) the mixed P and N donor system attracted the most attention, notably the diphosphazane ligands ($R_2PN(R)PR_2$). The use of this class of ligands was not new, having been employed in conjunction with both palladium and nickel as polymerization catalysts in the past [48, 49]. However, when applied in combination with chromium, the resulting complex proved to be remarkably effective with reported selectivities of >99% and productivities as high as $>10^6$ g/gCr h (when used in combination with MAO). While investigating the mechanistic aspects of the reaction (i.e., specifically whether the reaction progresses through a Cossee-Arlman pathway or through a metallacycle pathway) it was noted that when the reaction was left to progress for a long enough time, the newly formed 1-hexene product could also participate in the oligomerization reaction forming small amounts of branched dodecenes. Similarly, if 1-butene was used, the process could produce branched octenes. At the time, the authors were unable to establish the catalytically active form of the catalyst. Even the use of $CrCl_2$ resulted in some catalytically active species which lead the authors to speculate that at least some of the species formed are the same. This makes it difficult to conclude which species are catalytically active and indeed which Cr oxidation state is operative in the reaction; a recurring problem for systems based on the Phillips catalyst (see section 1.7).

McGuiness *et al*., also reported a variation of this system which used a different ligand. In this case the chromium source was combined with the ligand as a separate stage allowing for the isolation of the pre-catalyst as a distinct complex. A representative example of such a Cr-complex is shown in Figure 1.11 for a PNP pincer ligand. The activation step of this complex for ethylene oligomerisation was carried out with MAO [37]. The reported values indicated that using cyclohexyl rings resulted in substantial formation of polyethylene while using aromatic rings and ethyl substituents yielded better results. The amount of MAO used for the activation ranged from 100 equivalents to over 600 per unit of chromium.

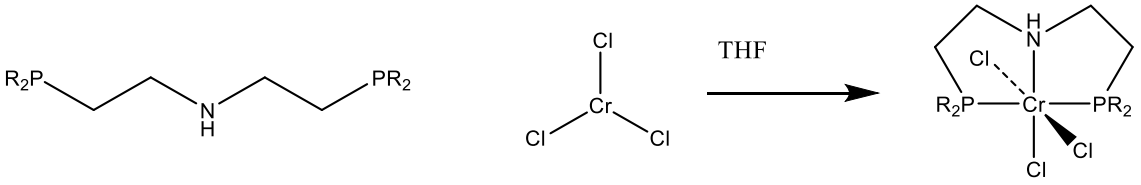

R = phenyl, cyclohexyl, ethyl

Figure 1.11: Synthesis of $[CrCl_3(PR_2C_2H_4)_2NH]$ complex, adapted from [37].

By synthesising and isolating the pre-catalyst before the reaction, allowed for better control of the reaction conditions. Nevertheless, the identity of the resulting catalytically activated complex in solution following the addition of the cocatalysts (such as MAO, MMAO or TEA), remains elusive.

Another more recent variation on this ligand system was based on the S analogues (Figure 1.12) [36]. The most interesting aspect of this change is that it appears to dramatically reduce the number of equivalents of cocatalyst used with reported ranges of 30 to 100.

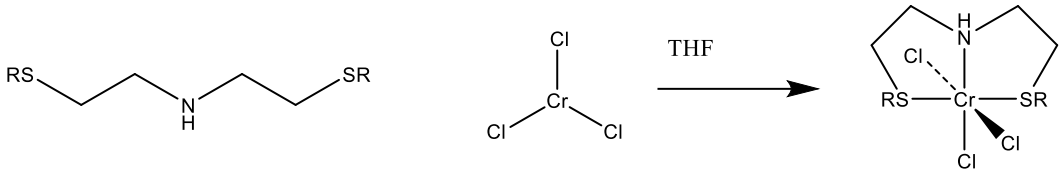

R = methyl, ethyl, n-Butyl, n-decyl

Figure 1.12: Synthesis of $[CrCl_3(SRC_2H_4)_2NH$ adapted from [36].

1.6 Chromium (I) Species in Ethylene Oligomerization – the role of the oxidation & spin state

One of the most versatile attributes of the transition metals is their ability to exist in multiple oxidation states and thereby facilitate a wide range of catalytic reactions. The variable oxidation states of chromium are no exception. In all of the above sections, the emphasis was placed on the historical developments in the ancillary ligands, such as $[CrCl_3(PR_2C_2H_4)_2NH]$ which demonstrated excellent catalytical activity for ethylene trimerisation, and little attention was devoted to the key oxidation states involved in the reactions. The primary driver for developing these catalysts was of course the need to scale up the ethylene oligomerization process, rather than providing a thorough mechanistic understanding first. Indeed, in some of the ethylene oligomerization processes, it was also known that the reaction was effective regardless of whether the oxidation state of the pre-catalyst was Cr(I) or Cr(III). Hence less attention was devoted to the primary oxidation state nor the need to strictly control (stabilise) a particular oxidation state. As a result, the Cr(I) pre-catalysts have attracted little attention to date. These chromium (I) centres have a d^5 electron configuration and are generally less stable (and notoriously more air and moisture sensitive) than other Cr-

oxidation states [50]. As the metalacyclic reaction is believed to occur either through a Cr(I) / Cr(III) or Cr (II) / Cr (IV) redox couple, it is essential to better understand how the reaction proceeds via the starting oxidation states of Cr (notably I or III).

Of interest to this project is the Cr (I) complex $Cr(CO)_4((PPh_2)_2N(CH(CH_3)_2))]^+$ (Figure 1.13) which has demonstrated high catalytic activity, using a TEA cocatalyst, similar to the well-known system $[Cr(CO)_4((P(PhOCH_3)_2)_2NCH_3))]^+$ [51].

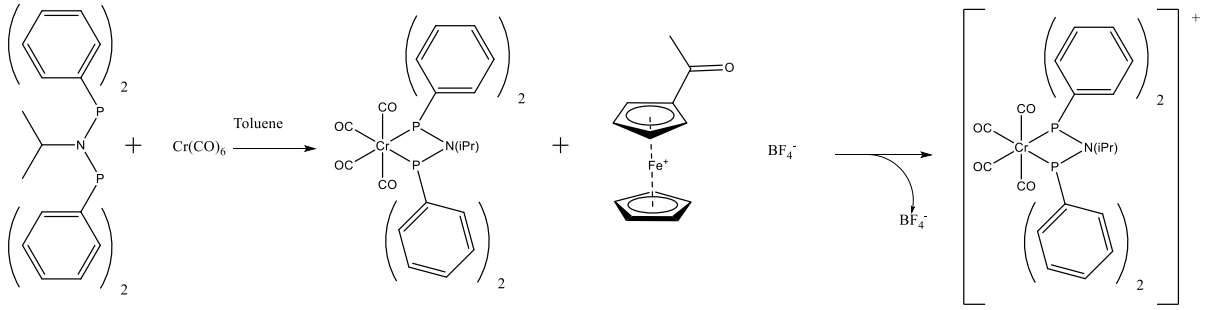

Figure 1.13: Synthesis of $[Cr(CO)_4((PPh_2)_2N(CH(CH_3)_2))]^+$ starting from $Cr(CO)_6$ and acetylferrocenium-tetrafluroborate, adapted from [51].

These Cr(I) complexes are made using the neutral Cr(0) complex ($Cr(CO)_6$) as a precursor. This volatile compound will readily react with the desired PNP ligand (Figure 1.13) in toluene to form the Cr(0) version of the desired complex, which in turn can be oxidized to the Cr(I) counterpart.

Rucklidge *et al.*, also reported on this same complex for tetramerization of ethylene, albeit with different counterion and redox agent [52]. In a previous study by the same group, it was found that $[B(C_6F_5)_4]$ with TEA can effectively replace MAO for ethylene oligomerization [53]. However, the lifespan of the catalytically active system was found to be significantly shortened, and this was attributed to TEA degrading $[B(C_6F_5)_4]$. As a result $[Al(OC(CF_3)_3)_4]^-$ (tetrakis[perfluoro-tert-butoxy]aluminate) was considered as an alternative, as it is less degradable by agents such as TEA and is a very large, non-coordinating anion [54]. Owing to their interest in studying the role of the oxidation state in the mechanism, they synthesized a Cr(I) version of the complex rather than a Cr(III) complex (Figure 1.14).

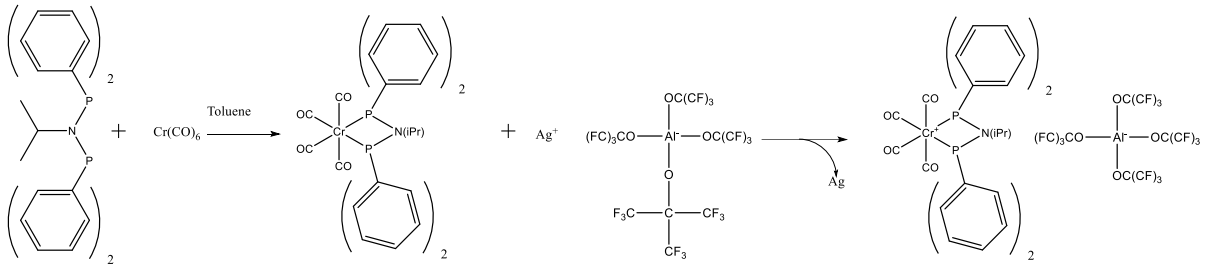

Figure 1.14: Synthesis of $[Cr(CO)_4((PPh_2)_2N(iPr)_2))]^+$ from $Cr(CO)_6$ and $[Al(OC(CF_3)_3)_4]^-$ acetylferrocenium-tetrafluroborate, adapted from [52].

These Cr(I) complexes still required large excesses of a cocatalyst to function as a catalyst for oligomerization, similar to the Cr(III) counterparts. The cocatalysts TEA, MAO and MMAO are believed to be necessary as scavengers to remove the carbonyl ligands from the pre-catalyst and are also believed to play some role in stabilizing the active species. A study by Carter *et al.* highlights the effect of increasing amount of TEA catalyst as it interacts with the $[Cr(CO)_4((PPh_2)_2N(iPr)_2))]^+$ and found that as -CO groups are removed the ligand undergoes a configuration change to coordinate through its aromatic rings, first in a piano-stool configuration and then, with at least 10 equivalents of TEA through a sandwich complex [55]. Similar findings were also found for $[Cr(CO)_4((PPh_2(C_3H_6)PPh_2)]^+$ [56, 57]. More on this will be covered in Chapter 4.

As mentioned earlier 4, several attempts to elucidate the redox couple response for the oligomerization reaction (*e.g.*, Cr(II) / Cr (IV) [25, 58], Cr(I) / Cr (III) [26, 27] or even Cr (III) / Cr (V)) have all been reported [59]. In theory the oxidation state, and crucially for Cr(I) the spin state (see below), can be relatively easily determined by EPR spectroscopy. However, the observer is often detecting the stable resting state of the catalyst as opposed to the transient active state, so great care must always be exercised when interpreting the results of the experimental EPR data. The precise effect caused by the addition of MAO, MMAO or TEA, which changes the oxidation state of the Cr pre-catalyst has never been completely understood [47, 5, 60]. In many cases the number of equivalents required for activation is substantial (*e.g.*, 600 equivalents of MAO per unit of chromium [37] and 30 being considered a low amount [36]). It is certain that the activator (cocatalyst) plays a variety of roles, which can decarbonylate the complex (thus creating the necessary coordination sites for ethylene) and stabilizing the chromium complex. It is indeed possible that the effect of

the cocatalyst is limited to these two steps alone, especially under the typically employed experimental conditions (excess reagent).

Traditionally, NMR is the tool of choice when investigating the reaction mechanism of homogeneous transition metal-based catalysts. However, in the presence of paramagnetic species, NMR spectroscopy is not a suitable technique (*i.e.,* while paramagnetic NMR techniques exist, these are often more difficult and less well resolved than the more traditional NMR of diamagnetic systems) [61]. The presence of the paramagnetic Cr species often renders NMR redundant in oligomerisation studies. By comparison, EPR (Chapter 2) is an ideal system, to probe such reactions [62]. Moreover, whilst EPR is the perfect tool to investigate the oxidation state changes of the Cr-based catalysts, it can also uncover any changes in spin state of the catalyst. To understand how this occurs, a very brief overview of Cr coordination chemistry will be presented [63].

For many years Crystal Field Theory (CFT) was used as an approximation to explain the geometry and properties of many complexes. While Ligand Field Theory has largely supplanted this theory, it still sees frequent use due to its simplicity in predicting how the electrons of a metal centre will act in the presence of ligands, and in turn the observed spin state of the metal centre. In its simplest interpretation, CFT assumes the ligands act as point charges (typically negative) which will repel the electrons around the metal centre. A single atom, isolated in an ideal vacuum will have complete degeneracy of all its orbitals of the same type, thus all *d* orbitals of an atom will have exactly the same amount of energy. This degeneracy is lost when the atom is perturbed by the presence of the ligands. In the case of an octahedron, the d_{xy}, d_{xz} and d_{yz} (t_{2g}) orbitals are stabilized by this interaction and thus considered bonding orbitals. The $d_{x^2-y^2}$ and d_{z^2} (e_g) orbitals increase in energy and destabilize the complex making them anti-bonding orbitals. Hund's rule describes that electrons in energetically degenerate orbitals will fill these orbitals preserving the maximum multiplicity. When these orbitals are no longer degenerate, two possible electron configurations result:

- High spin: if the splitting between the energy levels t_{2g} and e_g is small enough, the stabilization effect of having the highest multiplicity possible will be

preserved and thus the complex will have the maximum number of unpaired electrons.

- Low spin: if the splitting between the energy levels t_{2g} and e_g is large enough to overcome Hund's multiplicity rule, all electrons will first fill the t_{2g} orbital and only once this has been completely filled will the e_g be filled. This means that the multiplicity will be lower than what Hund's rule predicts.

The two main factors that contribute to this are the oxidation state of the metal (higher oxidation states have typically larger gaps than lower oxidation states) and the nature of the ligand. Ligands such as carbonyls and phosphines that are on the high end of the spectrochemical series and are capable of forming retro-donation (a stabilizing interaction between an anti-bond orbital of the ligand and one of the bonding orbitals of the metal) have been observed to have high gaps between t_{2g} and e_g thus strongly favouring low spin complexes.

Moving away from this idealized version of coordination chemistry one also needs to factor in other effect such as the Jahn-Teller distortion affecting our octahedral systems. The Jahn-Teller effect is an empirically discovered spontaneous symmetry breaking property which plays a significant role in transition metal and coordination chemistry both at a molecular level and in solid structures. As mentioned earlier for the CFT coordination, when degeneracy is removed from a system, the energy levels of the orbitals affected by this change are perturbed with some moving to lower values (stabilised) and others increasing in energy (destabilized). What makes this perturbation advantageous is that for many configurations of the d orbitals it is possible to fill the stabilised orbitals while leaving the destabilised orbitals empty. The stability gained is often enough to fuel spontaneous changes in configurations of an octahedral system so that one of its axes will be either elongated or shortened. These changes can vary from significant to very minute and thermally accessible. As the Jahn-Teller effect plays a direct role in establishing the total electron it is possible to not only end up with a different spin value than originally expected but to observe spin configuration alterations with changes in temperature and coordination environment.

Accounting for all of these factors in a static system can be challenging but it usually does not pose an insurmountable obstacle to scientific investigation. A reaction system such as the one found in the metalacyclic process simultaneously has multiple species

in equilibrium, transient intermediates and a variety of magnetic properties with the potential of having diamagnetic molecules and paramagnetic molecules in a variety of spin systems, all of which are interacting both chemically and magnetically. Under these conditions, finding a specific spectroscopic technique that can highlight all of the possible species simultaneously can quickly turn into an impossibility. Even just accounting for the species that have fast relaxation properties is a challenge because these are only detectable at near 0 K temperatures, well below what would be considered as valid reaction conditions.

Additionally, the Cr(I) complex proposed to be catalytically active comprised only a minor amount of total Cr present. The presence of EPR silent species made the authors very cautious about drawing too many conclusions from their experiment but it still was an important effort to further delve into this persistent enigma.

1.7 Photochemistry of Cr(I) Complexes

Any molecule or complex can interact with electromagnetic radiation to promote an electron from its ground state to an excited state. In the case of many transition metals, the energy to promote one such transition often falls in the visible range, giving these complex colours. Chromium can exist in a wide variety of oxidation states and in an even wider variety of colours, which ultimately are responsible for its name. This extends to electrons involved in metal-ligand bonds and it is thus possible to break a chemical bond applying light of the appropriate wavelength [63]. Chromium – carbonyl bonds in particular have long been known to be photolabile, but the most detailed study performed was by Compton *et al.* [64]. A comprehensive tutorial review on the subject of photochemistry of metal carbonyls was recently published by Turner *et al.* [65].

Rieger *et al.* later performed a photochemistry and EPR study on the Cr(I) complexes *fac*-$[Cr(CO)_3(Ph_2P(CH_2)_2PPh_2)_2]^+$ and *fac*-$[Cr(CO)_3(Ph_2As(CH_2)_2AsPh_2)_2]^+$ based on previous observations that other complexes of similar geometry could be transformed into their *mer*- counterparts with removal a carbonyl ligand (see Figure 1.15) [66]. Previous studies had shown that this *fac*- and *mer*- conformation change could be induced electrochemically [67, 68].

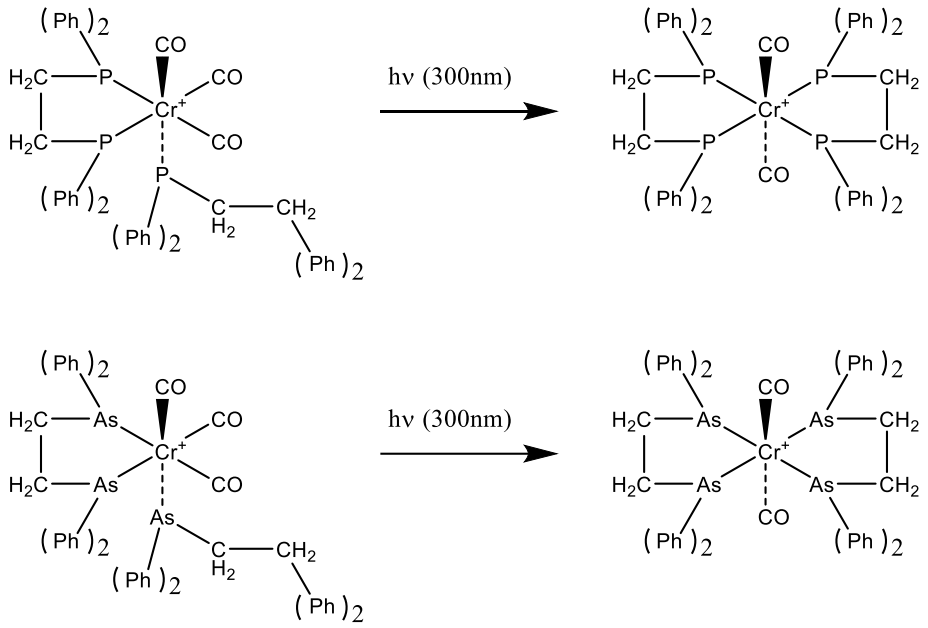

Figure 1.15: adapted from [66], photochemically induced transformation of *fac*-$[Cr(CO)_3(Ph_2P(CH_2)_2PPh_2)_2]^+$ and *fac*-$[Cr(CO)_3(Ph_2As(CH_2)_2AsPh_2)_2]^+$ to *mer*-$[Cr(CO)_2(Ph_2P(CH_2)_2PPh_2)_2]^+$ and *mer*-$[Cr(CO)_2(Ph_2As(CH_2)_2AsPh_2)_2]^+$ with irradiation at **300 nm**.

Luckham *et al*. [69] studied the photochemical properties of $[Cr(CO)_4(Ph_2P(C_3H_6)Ph_2)]^+$ complex ($Ph_2P(C_3H_6)Ph_2$ = dppp) in dichloromethane using CW-EPR spectroscopy. The room temperature irradiation with UV light induced a rapid transformation of $[Cr(CO)_4(dppp)]^+$ into trans-$[Cr(CO)_2(dppp)_2]^+$. On the other hand, when irradiating between temperatures of 77 K to 120 K it was reported that an intermediate species, *mer*-$[Cr(CO)_3(\kappa^1\text{-dppp})(\kappa^2\text{-dppp})]^+$ could be detected. The reaction is believed to progress through an intermolecular pathway and will be further explored in Chapter 4.

1.8 Project Aims

The chemistry of chromium-based ethylene oligomerization catalysis has been the subject of numerous studies to date and remains an active field of research. However, whilst its successes for oligomerization are undeniable, there remains some outstanding uncertainties about the reaction mechanism, notably the oxidation state of the catalyst under operating conditions. This issue is first observed following the addition of a cocatalyst (such as TEA, MAO and MMAO) to the Cr(I) containing solution, whereby the deep blue colouration of the liquid is immediately changed to

brown or colourless. This is accompanied by a change in the oxidation state of the Cr species, as observed by EPR. It remains unclear whether the loss in EPR signal intensity is due to the formation of diamagnetic species (*e.g.*, Cr(II) centres) or EPR silent states (*e.g.*, Cr(I)-Cr(I) dimers) [24]. TEA, MAO and MMAO are far from ideal cocatalysts both due to their inherent chemical properties and the number of equivalents per mole of chromium that need to be used. From a chemical point of view, these agents are toxic and pyrophoric making them a safety hazard [70]. From the point of view of the more modern standards of atom economy [71] and green chemistry [72] the very high number of equivalents of co-catalyst required per mole of chromium leads to excessive amounts of industrial waste. This waste, in the form of alkyl-aluminium salts, cannot be reused.

Whilst the definitive role played by the cocatalyst remains to be revealed, it is clear that the decarbonylation of the Cr(I) centre is crucial to this step. As section 1.7 briefly reveals, many Cr-carbonyl complexes can undergo decarbonylation photochemically. It is most surprising then that the use of UV radiation as a means of “co-activating” the Cr(I) based precatalysts have never previously been explored. The notion of “co-activating” here represents the idea that UV radiation could be used to remove the CO groups from the Cr centres, and thereby working in partnership with potentially lower equivalents of cocatalyst which would complete the CO scavenging step. This would represent a significant breakthrough in the field of ethylene oligomerization, if the activation step can be executed through a photochemical pathway or that potentially photochemistry could be used to drastically diminish the quantity of activator agent required.

Therefore, the primary aim and motivation of this work is to explore the use of photochemistry ‘activation’ to initiate the reactivity in a series of well-known Cr(I) precatalysts and more broadly demonstrate the utility of EPR spectroscopy to unravel the complex oxidation state changes and structural rearrangements that occur in these Cr(I) complexes.

Bibliography

[1] K. M. Sundaram, M. M. Shreehan and O. F. Olszewski, Ethylene, Wiley, 2010.

[2] K. L. Wang, H. Li and J. R. Ecker, “Ethylene biosynthesis and signaling networks,” *Plant Cell,* vol. 14, 2002.

[3] J. E. McMurry, Organic Chemistry 9th Edition, Cenegage.

[4] G. Odian, Principles of Polymerization, Wiley, 2004.

[5] D. S. McGuinness, “Olefin oligomerization via metallacycles: Dimerization, trimerization, tetramerization, and beyond,” *Chemical Reviews,* vol. 111, no. 3, pp. 2321-2341, 2011.

[6] T. Gopal, “Catalytic tri- and tetramerization of ethylene: a mechanistic overview,” *Catalysis Reviews,* pp. 1-56, 2022.

[7] A. de Klerk, “Thermal Cracking of Fischer-Tropsch Waxes,” *Industrial & Engineering Chemistry Research,* vol. 46, no. 17, pp. 5516-5521, 2007.

[8] F. Fischer and H. Tropsch, Process for the production of paraffin-hydrocarbons with more than one carbon atom, US1746464A, 1926.

[9] A. de Klerk, E. Furimsky and J. J. Spivey, Catalysis in the Refining of Fischer-Tropsch Syncrude, Royal Chemistry Society, 2010.

[10] P. J. Flory, “Molecular Size Distribution in Linear Condensation Polymers,” *Journal of the American Chemical Society,* vol. 58, no. 10, pp. 1877-1885, 1936.

[11] G. V. Schulz, “Über die Beziehung zwischen Reaktionsgeschwindigkeit und Zusammensetzung des Reaktionsproduktes bei Makropolymerisationsvorgängen,” *Zeitschrift für Physikalische Chemie,* vol. 30B, no. 1, pp. 379-398, 1935.

[12] O. Novaro, S. Chow and P. Magnouat, “Mechanism of oligomerization of α-olefins with Ziegler-Natta catalysts,” *Journal of Catalysis,* vol. 41, no. 1, pp. 91-100, 1976.

[13] K. Wilhelm, “Oligomerization of Ethylene to α-Olefins: Discovery and Development of the Shell Higher Olefin Process (SHOP),” *Angewandte Chemie International Edition,* vol. 52, no. 48, pp. 12455-12744, 2013.

[14] B. Reuben and H. Wittcoff, “The SHOP process: An example of industrial creativity,” *Journal of Chemical Education,* vol. 65, no. 7, pp. 605-607, 1988.

[15] K. Weissermel and H.-J. Arpe, Industrial Organic Chemistry, VCH Verlags Gesellschaft, 1997.

[16] P. Khun, D. Sémeril, D. Matt, M. J. Chetcuti and P. Lutz, “Structure-reactivity relationships in SHOP-type complexes: Tunable catalysts for the oligomerisation and polymerisation of ethylene,” no. 5, pp. 515-528, 2007.

[17] A. Forestière, H. Olivier-Bourbigou and S. L., *"Oil Gas Sci. Technol." Revue de l'IFP,* vol. 64, pp. 649-667, 2009.

[18] D. Commereuc, Y. Chauvin, J. Gaillard, J. Léonard and J. Andrews, “Dimerize ethylene to butene-1,” *Hydrocarbon Process,* vol. 63, no. 11, 1984.

[19] A. W. Al-Sa'doun, “Dimerization of ethylene to butene-1 catalyzed by Ti(OR')4-AlR3,” *Applied Catalysis A: General,* vol. 105, no. 1, pp. 1-40.

[20] K. P. Bryliakov and A. A. Antonov, “Recent progress of transition metal based catalysts for the selective dimerization of ethylene,” *Journal of Organometallic Chemistry,* no. 867, pp. 55-61, 2018.

[21] P. Cossee, “Ziegler-Natta Catalysis I. Mechanism of Polymerization of α-Olefins with Ziegler-Natta Catalysts,” *J. Catal.,* no. 3, pp. 80-88, 1964,.

[22] W. K. Reagen and B. K. Conroy, “Chromium Compounds and Uses Thereof.,” *Patent,* p. EP0416304A2, 1991.

[23] R. M. Manyik, W. E. Walker and T. P. Wilson, “A soluble chromium-based catalyst for ethylene trimerization and polymerization,” *Journal of Catalysis,* vol. 47, no. 2, pp. 197-209, 1977.

[24] A. Brückner, J. K. Jabor, A. E. McConnell and P. B. Webb, “Monitoring structure and valence state of chromium sites during catalyst formation and ethylene oligomerization by in situ EPR spectroscopy,” *Organometallics,* vol. 15, no. 3849-3856, p. 27, 2008.

[25] W. J. Van Rensburg, C. Grové, J. P. Steynberg, K. B. Stark, J. J. Huyser and P. J. Steynberg, “A DFT Study toward the Mechanism of Chromium-Catalyzed Ethylene Trimerization,” *Organometallics,* vol. 23, no. 6, pp. 1207-1222, 2004.

[26] A. Jabri, C. B. Mason, Y. Sim, S. Gambarotta, T. J. Burchell and R. Duchateau, “Isolation of single-component trimerization and polymerization chromium catalysts: The role of the metal oxidation state,” *Angewandte Chemie - International Edition,* vol. 47, no. 50, pp. 9717-9721, 2008.

[27] I. Vidyaratne, G. B. Nikiforov, S. I. Gorelsky, S. Gambarotta, R. Duchateau and I. Korobkov, “Isolation of a Self-Activating Ethylene Trimerization Catalyst,” *Angewandte Chemie,* vol. 121, no. 35, pp. 6674-6678, 2009.

[28] T. Agapie, S. J. Schofr, J. A. Labinger and J. E. Bercaw, “Mechanistic Studies of the Ethylene Trimerization Reaction with Chromium-Diphosphine Catalysts: Experimental Evidence for a Mechanism Involving Metallacyclic Intermediates,” *Journal of the American Chemical Society,* vol. 126, no. 5, pp. 1304-1305, 2004.

[29] J. R. Briggs, “The selective trimerization of ethylene to hex-1-ene,” *Journal of the Chemical Society, Chemical Communications,* no. 11, pp. 674-675, 1989.

[30] J. X. McDermott, J. F. White and G. M. Whitesides, “Preparation and Thermal Decomposition of Platinum(II) Metallocycles,” *Journal of the American Chemical Society,* vol. 95, no. 13, pp. 4451-4452, 1973.

[31] J. X. McDermott, J. F. White and G. M. Whitesides, “Thermal Decomposition of Bis(phosphine)platinum(II) Metallocycles,” *Journal of the American Chemical Society,* vol. 98, no. 21, pp. 6521-6528, 1976.

[32] Z. X. Yu and K. N. Houk, “Why trimerization? Computational elucidation of the origin of selective trimerization of ethene catalyzed by [TaCl3(CH3)2] and an agostic-assisted hydride transfer mechanism,” *Angewandte Chemie - International Edition,* vol. 42, no. 7, pp. 808-811, 2003.

[33] H. Urata, A. Aoshima and S. Nishimura, “Process for Producing α-Olefin Oligomer.,” *US6133495A,* 2000.

[34] A. Carter, S. A. Cohen, N. A. Cooley, A. Murphy, J. Scutt and D. F. Wass, “High Activity Ethylene Trimerisation Catalysts Based on Diphosphine Ligands,” *Chemical Communications,* vol. 2, no. 8, p. 858–859, 2002.

[35] P. J. W. Deckers, B. Hessen and J. H. Teuben, “Catalytic Trimerization of Ethene with Highly Active Cyclopentadienyl-Arene Titanium Catalysts.,” *Organometallics,* vol. 21, no. 23, p. 5122–5135, 2002.

[36] D. S. McGuinness, P. Wasserscheid, W. Keim, D. Morgan, J. T. Dixon, A. Bollmann, H. Maumela, F. Hess and U. Englert, “First Cr(III)-SNS Complexes and Their Use as Highly Efficient Catalysts for the Trimerization of Ethylene to 1-Hexene,” *Journal of American Chemical Society,* vol. 125, no. 18, p. 5272–5273, 2003.

[37] D. S. McGuinness, P. Wasserscheid, W. Keim, C. Hu, U. Englert, J. T. Dixon and C. Grove, “Novel Cr-PNP complexes as catalysts for the trimerisation of ethylene,” *Chemical Communications,* vol. 3, no. 3, pp. 334-335, 2003.

[38] A. Bollmann, K. Blann, J. T. Dixon, F. M. Hess, E. Killian, H. Maumela, D. S. McGuinness, D. H. Morgan, A. Neveling, S. Otto, M. Overett, A. M. Z. Slawin, P. Wasserscheid and S. Kuhlmann, “Ethylene Tetramerization: A New Route to Produce 1-Octene in Exceptionally High Selectivities., 126 (45),,” *J Am Chem Soc,* vol. 126, no. 45, p. 14712–14713, 2004.

[39] M. J. Overett, K. Blann, A. Bollmann, J. T. Dixon, F. Hess, E. Killian, H. Maumela, D. H. Morgan, A. Neveling and S. Otto, “Ethylene Trimerisation and Tetramerisation Catalysts with Polar-Substituted Diphosphinoamine Ligands,” *Chemical Communications,* vol. 5, no. 622, 2005.

[40] X. Gao, C. A. G. Carter, L. FanLee and D. Henderson, “Amino Phosphine,” *US7994363B2,* 2011.

[41] S. Peitz, N. Peulecke, B. H. Müller, A. Spannenberg, H. J. Drexler, U. Rosenthal, M. H. Al-Hazmi, K. E. Al-Eidan, A. Wöhl and W. Müller, “Heterobimetallic Al-Cl-Cr Intermediates with Relevance to the Selective Catalytic Ethene Trimerization Systems Consisting of CrCl3(THF) 3, the Aminophosphorus Ligands Ph2PN(R)P(Ph)N(R)H, and Triethylaluminum,” *Organometallics,* vol. 30, no. 8, p. 2364–2370, 2011.

[42] M. Höhne, N. Peulecke, K. Konieczny, B. H. Müller and U. Rosenthal, “Chromium-Catalyzed Highly Selective Oligomerization of Ethene to 1-Hexene with N,N-Bis[Chloro(Aryl)Phosphino]Amine Ligands.,” *ChemCatChem,* vol. 9, no. 13, p. 2467–2472, 2017.

[43] M. Wang, H. Zhu, K. Jin, D. Dai and L. Sun, “Ethylene oligomerization by salen-type zirconium complexes to low-carbon linear α-olefins,” *Journal of Catalysis,* vol. 220, no. 2, pp. 392-398, 2003.

[44] M. Khamiyev, A. Khanmetov, V. Amir Reza, R. Aliyeva, K. Hajıyeva-Atayi, Z. Akhundova and G. Khamiyeva, “Zirconium Catalyzed Ethylene Oligomerization,” *Applied Organometallic Chemistry,* vol. 34, no. 2, 2020.

[45] T. Agapie, “Selective ethylene oligomerization: Recent advances in chromium catalysis and mechanistic investigations,” *Coordination Chemistry Reviews,* vol. 255, no. 7-8, pp. 861-880, 2011.

[46] J. Petit, L. Magna and N. Mézailles, “Alkene oligomerization via metallacycles: Recent advances and mechanistic insights,” *Coordination Chemistry Reviews,* vol. 450, p. 214227, 2022.

[47] J. T. Dixon, M. J. Green, F. M. Hess and D. H. Morgan, “Advances in selective ethylene trimerisation - A critical overview,” vol. 689, no. 23, pp. 3641-3668, 2004.

[48] S. J. Dossett, A. A. Gillon, G. Orpen, J. S. Fleming, P. G. Pringle, D. F. a. Wass and J. M. D., “Steric activation of chelate catalysts: Efficient polyketone catalysts based on four-membered palladium(II) diphosphine chelates,” *Chemical Communications,* vol. 2, no. 8, pp. 699-700, 2001.

[49] N. A. Cooley, S. M. Green, D. F. Wass, K. Heslop and a. P. G. P. A. Guy Orpen, “Nickel Ethylene Polymerization Catalysts Based on Phosphorus Ligands,” *Organometallics,* vol. 20, no. 23, p. 4769–4771, 2001.

[50] P. H. Rieger, “Electron paramagnetic resonance studies of low-spin d5 transition metal complexes,” *Coordination Chemistry Reviews,* Vols. 135-136, no. C, pp. 203-286, 1994.

[51] L. E. Bowen, M. F. Haddow, A. G. Orpen and D. F. Wass, “One electron oxidation of chromium N, N-bis(diarylphosphino)amine and bis(diarylphosphino)methane complexes relevant to ethene trimerisation and tetramerisation,” *Journal of the Chemical Society. Dalton Transactions,* vol. 4, no. 11, pp. 1160-1168, 2007.

[52] A. J. Rucklidge, D. S. Mcguinness, R. P. Tooze, A. M. Z. Slawin, J. D. A. Pelletier, M. J. Hanton and P. B. Webb, “Ethylene Tetramerization with Cationic Chromium(I) Complexes,” *Organometallics,* vol. 26, no. 10, pp. 2782-2787, 2007.

[53] D. S. McGuinness, M. Overett, R. P. Tooze, K. Blann, J. T. Dixon and A. M. Slawin, “Ethylene tri- and tetramerization with borate cocatalysts: Effects on activity, selectivity, and catalyst degradation pathways,” *Organometallics,* vol. 26, no. 4, pp. 1108-1111, 2007.

[54] I. R. A. Krossing, “Chemistry with weakly-coordinating fluorinated alkoxyaluminate anions: Gas phase cations in condensed phases?,” *Coordination Chemistry Reviews,* vol. 250, no. 21-22, pp. 2721-2744, 2006.

[55] E. Carter, K. J. Cavell, W. F. Gabrielli, M. J. Hanton, A. J. Hallett, L. E. McDyre, J. A. Platts, D. M. Smith and D. M. Murphy, “Formation of [Cr(CO)x(Ph2PN(i

Pr)PPh 2)]+ structural isomers by reaction of triethylaluminum with a chromium N,N -Bis(diarylphosphino)amine complex [Cr(CO) 4(Ph2PN(i Pr)PPh2)]+: An EPR and DFT investigation," *Organometallics,* vol. 32, no. 6, pp. 1924-1931, 2013.

[56] L. E. McDyre, E. Carter, K. J. Cavell, D. M. Murphy, J. A. Platts, K. W. B. D. Sampford, W. F. Gabrielli and M. J. Hanton, "Intramolecular formation of a CrI(bis-arene) species via TEA activation of [Cr(CO)4(Ph2P(C3H 6)PPh2)]+: An EPR and DFT investigation," *Organometallics,* vol. 30, no. 17, pp. 4505-4508, 2011.

[57] L. E. McDyre, T. Hamilton, D. M. Murphy, K. J. Cavell, W. F. Gabrielli, M. J. Hanton and D. M. Smith, "A cw EPR and ENDOR investigation on a series of Cr(i) carbonyl complexes with relevance to alkene oligomerization catalysis: [Cr(CO)4L] + (L = Ph2PN(R)PPh2, Ph2P(R)PPh 2)," *Dalton Transactions,* vol. 39, no. 33, pp. 7792-7799, 2010.

[58] D. H. Morgan, S. L. Schwikkard, J. T. Dixon, J. J. Nair and R. Hunter, "The Effect of Aromatic Ethers on the Trimerisation of Ethylene using a Chromium Catalyst and Aryloxy Ligands," *Advanced Synthesis and Catalysis,* vol. 345, no. 8, pp. 939-942, 2003.

[59] N. Meijboom, C. J. Schaverien and A. G. Orpen, "Organometallic Chemistry of Chromium(VI): Synthesis of Chromium(VI) Alkyls and Their Precursors. X-ray Crystal Structure of the Metallacycle Cr(NtBu)2{o-(CHSiMe3)2C6H4}," *Organometallics,* vol. 9, no. 3, pp. 774-782, 1990.

[60] O. L. Sydora, "Selective Ethylene Oligomerization," *Organometallics,* vol. 38, no. 5, pp. 997-1010, 2019.

[61] F. H. Köhler, Paramagnetic Complexes in Solution: The NMR Approach, eMagRes, 2011.

[62] S. A. Bonke, T. Risse, A. Schnegg and A. Brückner, "In situ electron paramagnetic resonance spectroscopy for catalysis," *Nature Reviews Methods Primers,* vol. 1, no. 1, 2021.

[63] G. L. Miessler, P. J. Fischer and D. A. Tarr, Inorganic Chemistry: Pearson New International Edition, Pearson Higher Ed, 2013.

[64] R. G. Compton, R. Barghout, J. C. Eklund, A. C. Fisher, S. G. Davies, M. R. Metzler, A. M. Bond, R. Colton and J. N. Walter, “Photoelectrochemistry of some organochromium carbonyl compounds,” *Journal of the Chemical Society, Dalton Transactions,* no. 24, pp. 3641-3646, 1993.

[65] J. J. Turner, M. W. George, M. Poliakoff and R. N. Perutz, “Photochemistry of transition metal carbonyls,” *Chemical Society Reviews,* vol. 51, no. 13, pp. 5300-5329, 2022.

[66] A. L. Rieger and P. H. Rieger, “EPR Study of Photochemical Reactions of fac- and mer-[Cr(CO) 3 (η 1-L 2)(η 2-L 2)] + (L 2) Bidentate Phosphine, Arsine, or Phosphonite Ligand),” *Organometallics,* vol. 21, no. 26, pp. 5868-5873, 2002.

[67] A. M. Bond, R. Colton and J. Jackowski, “Electrochemical and chemical oxidation of pi-bonded [bis(diphenylarsino)methane]chromium and-molybdenum dicarbonyl complexes,” *Inorganic Chemistry,* vol. 18, no. 7, pp. 1977-1985, 1979.

[68] A. Blagg, S. W. Carr, G. R. Cooper, I. D. Dobson, J. B. Gill, D. C. Goodall, B. L. Shaw, N. Taylor and T. Boddington, “A mechanistic study on complexes of type mer-[Cr(CO) 3 (η 2 -L–L)(σ-L–L)](where L–L = Ph 2 PCH 2 PPh 2 , Ph 2 PNHPPh 2 , or Ph 2 PNMePPh 2) using spectroscopic and convolutive electrochemical techniques,” *J. Chem. Soc., Dalton Trans.,* vol. 135, no. 6, pp. 1213-1221, 1985.

[69] S. L. J. Luckham, A. Folli, J. A. Platts, E. Richards and D. M. Murphy, “Unravelling the Photochemical Transformations of Chromium(I) 1,3 Bis(diphenylphosphino), [Cr(CO)4(dppp)]+ , by EPR Spectroscopy,” *Organometallics,* vol. 38, no. 12, pp. 2523-2529, 2019.

[70] S. Yoshihiko, O. Ken, A. Miyako, T. Kohichi and M. Takehiro, “Reaction hazards of triethylaluminum under closed conditions,” *Journal of Loss Prevention in the Process Industries,* vol. 24, no. 5, pp. 656-661, 2011.

[71] R. A. Sheldon, “Atom efficiency and catalysis in organic synthesis,” *Pure and Applied Chemistry,* vol. 72, no. 7, pp. 1233-1246, 2007.

[72] M. Hatice and B. Leonie, “Getting the Terms Right: Green, Sustainable, or Circular Chemistry?,” *Macromol. Chem. Phys.,* vol. 223, no. 13, 2022.

Chapter 2
EPR Theory

2.1 Introduction to Electron Paramagnetic Resonance Spectroscopy

Quantum mechanics is, with little argument, one of the most important discoveries in the history of physics and completely revolutionized how humankind conceives of the building blocks of the universe. Among the phenomena observed in quantum mechanics with no classical counterpart we have quantum Spin [1]. Quantum Spin can be defined as an intrinsic angular momentum that many of the known fundamental particles of the standard model possess, in the field of chemistry the relevant particles are the electron, proton and neutron [2]. For an electron, the Spin quantum number is the fourth number needed for a complete description of its state, while bound within an atom (with the other being the Principal quantum number, Azimuthal quantum number and Magnetic quantum number). These tell us which orbital the electron is occupying and are the origin of such notations as $3d^5\ 4s^1$ for the ground state of chromium.

Particles with half-integer spin values (such S = 1/2 for the electron) follow a Fermi-Dirac distribution and are called Fermions. Two or more Fermions cannot share all quantum numbers which is what ultimately limits the capacity of orbitals and is the origin of the Pauli Exclusion principle which limits the capacity of each subshell to 2. In the event of two electrons occupying the same subshell the two spins will align in anti-parallel fashion (up and down), with their magnetic moments cancelling each other out. It is a well-established fact of classical physics that a charge in motion or rotation will give rise to a magnetic field, thus the combination of electronic quantum spin and charge gives rise to the magnetic properties of many materials.

Electron Paramagnetic Resonance (EPR) spectroscopy can be applied to all those materials and systems in which at least one electron remains unpaired and thus it can be probed through the application of an external magnetic field (B_0) which is conventionally assumed to be orientated along the z axis. While the required presence

of paramagnetic electrons makes it impossible to run EPR spectroscopy of every material, it remains a powerful technique to probe a variety of systems, including but not limited to, organic radicals, transition-metal ions, inorganic radicals, biological samples, photoexcited molecules, point defects in crystals and radiation damage. EPR is also being used in the budding field of quantum computing. This section is based on the following references [3, 4, 5, 6].

In the case of S = 1/2 the number of possible configurations is $2S$+1 corresponding to projections along a quantization axis identified by the quantum numbers m_s = +1/2 and -1/2 (spin up, $|\alpha\rangle$, and spin down, $|\beta\rangle$). In the absence of an external magnetic field these are energetically equivalent and defined as degenerate. The magnetic dipole moment of an electron that emerges from spin angular momentum is $\boldsymbol{\mu}_s$:

$$\boldsymbol{\mu}_S = -g_e \mu_B . \mathbf{S} \tag{2.1}$$

where, g_e is the free electron g-factor (g_e = 2.0023), μ_B is the Bohr magneton ($\mu_B = e\hbar/2m_e$ = 9.274 x 10^{-24} JT^{-1}) and **S** is the spin angular momentum.

When the degeneracy of the system is broken by introducing an external magnetic field, B_0 assumed to be along the z axis (often referred to as laboratory axis), the m_s states are now considered as either parallel or antiparallel to this magnetic field.

$$\mu_S = -g_e \mu_B m_s \tag{2.2}$$

The relative energy, E, of the two m_s states is then given by:

$$E = -\boldsymbol{\mu}_s \cdot \boldsymbol{B} = g_e \mu_B m_s B_0 = \pm \frac{1}{2} g_e \mu_B B_0 \tag{2.3}$$

The splitting of the electron spin energy level into two levels in the presence of a magnetic field is called the Zeeman effect, and the interaction of an electron magnetic moment with an external applied magnetic field is called the electron Zeeman interaction (Figure 2.1).

In an EPR experiment, a spin transition is promoted by the absorption of a quantum of microwave radiation energy according to Eq. 2.4, which describes the resonance condition.

$$\Delta E = h\nu = E_2' - E_1' = g_e \mu_B B_0 \qquad (2.4)$$

where ν is the radiation frequency. The EPR experiment is therefore based on the absorption of electromagnetic radiation, which is usually in the microwave frequency region, by a paramagnetic sample placed in a magnetic field.

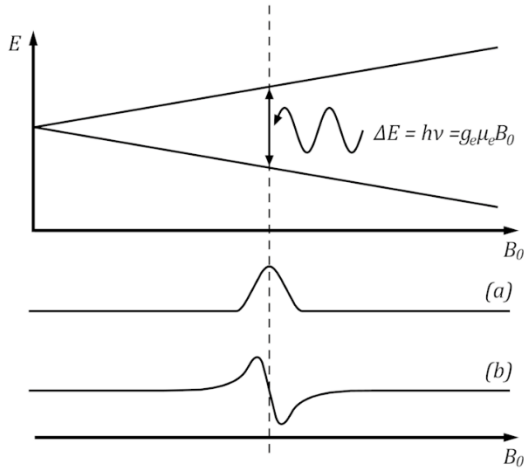

Figure 2.1: representation of the electron Zeeman effect and resonance condition. The energy gap increases linearly with the magnetic field. At resonance condition, the absorption of microwave energy leads to an electron spin flip resulting in an EPR signal that can be presented either in (a) absorption or (b) 1st derivative mode. Adapted from ref. [7].

In the usual experimental setup, one considers samples of many electron spins ($\approx 10^{12}$), statistically distributed in the α and β states according to a Maxwell-Boltzmann statistical distribution (Eq. 2.5).

$$\frac{N_\alpha}{N_\beta} = exp\left(-\frac{g\mu_B B_0}{k_B T}\right) \qquad (2.5)$$

Where k_B is Boltzmann's constant which is equal to 1.3806 x 10^{-23} JK^{-1}, T is the absolute temperature and N_α and N_β are the spin populations characterized by the m_s values +1/2 and -1/2, respectively. At room temperature in the magnetic field of an X-band spectrometer there is an excess of β spins over the α spins of 1/1000. This small excess is enough for the microwave absorption to overcome the emission and to make possible the observation of an EPR absorption signal.

2.2 Electron Spin in Atoms and Molecules

In a real chemical system, the electron angular momentum has two contributions: one arises from the electron spin, and another one arises from the motion of the electron within its orbital. However, in molecular and crystalline systems the orbital angular momentum is quenched (its average is zero), and the electron angular momentum in the absence of spin–orbit coupling is to first order, only due to spin. The effect of spin–orbit coupling is to restore a small amount of orbit contribution, which results in a deviation $\Delta g = g - g_e$ of the g factor from the free electron value entering in Equation 2.4. This has two important consequences: 1) is the shift of the resonance field intensity from the value corresponding to the free electron spin, 2) since the spin-orbit coupling has different efficiency along different directions, g is no longer a scalar but becomes a 3×3 matrix.

In its eigenspace the g tensor can be diagonalized to give three values for the principal axes (g_x, g_y and g_z)

$$\boldsymbol{g} = \begin{pmatrix} g_{xx} & g_{xy} & g_{xz} \\ g_{yx} & g_{yy} & g_{yz} \\ g_{zx} & g_{zy} & g_{zz} \end{pmatrix} \Longrightarrow \boldsymbol{g}_{diagonal} = \begin{pmatrix} g_{xx} & 0 & 0 \\ 0 & g_{yy} & 0 \\ 0 & 0 & g_{zz} \end{pmatrix} \tag{2.6}$$

Because Δg depends on the spin–orbit coupling, its value is large for metal complexes, due to the large spin-orbit coupling constant of heavy atom nuclei, while for organic free radicals containing only light atoms, the spin–orbit interaction is small, and so is the deviation of g from the free electron value. In the same way, the anisotropy of g contains important information on the local symmetry of the paramagnetic species and can be measured by recording the EPR spectra of a single crystal, where the paramagnetic species are in fixed orientations, by rotating the crystal in the spectrometer's magnetic field. The anisotropy of g can also be recovered in disordered (powder) samples (see section 2.3.3), while in liquids, because of rapid molecular tumbling, the g factor anisotropy is averaged out and a mean g value g_{iso} is measured.

$$g_{iso} = \frac{g_x + g_y + g_z}{3} \tag{2.7}$$

Moreover, in a real chemical system the electron magnetic moment can interact with the magnetic moment associated to nuclei possessing a nuclear spin $I \neq 0$. This interaction is called hyperfine interaction and results in the splitting of the resonance line based on the value of I and the number of interacting nuclei.

A quantitative description of such interactions is based on the quantomechanical description of the interaction of electron and nuclear spins with a magnetic field and their hyperfine interaction. A basic outline of the quantum mechanics needed for the description of the EPR is provided in the following sections.

2.3 The Spin Hamiltonian

In quantum mechanics, to each mechanical quantity is associated an operator, which acts on a state function by transforming it into another one. There are particular cases where an operator corresponding to a mechanical property acting upon a state function has the effect of multiplying the function by a constant. In such a case the state is said to be an eigenstate of that particular operator (property) and the constant is called its eigenvalue. In that state the property considered has a definite value equal to the eigenvalue. The Hamiltonian is the operator used to extract information on the energy of the system and its solutions represent the possible energy eigenvalues of that system. Thus, when we define the Spin Hamiltonian, we are analysing the energy states associated with the electron spin. The Hamiltonian can be factorized to account for a variety of possible contributions.

$$\widehat{H}_{total} = \widehat{H}_{EZ} + \widehat{H}_{NZ} + \widehat{H}_{HFI} + \widehat{H}_{NQI} + \widehat{H}_{ZFS} + \widehat{H}_{EE} \quad (2.8)$$

Each of these terms will be examined separately but briefly they are the Electron Zeeman splitting ($\widehat{H}_{EZ}$), the Nuclear splitting ($\widehat{H}_{NZ}$), the hyperfine interaction ($\widehat{H}_{HFI}$), the nuclear quadrupolar interaction ($\widehat{H}_{NQI}$), the Zero Field Splitting (ZFS) ($\widehat{H}_{ZFS}$), exchange and dipolar interactions ($\widehat{H}_{EE}$).

2.3.1 The Electron Zeeman splitting

This term describes the interaction between the electron spin and the external magnetic field $\mathbf{B_0}$.

$$\widehat{H} = \mu_B \mathbf{B}^T . \mathbf{g} . \hat{\mathrm{S}} \quad (2.9)$$

The superscript T indicates a vector transposition to align the contribution of the magnetic field to the direction of the **g** tensor. In full the equation becomes:

$$\widehat{H}_{EZ} = \mu_B \left[B_x\, B_y\, B_z\right]. \begin{bmatrix} g_{xx} & 0 & 0 \\ 0 & g_{yy} & 0 \\ 0 & 0 & g_{zz} \end{bmatrix} \begin{bmatrix} \hat{S}_x \\ \hat{S}_y \\ \hat{S}_z \end{bmatrix} \tag{2.10}$$

As mentioned in section 2.2, the deviation of the principal *g* values from g_e and the orientation dependence of the electron Zeeman term are due to spin-orbit interaction between the ground and excited states.

The Hamiltonian describing this effect is written as:

$$\widehat{H} = \mu_B \mathbf{B}^T \left(\hat{\mathbf{L}} + g_e \hat{\mathbf{S}}\right) + \boldsymbol{\lambda} \hat{\mathbf{L}}^T \hat{\mathbf{S}} = \mu_B \mathbf{B}^T \left(g_J \hat{\mathbf{J}}\right) + \lambda \hat{\mathbf{L}}^T \hat{\mathbf{S}} \tag{2.11}$$

Where $\boldsymbol{\lambda} \hat{\mathbf{L}}^T \hat{\mathbf{S}}$ is the spin orbit interaction with λ being the spin-orbit coupling constant. Applying second order perturbation theory yields the ***g*** tensor:

$$\boldsymbol{g} = g_e \mathbf{1} + 2\lambda \boldsymbol{\Lambda} \tag{2.12}$$

Where Λ is:

$$\Lambda_{ij} = \sum_{n \neq 0} \frac{\langle \psi_0 | \boldsymbol{L}_i | \psi_n \rangle \langle \psi_n | \boldsymbol{L}_j | \psi_0 \rangle}{\varepsilon_0 - \varepsilon_n} \tag{2.13}$$

Where ψ_o is the wave function of the ground state of the unpaired electron and ψ_n is the wave function of the nth excited states. ε_0 and ε_n are their corresponding energies. The spin – orbit coupling is correlated to the difference between the energy of the ground state and the excited state and is higher in value the closer these energies are to each other. This causes a more significant shift of *g* from g_e [8].

2.3.2 Single crystal vs powder spectra

As discussed previously, **g** (and consequently the Zeeman splitting Spin Hamiltonian) are orientation dependent. This is evidenced by single crystal studies where the sample is rotated in the magnetic field leading to spectra such as those reported in Figure 2.2.

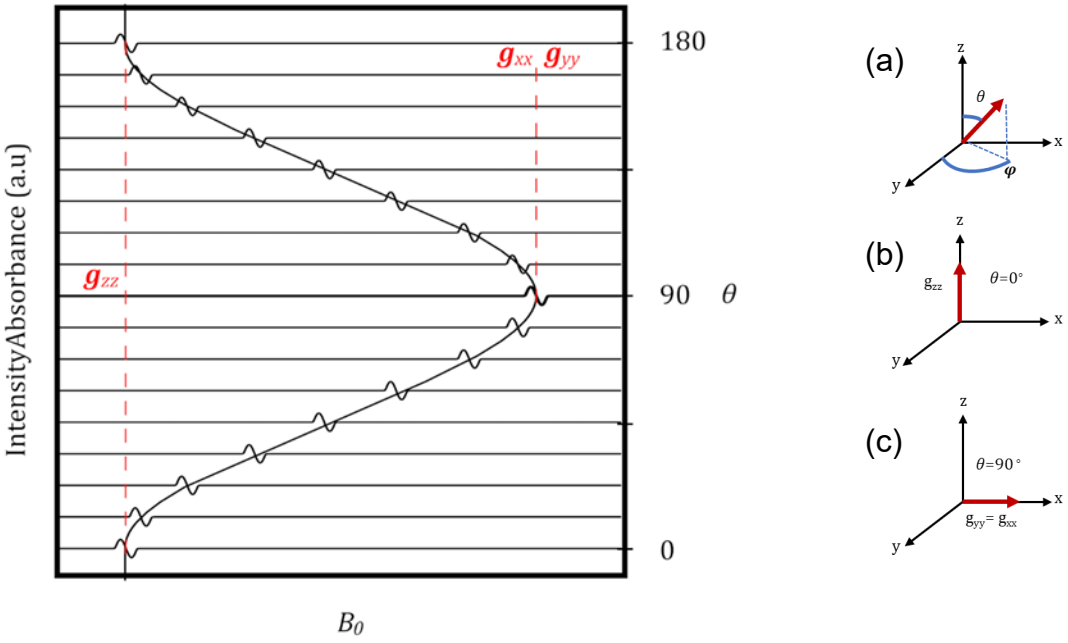

Figure 2.2: On the left-hand side, EPR spectra of a single crystal as a function of θ. These are for an axially symmetric system with P1 symmetry. On the right-hand side, (a) defines the angles θ and φ in relation to the magnetic field vector; (b) shows the projection of *g* onto *B* at θ = 0, 180°, equivalent to g_{zz}; (c) shows the projection of *g* onto *B* at θ = 90°, equivalent to g_{xx} and g_{yy}. Adapted from reference [9].

In most chemical studies and in the case of systems of catalytic relevance such as those studied in this thesis, the sample is in the form of frozen glassy solution or a powder. In these cases, although the spectral lines are typically broader and the angle between the external magnetic field **g** tensor cannot be determined, the principal values of the **g** tensor can still be measured.

The following equation gives the resonance probability, P(*B*), for axial symmetry and a given position of **B**:

$$P(B) = C\,\frac{1}{2}\,sin\theta\,\left(\frac{dB}{d\theta}\right)^{-1} \tag{2.14}$$

Where C is the normalisation constant. In a completely randomly oriented sample, *P*(B) is proportional to $sin\theta$ and B^{-1}, assuming equal probability for all orientations. d*B*/dφ must also be considered for rhombic systems.

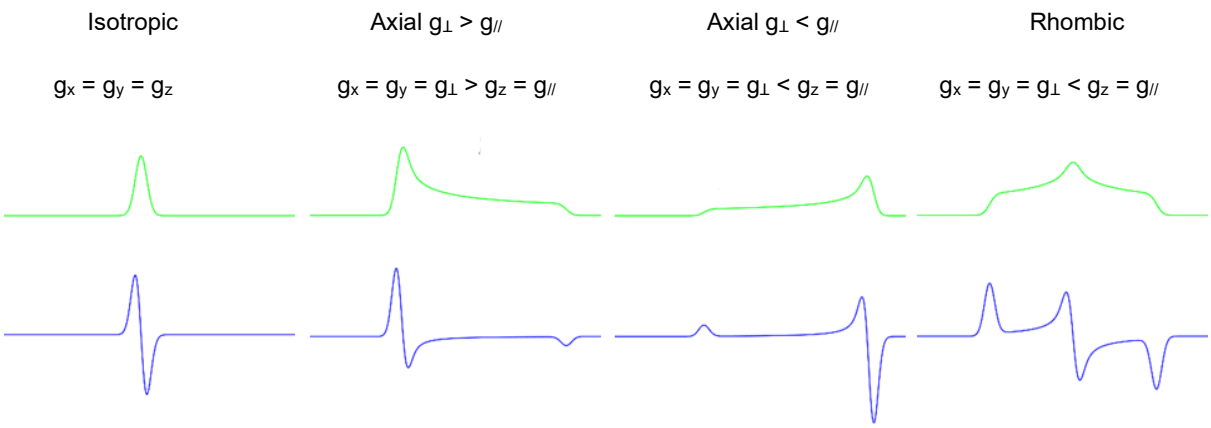

Figure 2.3: Simulated polycrystalline line shapes in relation to the symmetry of the *g* tensor, annotated for each case. Green: absorption spectrum. Blue: first derivative spectrum.

2.3.3 Nuclear Zeeman (NZ) Interaction

When one or more magnetically active nuclei are present, the energy interaction between the nuclear magnetic moment and the external field (Nuclear Zeeman interaction) need to be considered:

$$\widehat{\boldsymbol{H}}_{\boldsymbol{NZ}} = \mu_n \sum_k \boldsymbol{B_0}\, g_{n,k} \widehat{\boldsymbol{I}}_{\boldsymbol{k}} = \mu_n \sum_k B_0\, g_{n,k} \hat{I}_{k,z} \tag{2.15}$$

As each paramagnetic isotope has its own characteristic nuclear *g*-factor g_n, even though the nuclear Zeeman interaction [4] does not influence the CW-EPR spectrum in the first order, it allows distinguishing the different nuclei observed in spectra of hyperfine spectroscopy (e.g. HYSCORE, ENDOR, etc.).

2.3.4 Hyperfine interaction

The hyperfine interaction (hfi) describes the interaction between the electron spin and the nearby nuclear spins. Such interaction can be split into two terms, the isotropic term and the anisotropic term. The first term is also called the Fermi contact interaction and it considers the overlap of the wave function of the electron spin with the nucleus. The Fermi contact term is given by:

$$\boldsymbol{a_{iso}} = \frac{\boldsymbol{8\pi}}{\boldsymbol{3}} \boldsymbol{g_e \mu_B g_n \mu_n} |\boldsymbol{\psi_0(0)}|^{\boldsymbol{2}} \tag{2.16}$$

2.3.5 The nuclear quadrupole Interaction

For nuclei with nuclear Spin *I* > 1/2, the charge distributions are not spherical due to their structures (Fig. 2.4). This results in an electric quadrupole moment that interacts with the electric field gradient.

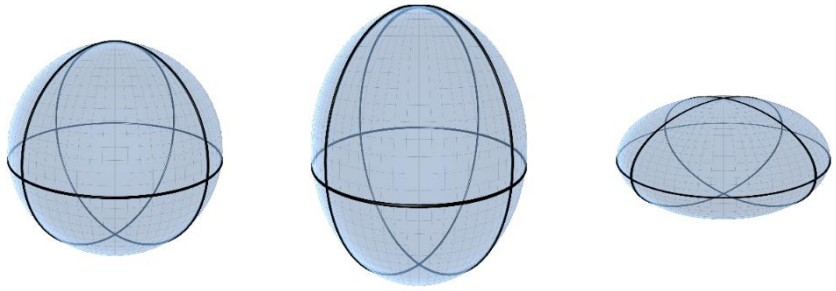

$Spherical$ $Elongated$ $Flattened$

$Q = 0; I = 0, 1/2$ $Q > 0; I > 0, 1/2$ $Q < 0; I < 0, 1/2$

Figure 2.4: Illustration of the relation between nuclear charge distribution shape and the nuclear quadrupole moment Q for some I >1/2 isotopes often investigated in EPR. Adapted from reference [4].

This is called the nuclear quadrupole moment Q. Even though the interaction is purely electrostatic, the orientation of nuclear quadrupole moment is linked to that of the nuclear spin. It can be considered as a self-interaction of the nuclear spin and the Hamiltonian is written as:

$$\mathcal{H}_{NQ} = P_x I_x^2 + P_y I_y^2 + P_z I_z^2 = \frac{e^2 qQ}{4I(2I-1)\hbar}\left[3I_z^2 - I(I+1) + \eta\left(I_x^2 - I_y^2\right)\right] \quad (2.19)$$

The nuclear quadrupole tensor ***P*** can then be written as:

$$\boldsymbol{P} = \frac{e^2 qQ}{4I(2I-1)\hbar}\begin{bmatrix} -(1-\eta) & & \\ & -(1+\eta) & \\ & & 2 \end{bmatrix} \quad (2.20)$$

where *eq* is the magnitude of the electric field gradient experienced by the nucleus and Q is the quadrupole moment of the nucleus. The asymmetry parameter $\eta = (P_x - P_y)/P_z$, with $|P_z| > |P_y| > |P_x|$, represents the deviation of the field gradient from axial symmetry and can adopt values in the range $0 < \eta < 1$.

The isotropic hyperfine coupling arises from the presence of finite electron spin density at the nucleus, and is proportional to the probability of finding the electron spin at the nucleus $|\boldsymbol{\psi_0}(\mathbf{0})|^2$.

The anisotropic term is of classical nature and depends on the magnetic dipole-dipole interactions between the unpaired electron and the nucleus (at distance *r*).

$$\mathcal{H}_{DD} = \frac{\mu_0}{4\pi\hbar} g_e g_n \mu_n B_n \left[\frac{(3\boldsymbol{Sr})(\boldsymbol{rI})}{r^5} - \frac{\boldsymbol{SI}}{r^3}\right] = \boldsymbol{STI} \tag{2.17}$$

The experimental **A** tensor can therefore be decomposed in the two relevant terms as follows:

$$\boldsymbol{A} = \begin{bmatrix} A_{xx} & A_{xy} & A_{xz} \\ A_{yx} & A_{yy} & A_{yz} \\ A_{zx} & A_{zy} & A_{zz} \end{bmatrix} = a_{iso}\boldsymbol{U} + \boldsymbol{T} \tag{2.18}$$

2.3.6 Zero Field Interaction

For spin systems with more than one unpaired electron (S > 1/2), one also needs to consider the interactions between the electron spins. These interactions can lead to the degeneracy of the spin states being partially removed, even without the applied external magnetic field. It is therefore called the zero-field interaction (***zfi***). The Hamiltonian is written as:

$$\widehat{\mathcal{H}}_{ZFS} = \widehat{\boldsymbol{S}}_{\mathbf{1}} \cdot \boldsymbol{D} \cdot \widehat{\boldsymbol{S}}_{\mathbf{2}} \tag{2.21}$$

where ***D*** is the symmetrical and traceless zero-field interaction tensor. The presence of ***zfi*** can significantly increase the complexity of the system. It is not uncommon for the position of energy levels at the start (with no magnetic field) to be in a different order than when a magnetic field is applied, similarly the extent by which energy levels are shifted may not be the same for all energy levels. As none of the systems observed in this thesis are affect by ***zfi*** there is no need to dig too deeply into this but some information relevant to high spin Cr(III) is present in section 2.6 [10].

2.4 Continuous Wave (CW) Spectroscopy

Continuous Wave EPR spectroscopy is largely regarded as the simplest application of EPR spectroscopy. As the name implies the sample is irradiated with a continuous stream of microwave radiation at constant frequency while the magnetic field is swept through the desired values. The operating microwave frequency depends on the intensity of the externally applied magnetic field, but traditionally only certain frequency ranges are used. X-band is typically around 9.5 GHz, Q-band is 35 GHz and W-band is 95 GHz. When the changes in magnetic field match an EPR transition with its microwave frequency, energy from the microwave radiation is absorbed by the sample while the rest is returned to the detector which can subtract the return signal with the original intensity giving us the absorbed power. However, the signal will weaken and disappear if the EPR transition becomes saturated. A way to overcome this is to use lower powers of microwave radiation but it will also decrease signal intensity. Temperature also plays a role as higher temperatures typically result in faster relaxation times.

The simplicity of the continuous wave setup makes the machines much easier to operate and are effective in many applications and one of its most important aspects is that it is possible to run EPR at room temperature.

2.5 Pulse EPR

Pulse EPR is a series of spectroscopical techniques that utilize sequences of short, but powerful, bursts of microwave radiation. While continuous wave EPR spectroscopy predates NMR spectroscopy, pulse techniques were first pioneered in NMR and brought into EPR spectroscopy shortly after. The setup for a pulse spectrometer is much more complex than what is used by the simpler continuous wave devices, but these machines can probe much smaller hyperfine couplings, nuclear quadrupole interactions or distant electron couplings.

In the frame of a semiclassical description [11, 12, 13, 14], the electron spins in the sample will orient either in parallel or antiparallel configuration, relatively to the external magnetic field. The net magnetization can be treated like a classical vector with a defined length and direction in space:

$$\boldsymbol{M} = \frac{1}{V}\sum_{i} \boldsymbol{\mu_i} \tag{2.22}$$

where *V* is the sample volume with all individual magnetic moments. A useful method to simplify the understanding of the motion of magnetization, during a microwave pulse, is to use the rotating and laboratory (or, in short, lab) frames.

By convention, the external magnetic field (***B₀***) is set as orientated along the Z axis while the magnetic field from microwave irradiation (***B₁***) is set along the X axis. In the absence of the magnetic field the electron spin has a random orientation. When the external magnetic field is activated, it applies a torque to the magnetic moment **M** of the electron spin, causing it to precess on a cone about ***B₀***. This causes a time-averaged magnetization vector ***M₀*** along the Z' axis. The precessing frequency is equal to the Larmor frequency:

$$\omega_L = -\gamma \boldsymbol{B_0} \tag{2.23}$$

where γ is the gyromagnetic ratio and ***B₀*** is the external magnetic field. The magnetic field of microwave radiation ***B₁*** oscillates with the frequency of the radiation itself and introduces a perturbation on the precession of the system. When applying a microwave pulse along the X axis, which is, in essence, a time-dependent magnetic field ***B₁*** oscillating with the microwave frequency, it becomes very complicated to consider its effects on the magnetization vector in the lab-frame. Both the ***B₁*** field and the spins undergo complex rotations when viewed in this frame. It is mathematically permitted to change this static reference frame to one in rotation along its Z axis, spinning at the Larmor frequency. This allows us to simplify the mathematical description and only visualize the effect of the ***B₁*** field. The magnetic moment in this new system is defined as ***M₀***.

Variations of the magnetization as a function of time are described by the Bloch equations [15].

$$\frac{\partial \boldsymbol{M}}{\partial t} = \frac{-g\mu_B}{\hbar}\, \boldsymbol{M} \times \boldsymbol{B_0} \tag{2.24}$$

In the rotating frame, the precession frequency of ***M*** about the Z-axis is calculated with:

$$\Omega = \omega_L - \omega_{mw} \tag{2.25}$$

After applying a microwave pulse, the microwave magnetic field $\boldsymbol{B_1}$, that is perpendicular to the external magnetic field, causes an additional precession of $\boldsymbol{M_0}$ about the X^{rot}-axis with angular velocity:

$$\omega_1 = -\gamma \boldsymbol{B_1} \tag{2.26}$$

where ω_1 is called the Rabi frequency. By turning on and off the microwave on the resonator at the right moment, it is possible to control how far the magnetization will be turned. For a microwave pulse of duration t_p, the angle by which the magnetization vector will rotate, called the flip angle, is given by:

$$\alpha = \gamma B_1 t_p \tag{2.27}$$

The flip angle is one of the most important parameters in setting a pulse sequence.

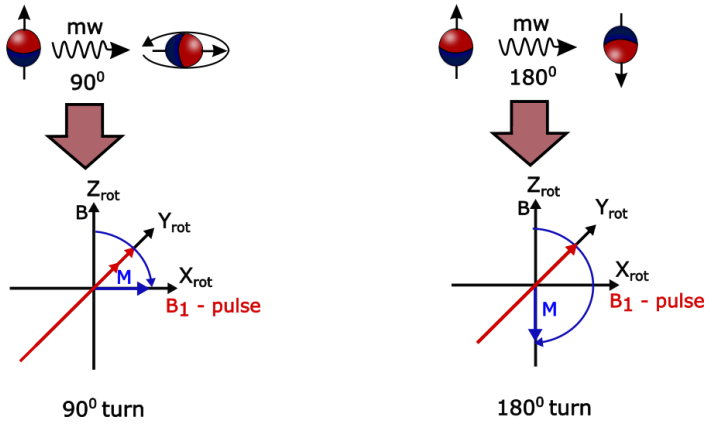

Figure 2.5: Illustration of the flip angles that can be obtained by adjusting the pulse length t_p or the microwave magnetic field strength B_1. Figures taken and combined from reference [16] and [17].

2.5.1 Hahn Echo

Pulse EPR requires careful manipulation of the $\boldsymbol{M_0}$ moment to provide any useful information. This requires setting up what is referred to as spin-echo sequence. The key aspects of a spin-echo sequence are the changes of $\boldsymbol{M_0}$ and the relaxation properties of the Spin system being probed. The simplest pulse sequence that can be applied to a system consists of a single $\pi/2$ microwave pulse that flips the magnetization $\boldsymbol{M_0}$ in the XY – plane, described hereafter in the rotating frame without the use of the superscript rot for simplicity (Figure 2. 6a) and is called Free Induction Decay (FID). FID tells us how quickly the system relaxes after being affected by $\boldsymbol{M_1}$. After Fourier transformation, a signal occurs at the resonant frequency of the spin packet.

The Hahn echo was described for the first time by E. Hahn [18]. In this experimental setup, the first $\pi/2$ pulse converts the magnetization $\boldsymbol{M_0}$ from Z-axis to Y-axis. It is followed by a period of free evolution τ during which the spin packets fan out along the XY-plane. By applying a second π – pulse the magnetization is flipped (still on the XY-plane) and the spin packets refocus after another τ interval. This refocussing generates a Hahn echo called spin echo. These are very useful, not only to probe the relaxation properties but also for the technical reason that they are detected when the microwave radiation is off, limiting unwanted interference.

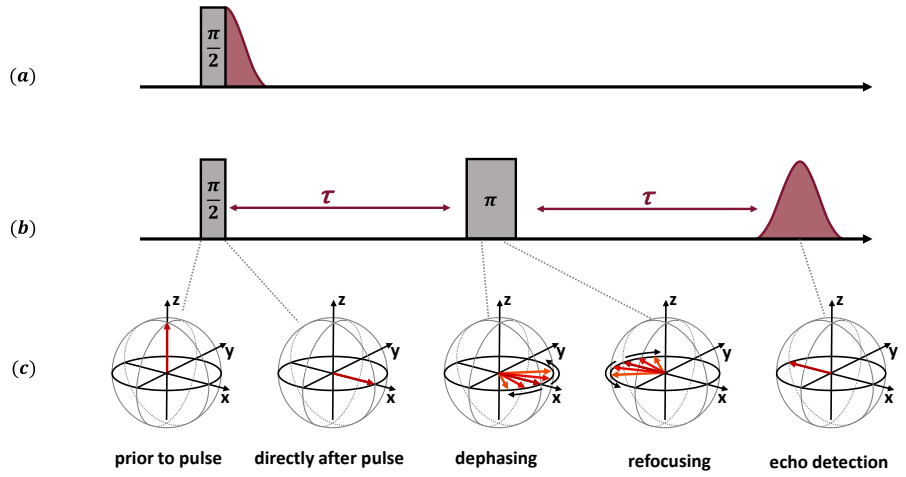

Figure 2.6: (a) Generation of the FID signal by a $\pi/2$. (b) The two-pulse sequence giving rise to the Hahn spin echo, which is an inverted FID followed by an FID. (c) The evolution of the magnetic moments of individual spin packets (red arrows) as seen in the rotating frame, from the Hahn Echo sequence. Taken from [19].

2.5.2 ESEEM pulse sequences

The Electron Spin Echo Envelope Modulation or ESEEM is a time-domain experiment used to determine the nuclear frequencies of weakly coupled nuclei to the unpaired electron. The ESEEM pulse sequence creates a spin echo that decays as a function of time. By running the Fourier transformation of the decaying time domain trace, we can convert the signal to its frequency domain. The spectrum post FT allows the identification of the nuclear frequencies (NMR frequencies) of the nuclei interacting with the unpaired electron [20, 21].

The practical execution of ESEEM experiments varies and the cases relevant to this thesis will be presented individually but generally speaking, every ESEEM experiment can be subdivided in the three parts as shown in Figure 2.7. These include preparation period followed by the first evolution time, the mixing period followed by a second evolution time and the detection period [22].

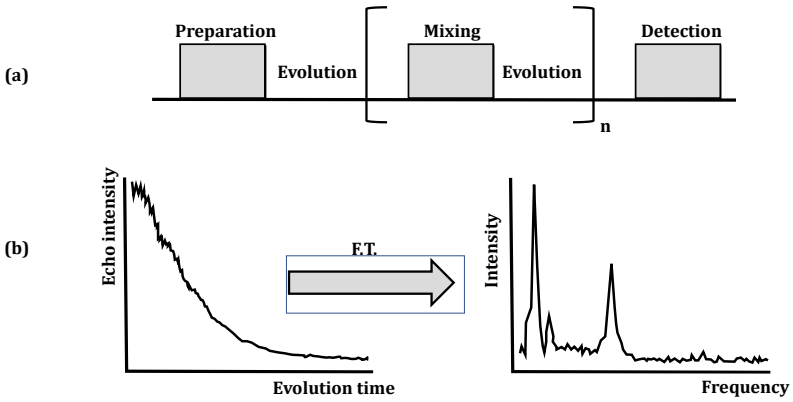

Figure 2.7: General outline of an ESEEM experiment. (A) A schematic representation of the preparation, mixing, and detection building blocks. (B) A standard two-pulse ESEEM time-domain spectra and its corresponding frequency – domain spectra obtained after Fourier transformation. Taken and adapted from reference [22].

2.5.2.1 Two-pulse ESEEM

The two pulse ESEEM is based on the previously discussed Hahn echo sequence [20, 23] composed of $\pi/2 - \tau - \pi - echo$. The first pulse of $\pi/2$ creates electron coherence that is allowed to evolve for the time τ. The mixing period consists of a π pulse that mixes the electron coherences. After a second evolution time τ an electron spin echo is generated.

Figure 2.8: Two-pulse ESEEM sequence [22].

The spin echo intensity decays as a function of τ, depending also on the phase-memory time T_m of the electron spin. This decay is modulated with nuclear frequencies of magnetic nuclei coupled to the unpaired electron. Assuming ideal, perfectly rectangular profile, pulses the resulting echo modulation for a S = 1/2, I = 1/2 system is given by:

$$V_{2P}(\tau) = 1 - \frac{k}{4}\left[2 - 2\cos(\omega_\alpha \tau) - 2\cos(\omega_\beta \tau) + \cos(\omega_- \tau) + \cos(\omega_+ \tau)\right] \quad (2.28)$$

where the modulation depth is defined as:

$$k = \left(\frac{B\omega_I}{\omega_\alpha \omega_\beta}\right)^2 \tag{2.29}$$

The nuclear frequencies ω_α and ω_β are defined as:

$$\omega_\alpha = |\omega_{12}| = \left[\left(\omega_I + \frac{A}{2}\right)^2 + \frac{B^2}{4}\right]^{1/2} \tag{2.30}$$

$$\omega_\beta = |\omega_{34}| = \left[\left(\omega_I - \frac{A}{2}\right)^2 + \frac{B^2}{4}\right]^{1/2} \tag{2.31}$$

and $\omega_\pm = \omega_{12} \pm \omega_{34}$ are the combination frequencies. Two-pulse ESEEM is a relatively simple technique with a short time needed to record it. ESEEM spectra allow quick identification of magnetic nuclei in the vicinity of the unpaired electron. However, the experiment also detects the sum and difference of the same frequencies that are being probed. In the event of multiple magnetic nuclei around the electron this combination can make the spectrum overburdened with broadened and overlapping signals that cannot be resolved and individually assigned. The other major problem with two-pulse ESEEM can emerge when the system has a short T_m and it overlaps with the spectrometer deadtime. The energy output of the microwave pulses is significantly stronger than what is used in continuous wave spectroscopy, if the full output of a microwave pulse were to enter the detector it would irreversibly damage it. To avoid this, a series of mechanisms exist to prevent any microwave radiation from reaching the detector while pulses are being applied. The time required to restore functionality to the detector after a pulse is called spectrometer deadtime and if the T_m time is shorter than the deadtime much of the signal will be impossible to record.

2.5.2.2 Three pulse ESEEM

Some of the issues encountered with two-pulse ESEEM are either addressed or avoided with three-pulse ESEEM [21, 24, 22] experiments with sequence $\pi/2 - \tau - \pi/2 - T - \pi/2 - echo$. The first two $\pi/2$ pulses $(\pi/2 - \tau - \pi/2)$ in the preparation

period will create nuclear coherences that will evolve during time *T* (evolution period) and converted to a detectable electron coherence from the last $\pi/2$ pulse.

Figure 2.9: Three-pulse ESEEM sequence [22].

For a *S* = 1/2, *I* = 1/2 system the echo modulation from the three-pulse ESEEM experiment is given by:

$$V_{3P}(\tau,T) = 1 - \frac{k}{4}\Big\{\big[1-\cos(\omega_\beta\tau)\big]\big[1-\cos(\omega_\alpha(T+\tau))\big] + \big[1-\cos(\omega_\alpha\tau)\big]\Big[1-\cos\Big(\omega_\beta(T+\tau)\Big)\Big]\Big\} \tag{2.32}$$

T is varied between experiments and the echo intensity decays as a function of it. The decay depends now in the phase memory time of the nuclear spins T_m^n which is usually significantly longer than the phase memory time T_m of the electron spins. As an extra bonus the combination frequencies $\omega_\pm$ are no longer observed, leading to a reduced number of frequency lines compared to the two-pulse ESEEM experiment which provides narrower and more easily resolved lines.

The influence of τ leading on three-pulse ESEEM can lead to τ-dependent blind spots, which is why it is recommended to always run three pulse ESEEM multiple times with different influence of τ values. Phase cycling is also required to remove spurious signals [22, 25].

2.5.2.3 HYSCORE

Hyperfine Sublevel Correlation Spectroscopy or HYSCORE is a two-dimensional, four-pulse variation on ESEEM, with sequence $\pi/2 - \tau - \pi/2 - t_1 - \pi - t_2 - \pi/2 - echo$. An additional π – pulse is introduced between the second and third $\pi/2$ pulse of the three-pulse ESEEM sequence, improving the interpretation of ESEEM spectra [26].

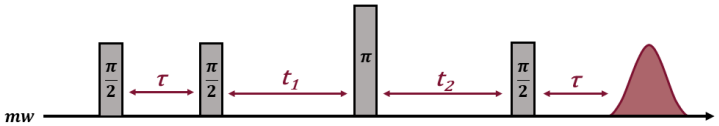

Figure 2.10: Four-Pulse HYSCORE sequence [20].

The experiment varies t_1 and t_2 which are plotted independently in a 2D space. HYSCORE experiments make the overlapping features in the two- and three-pulse ESEEM observable and much better resolved.

The preparation period in HYSCORE experiments consists of $\pi/2 - \tau - \pi/2$, which generate nuclear coherences and polarizations. After a first free evolution time (t_1) the nuclear coherences are transferred from one m_s manifold to the other by a strong mixing π pulse. Then there is another free evolution time (t_2) before the last $\pi/2$ pulse which generates the echo. 2D Fourier transformation of the time-domain data along the two dimensions generates a 2D frequency-domain spectra where cross peaks relate to corresponding nuclear frequencies. A HYSCORE spectrum in 2D frequency-domain is divided in quadrants but usually only the (+, +) and (−, +) are displayed.

The (+, +) quadrant displays signals from weakly coupled nuclei ($|A| < 2\omega_I|$), whereas (−, +) displays signals from strongly coupled nuclei ($|A| > 2\omega_I|$). Figure 2.11a and Figure 2.11b show the energy level schemes for an S = 1/2, I = 1/2 system in the weak and strong coupling, respectively. In exact cancelation conditions, both quadrants will display intense cross peaks due to a large k value.

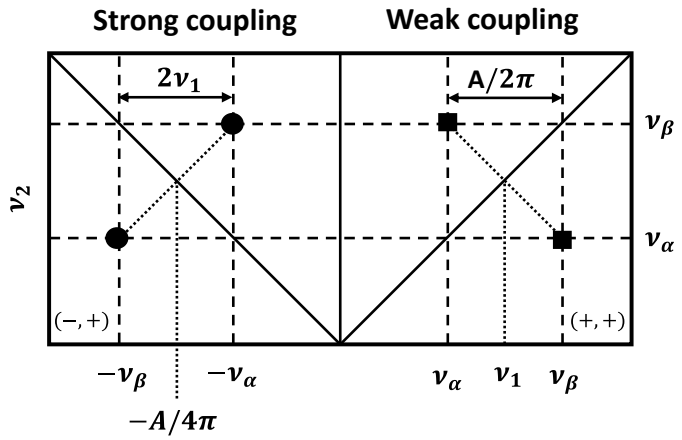

Figure 2.11: Schematic representation of the appearance of the cross peaks in different quadrants in the HYSCORE spectra in case of weak hyperfine coupling (■) and strong hyperfine coupling (•) for a *S* = 1/2, *I* = 1/2 spin system. Adapted from reference [4].

The case presented above is, alas, only applicable to perfect crystals. Polycrystalline powders and frozen solutions appear as broad ridges representing the sum of individual orientations. The HYSCORE spectra for a powder sample of an *S* = 1/2, *I* = 1/2 spin system is represented in Figure 2.11. For randomly oriented systems the HYSCORE spectra need to be recorded at different field positions.

In the single crystal systems, the cross-peak intensity is distributed between the left and right quadrant. However, for frozen solutions and powders not all cross peaks will have the same intensity when viewed in different quadrants. This is due to orientation selection and amplitude effects caused by destructive interferences [27]. This limits the information that can be used mostly to peak positions.

The anisotropy of the hyperfine coupling interaction *T*, can be determined from the shift of the curvature ridges from the anti-diagonal given by:

$$\Delta\omega_{max} = \frac{9T^2}{32|\omega_I|} \tag{2.33}$$

Where *T* is the dipolar component of the hyperfine tensor.

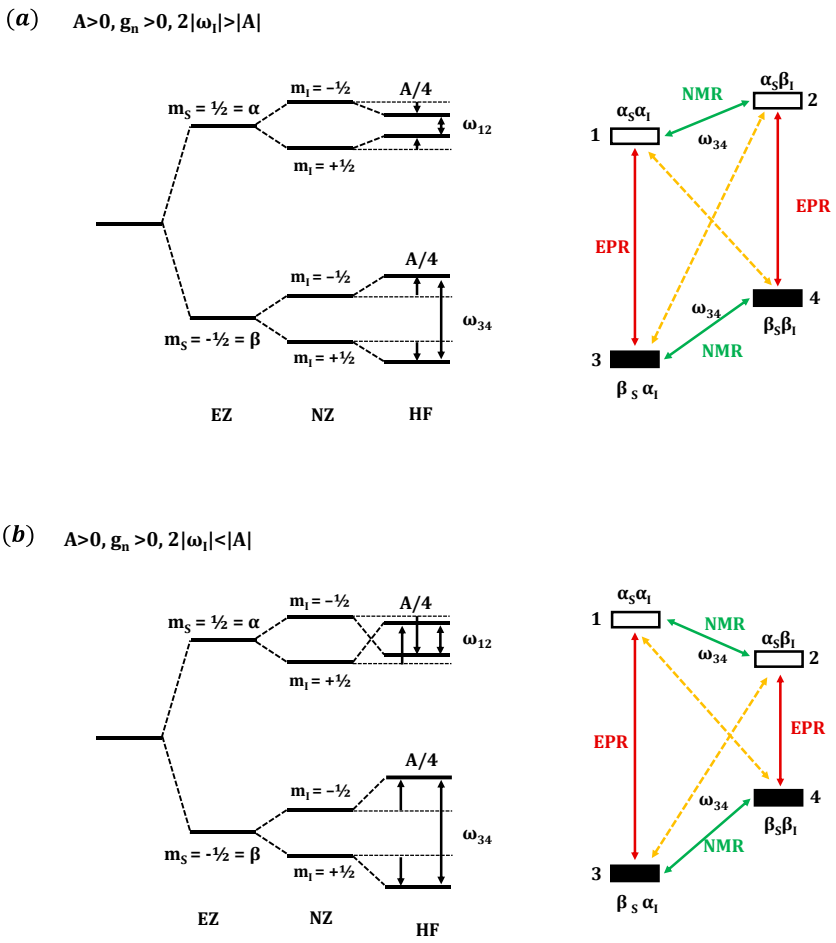

Figure 2.12: Energy-level diagrams for an $S = 1/2$, $I = 1/2$ spin system; (a) Weak coupling case, $2|\omega_I| > |A|$, with $A > 0$, $g_n > 0$; (b) Strong coupling case $2|\omega_I| < |A|$. The red lines correspond to EPR allowed transitions, the dotted yellow lines to forbidden transitions and the green lines to NMR transitions. Adapted from reference [4].

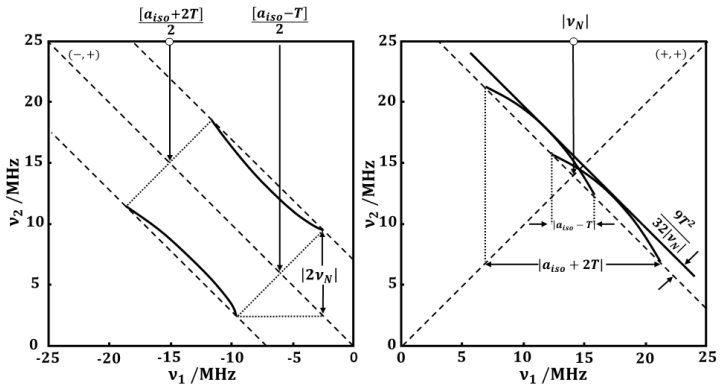

Figure 2.13: Schematic representation of HYSCORE spectra of a powder sample for an $S = 1/2$, $I = 1/2$ spin system with an axial hyperfine tensor. (a) Strong-coupling case with $\boldsymbol{\nu_I}$ = 3.5 MHz, $\boldsymbol{a_{iso}}$ = 18 MHz, and T = 6 MHz. (b) Weak-coupling case with $\boldsymbol{\nu_I}$ = 14 MHz, $\boldsymbol{a_{iso}}$ = 2.5 MHz, and T = 6 MHz. Adapted from reference [4].

When spin systems with I $\boldsymbol{I} \geq 1$ become involved the nuclear quadruple interaction is also present in HYSCORE spectra. This perturbation can make prohibited transition appear in the spectra and we can detect single-quantum (SQ: $|\Delta \boldsymbol{m_I}| = 1$) and double quantum (DQ: $|\Delta \boldsymbol{m_I}| = 2$) transitions. The double-quantum transitions are observed in frequencies given by:

$$\omega_{\alpha,\beta}^{DQ} = 2\sqrt{\left(\omega_I \pm \frac{A}{2}\right)^2 + \left(\frac{e^2qQ}{4h}\right)^2 (3+\eta^2)} \qquad (2.34)$$

where A is the hyperfine coupling at the observer position. The DQ cross peaks are less broad and more intense compared to the SQ ridges in the HYSCORE spectra. This is because the nuclear quadrupole interaction is contributing in first order in the SQ frequencies, while for DQ frequencies this interaction is contributing in second order.

HYSCORE, for all its uses has its own set of drawbacks. Like three-pulse ESEEM it requires phase cycling, leading to higher acquisition times. It also needs to be executed on multiple field positions and different $\boldsymbol{\tau}$ values in addition to being a 2D technique. All of this can compound in really long acquisition times, which require constant liquid helium cooling. There is also the issue where the presence of many paramagnetic nuclei will result in spectra of challenging interpretation.

2.5.3 Pulsed ENDOR

Electron Nuclear DOuble Resonance (ENDOR) exists both in pulse and continuous wave form but in this project, it was employed in its pulse variation. In an ENDOR experiment short pulses of microwaves (mw) in the order of ns and radiofrequencies (rf) in the order of μs are used [28]. The rf pulse transfers spin polarization between electron and nuclear transitions. In this way, nuclear polarization is transferred to electron coherence and detected via an echo. The amplitude of this echo is a function of the rf used, with a fixed time interval detection period.

ENDOR comes with its own requirements, which are that the phase memory time T_m needs to be longer than the spectrometer deadtime and time T_1 (spin-lattice relaxation)

be sufficiently long. The most used variations of ENDOR are: Davies-ENDOR [29] and Mims-ENDOR [23].

2.5.3.1 Davies ENDOR

The Davies ENDOR sequence $\boldsymbol{\pi_{mw} - \pi_{rf} - \pi/2_{mw} - \tau - \pi_{mw} - \tau - echo}$ is designed to apply a selective microwave pulse $\boldsymbol{\pi}$ that inverts the polarizations of a targeted EPR transition [29]. In the mixing period a rf pulse is applied to invert one of the NMR transitions. Then radio frequency is swept and upon entering resonance with the nuclear transition it will affect the electron polarization which can then be detected with a standard Hahn echo sequence.

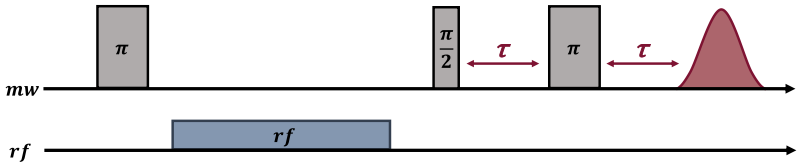

Figure 2.14: Pulse sequence of Davies ENDOR experiment.

2.5.3.2 Mims ENDOR

The Mims ENDOR sequence $\boldsymbol{\pi/2_{mw} - \tau - \pi/2_{mw} - \pi_{rf} - \pi/2_{mw} - \tau - echo}$, is based on the stimulated echo sequence, with three non-selective $\boldsymbol{\pi/2}$ microwave pulses, where the first two pulses create nuclear coherences and polarisation [23]. The nuclear polarizations are changed during the mixing period by a selective rf pulse, whose frequency is swept during the experiment. The final $\boldsymbol{\pi/2}$ microwave pulse generates the simulated echo.

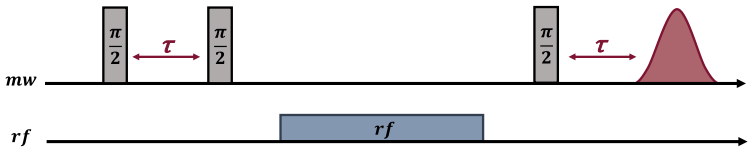

Figure 2.15: Pulse sequence of Mims ENDOR experiment.

2.6 EPR Properties of Chromium and Its Oxidation States

In Chapter 1 we explained at length how chromium is a transition metal with numerous oxidation states and the role this plays with it chemistry. We will now examine the EPR

properties of chromium in greater detail. Natural abundance chromium occurs as 4 isotopes with ^{50}Cr = 4.34%, ^{52}Cr = 83.8%, ^{54}Cr = 2.37% have *I* = 0, with only ^{53}Cr = 9.5% having *I* = 3/2 being magnetically active. This results in 4 satellite peaks for every spectral line with the following intensities:

$$\frac{^{53}Cr}{^{52}Cr} \times \frac{1}{spectral\ lines} = \frac{9.5}{90.5} \times \frac{1}{4} = \frac{1}{38} \qquad (2.35)$$

In many practical applications these additional satellite signals cannot be resolved individually or from the background noise and can often be ignored (in Chapters 4 and 5 these signals are present in many of the room temperature spectra). The valence shell electron configuration of chromium atoms in vacuum is $3d^5\ 4s^1$.

Chromium 0 compounds have an octahedral structure, and the six electrons occupy all of the slots in the t_{2g} level rendering the whole spin system diamagnetic with formally a $3d^6$, electron configuration.

Chromium (I) compounds have a $3d^5$ electron configuration with a single unpaired electron. In the presence of a ligand field the symmetry is lowered to give a singly occupied molecular orbital, either due to the ligand field itself or due Jahn-Teller distortion. When the Jhan-Teller effect is small and the complex has symmetry elements, the abundance of thermically accessible excited states creates many relaxation pathways for spin-spin diffusion, resulting in fast relaxation times and severe line broadening (in our case this is particularly notable with $[Cr(CO)_4dppp]^+$, see Chapter 4). In these cases, it is convenient to operate at lowered temperature and frozen solution.

$[Cr(CO)_6]^+$ has proven an elusive species to study [30]. A report from Bagchi *et al.* from 1986 made a tentative claim while studying the electrochemical oxidation of [Dibenzo-18-crown-6-K][$Cr(CO)_5F$] and $Cr(CO)_6$. Follow up studies have been largely unable to confirm the numbers attributed to this species. Still, as the simplest Cr(I) species that can be modelled it spectrum is displayed below.

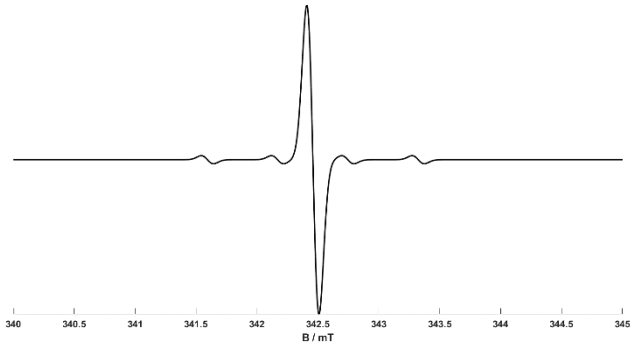

Figure 2.16: Simulation of $[Cr(CO)_6]^+$ from parameters published in [30]. g_{iso} = 1.982; ^{53}Cr a_{iso} = 20 MHz.

Besides the complexes bearing a phosphine ligand such as the ones studied in Chapter 4 of this thesis, other examples of Cr(I) complexes studied with EPR are nitrosyl-phosphine complexes [31, 32] and piano stool complexes, an example of which is also seen in Chapter 4 [33, 30].

Chromium II is a s^0d^4 system and can exist both as a low-spin (S=1) and high-spin system (S=2). This oxidation state is challenging to record and there are not a lot of studies conducted on it using EPR spectroscopy. Even when it is employed it is often paired with other spectroscopic techniques such as X-ray, UV-Vis and IR spectroscopies. It is reported by Scarborough *et al.* that some reported instances of low-spin Cr(II) might in fact be high spin Cr(III) (S = 3/2) where one of the unpaired electrons is located on a ligand and is anti-ferromagnetically coupled [34].

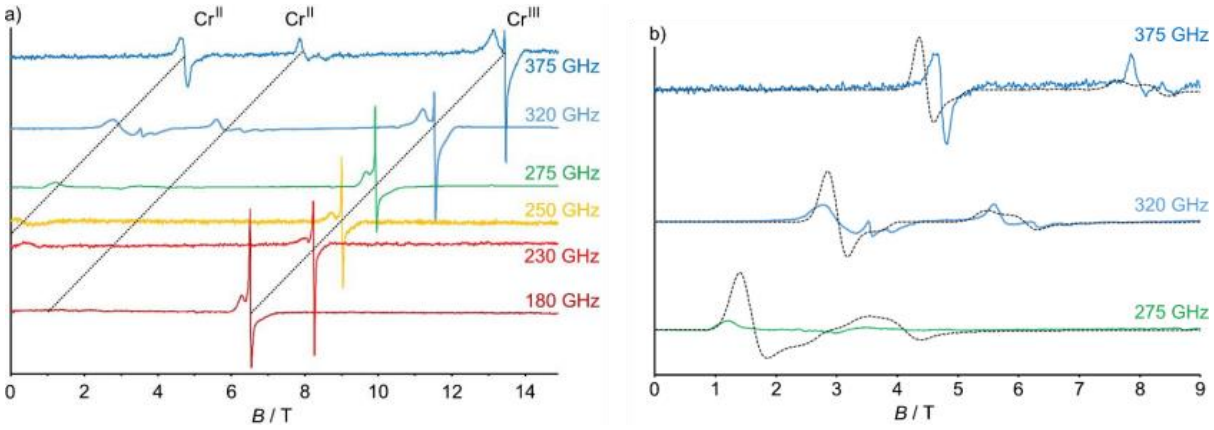

Figure 2.17: a) HFEPR spectra of a pressed powder pellet of $[Cr(ddpd)_2][BF_4]_2$ (ddpd = N,N'-dimethyl-N,N'-dipyridine-2-yl-pyridine-2,6-diamine) at 5 K and different frequencies. The signal at higher fields corresponds to a $[Cr(ddpd)_2]^{3+}$ impurity. b) Simulations of the high frequency spectra of the Cr(II) region (dotted black) based on the spin Hamiltonian and parameters: S = 1; g_x,= 2.08, g_y = 2.10, g_z = 2.15; D = 230838 MHz; E = 5996 MHz. Adapted from figure 5S of [35] electronic supporting information.

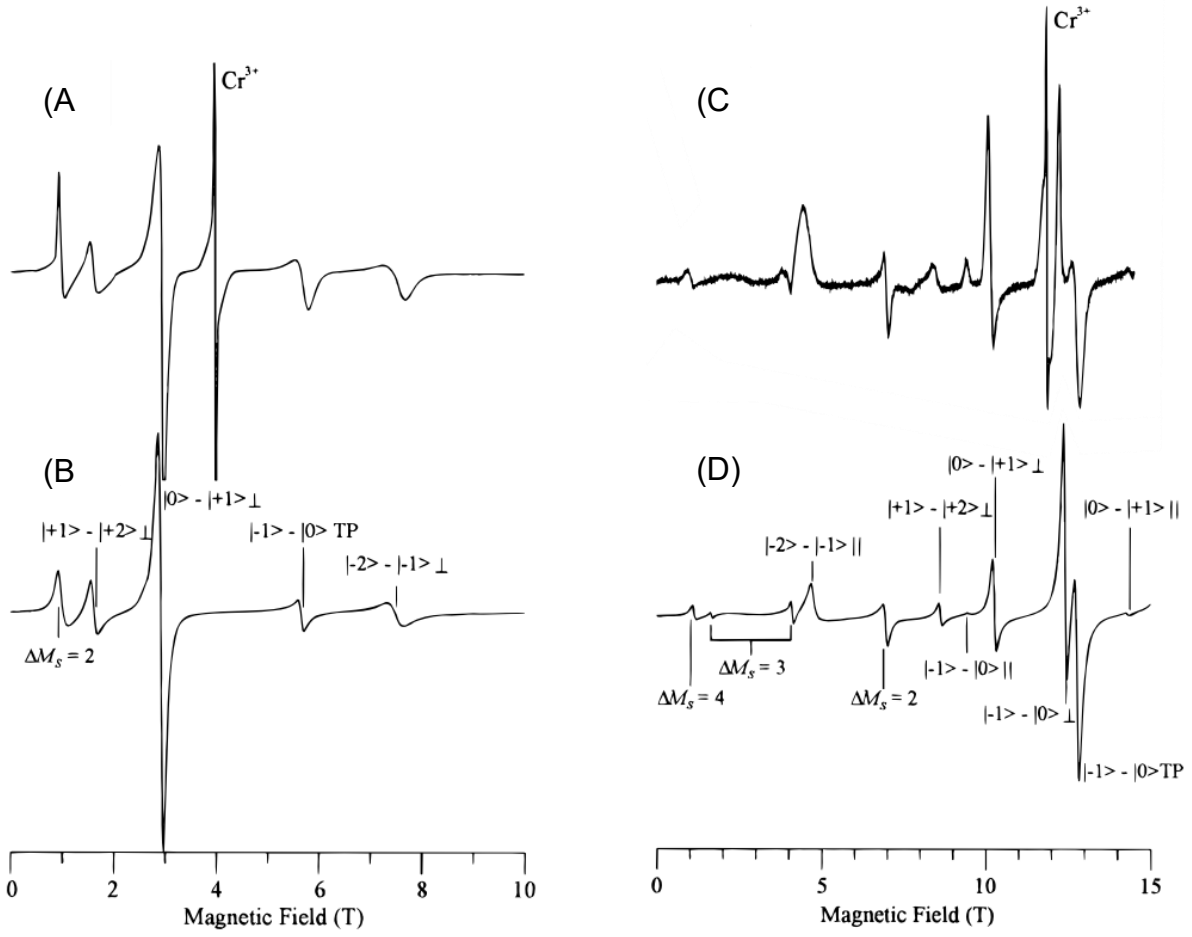

Figure 2.18: EPR spectra (A) and (C) and simulations (B) and (D) of aqueous high spin Cr^{2+} (~0.1-0.2 M) with a sulphate counterion. MW frequency = 109.564 GHz (A) and 328.69 GHz (C). Recorded at T = 10 K; field modulation frequency = 8.7 KHz; modulation amplitude = 1.5 mT. An aqueous Cr^{3+} impurity at g = 2.00 is indicated. Simulation parameters ((B) and (D)): S = 2; $g_\perp = g_{//}$ = 1.98; D = -65954 MHz, E = 0. Adapted by combining Figures 1 and 2 of [35].

The most studied chromium oxidation state is Cr(III) (s^0d^3) as it has the most favourable combination of chemical stability and EPR properties. In $3d^3$ ions the primary contribution is spin-orbit coupling which is slower than the mechanism present in Cr(I) systems [36]. Its more common spin state is that of S = 3/2 due to three unpaired electrons. It is also possible to find Cr(III) low spin though it is far less common with S = 1/2, which makes it quite similar to Cr(I). A defining feature of spin systems with multiple electrons is the Zero Field Splitting (Section 2.3.6) which plays a big role in high spin Cr(III) EPR and the spectra must be considered in terms of the two Kramer's doublets |3/2, ± 1/2> and |3/2 ± 3/2>, separated by |2D| [37]. The E term of the ZFS comes into play instead when the complex is rhombic which has the effect of intermixing the |3/2 ± 1/2> and |3/2 ± 3/2> states. ZFS, by its nature, contributes differently at different magnetic field positions and thus the wavelength of the microwave used.

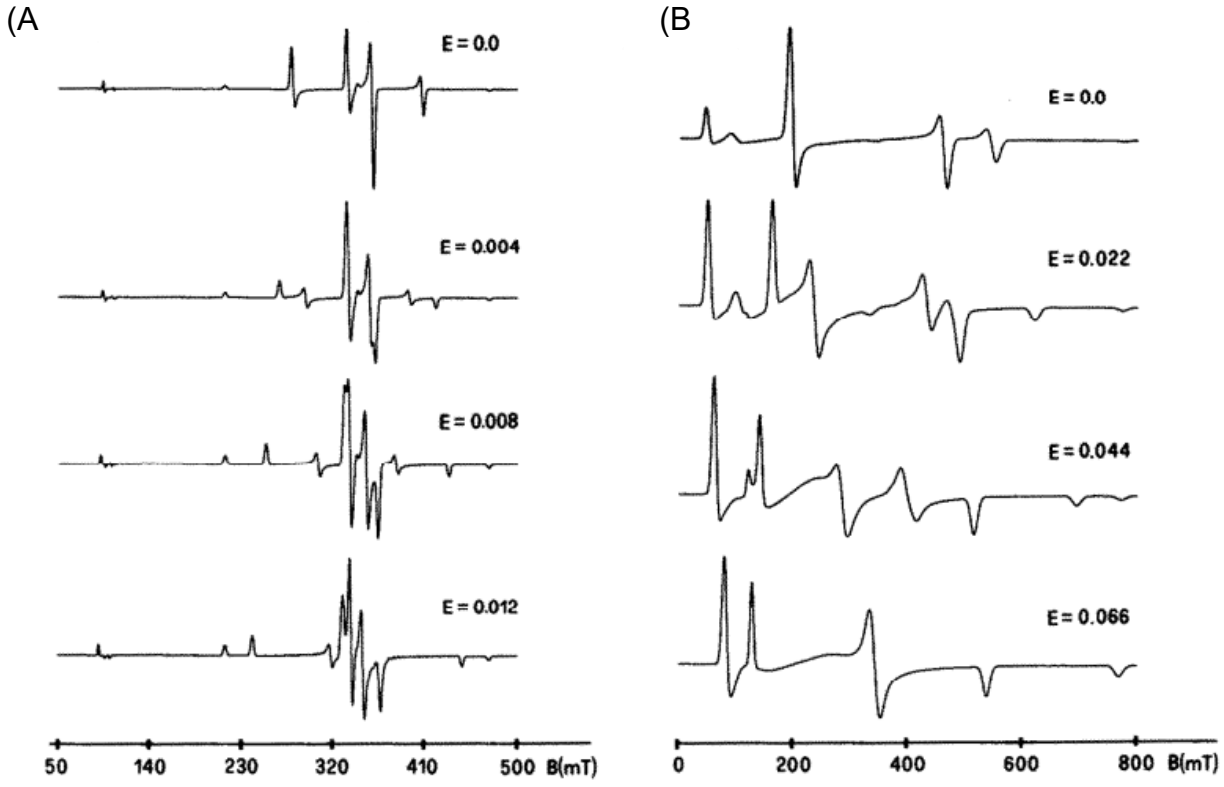

Figure 2.19: Calculated X-band spectra (9.5 GHz) of high spin (S = 3/2) C(III). g_{iso} = 1.98; (A) D = 0,06 cm^{-1} (1 cm^{-1} = 29799 MHz) and (B) D = 0.20 cm^{-1}. Adapted from Figure 1 [38].

Many of the complexes examined within ethylene oligomerization belong to this category and have already been examined in Chapter 1. Other works include studies which have focused on EPR properties of Cr – porphyrins [39], tetragonal complexes

with a $[Cr(NH_3)_4XY]^{n+}$ or $[Cr(py)_4XY]^{n+}$ with X and Y being variable ligands perpendicular to the plane of ammines and pyridines [40], aqueous solution ions and complexes [41], oxalate bearing complexes [42] and salen ligand bearing complexes for epoxidation catalysis [43], among many others.

Chromium IV (s^0d^2) has received some attention as a potential oxidation state in the Cr(II) and Cr (IV) pair of the metalacyclic reaction but there is little EPR data and it primarily focuses on Cr (IV) doping of crystals such as $CdGeAs_2$ [44].

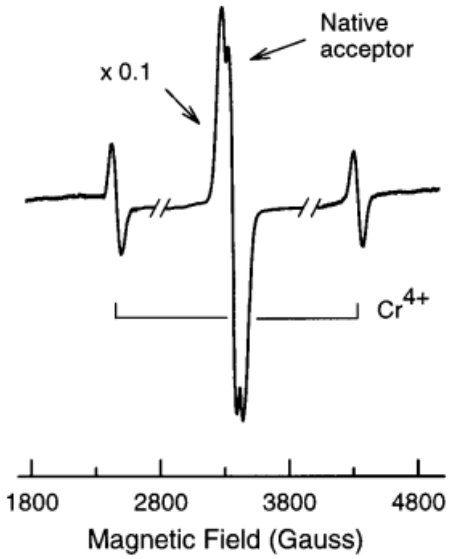

Figure 2.20: spectrum of C(IV) system, (S = 1), g_{iso} = 1.98; D= 17987 MHz; E = 4497. (^{53}Cr hyperfine is omitted for better visualization). Adapted from Figure 1 of [44].

Chromium V is not a particularly common oxidation state, it has an electronic configuration of (s^0d^1) and a single spin system of S = 1/2. It has biological significance in the reduction of Cr(VI) which is a dangerous pollutant in waterways and one of the first to receive legislation regulating its release in the environment. Cr(VI) is transported through organisms through the sulphate channels due to its structural similarities. Once inside, the cell reducing agents transform Cr(VI) into Cr(V) and subsequently Cr(III) which can attach itself to nucleic acids and proteins which explains its high genotoxicity activity [45]. For this reason a significant number of publications have focused on Cr(V) detection as a means to evaluate the speed at which Cr(VI) is being metabolized [46], this also includes a study of in-vivo EPR in mice [47] (in-vivo EPR and EPR imagining suffer from microwave radiation being absorbed by biological tissues but low frequency microwave radiation can penetrate

mice or limb sized systems without causing too much heat transfer [48]). The Phillips Catalyst (not to be confused with the Phillips system described in Chapter 1.4) is a polymerization catalyst system for ethylene introduced in the 1950s [49]. It is a supported, heterogeneous catalyst on silica and accounts for a significant portion of global production of high-density polyethylene (HDPE) [50]. Like its similarly named Phillips system for ethylene oligomerization, there are still many uncertainties about this system such as its actual structure and the redox state of the catalytically active state with Cr(III) / Cr (V) being one of the proposed couples [51].

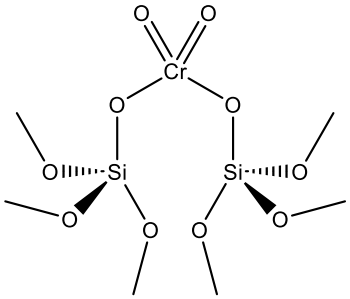

Scheme 2.1: proposed structure of the Phillips catalyst (actual structure of the catalytically active site remains uncertain) [50].

A detailed examination of this system is beyond the scope of this thesis, but several studies have used EPR to attempt to determine the properties of this [52, 53] and similar systems. [54, 55].

Chromium VI (d^0) is diamagnetic and is not observable by EPR.

Bibliography

[1] I. Kuprov, Spin, Springer, 2023.

[2] R. M. Eisberg and R. Resnick, Quantum physics of atoms, molecules, solids, nuclei, and particles, Wiley, 1985.

[3] F. E. Collison and D. Mabbs, Electron Paramagnetic Resonance of D Transition Metal Compounds, Elsevier, 1992.

[4] D. Goldfarb and S. Stoll, EPR spectroscopy: fundamentals and methods, John Wiley & Sons, 2018.

[5] J. A. Bolton and J. R. Weil, Electron paramagnetic resonance: elementary theory and practical applications, John Wiley & Sons, 2007.

[6] V. Chechik, E. Carter and D. M. Murphy, Electron Paramagnetic Resonance, Oxford Press, 2016.

[7] D. M. Murphy, “EPR (Electron Paramagnetic Resonance) Spectroscopy of Polycrystalline Oxide Systems,” in *Metal Oxide Catalysis*, Wiley, 2008, p. 1–50.

[8] A. Schweiger and G. Jeschke, Principles of Pulse Electron Paramagnetic Resonance, Oxford University Press, 2001.

[9] J. Spencer, An Electron Paramagnetic Resonance (EPR) Study of Battery and Functional Materials, PhD thesis., Cardiff University, 2021.

[10] J. Telser, “EPR Interactions - Zero-Field Splittings,” in *EPR Spectroscopy: Fundamentals and Methods*, Wiley, 2018, pp. 207-234.

[11] Roessler and S. E. M., “Principles and applications of EPR spectroscopy in the chemical sciences,” *Chem Soc Rev.,* vol. 47, no. 8, pp. 2534-2553, 2018.

[12] B. Abragam and B. A., Electron paramagnetic resonance of transition ions, 1970, Oxford University Press, 1970.

[13] M. R. Brustolon, Electron Paramagnetic Resonance, a practitioner's toolkit, University of Padua, 2009.

[14] M. Chiesa and E. Giamello, “Encycl. ofAnalytical Chem.,” 2000, p. 1437–1445.

[15] F. Bloch, “Nuclear Induction,” *Phys. Rev.,* vol. 70, no. 7-8, 1946.

[16] J. P. Klare, An Introduction to Pulsed EPR Spectroscopy - A lecture held at the 3rd Workshop on EPR Spectroscopy 06.-08.11.2013, University of Osnabrück, Germany, 2013.

[17] S. Stoll, Frontiers in Chemical Physics Symposium - (University of Washington-Dept of Chemistry), 2018.

[18] E. L. Hahn, “Spin Echoes,” *Phys. Rev.,* vol. 80, no. 4, 1950.

[19] S. Stoll, “Pulse EPR,” *eMagRes,* vol. 6, no. 1, 2017.

[20] L. G. Rowan, E. L. Hahn and M. W. B., “Electron-Spin-Echo Envelope Modulation,” *Phys. Rev.,* vol. 137, no. 1A, 1965.

[21] W. B. Mims, “Envelope Modulation in Spin-Echo Experiments,” *Phys. Rev. B,* vol. 5, no. 7, 1972.

[22] S. Van Doorslaer, “Hyperfine Spectroscopy: ESEEM,” vol. 6, no. 1, 2017.

[23] W. B. Mims, “Pulsed endor experiments,” in *Proceedings of the Royal Society A*, 1965.

[24] W. B. Mims, “Amplitudes of superhyperfine frequencies displayed in the electron spin-echo envelope,” *Phys. Rev. B,* vol. 6, p. 3543, 1972.

[25] A. Schweiger, L. Braunschweiler, J. M. Fauth and R. R. Ernst, “Coherent and Incoherent Echo Spectroscopy with Extended-Time Excitation,” *Phys. Rev. Lett.,* vol. 54, no. 12, p. 1241.

[26] P. Höfer, A. Grupp, H. Nebenführ and M. Mehring, “Hyperfine sublevel correlation (hyscore) spectroscopy: a 2D ESR investigation of the squaric acid radical,” *Chemical Physics Letters,* vol. 132, no. 3, pp. 279-282, 1986.

[27] S. A. Dikanov, A. M. Tyryshkin and M. K. Bowman, “Intensity of cross-peaks in hyscore spectra of S = 1/2, I = 1/2 spin systems,” *J. Magn. Reson.,* vol. 144, no. 2, pp. 228-242, 2000.

[28] G. Feher, “Observation of Nuclear Magnetic Resonances via the Electron Spin Resonance Line,” *Phys. Rev.,* vol. 103, no. 3, p. 834, 1956.

[29] E. R. Davies, “A new pulse endor technique,” *Physics Letters A,* vol. 47, no. 1, pp. 1-2, 1974.

[30] P. H. Rieger, “Electron paramagnetic resonance studies of low-spin d5 transition metal complexes,” *Coordination Chemistry Reviews,* Vols. 135-136, no. C, pp. 203-286, 1994.

[31] S. Clamp, N. G. Connelly, G. E. Taylor and T. S. Louttit, “Synthesis and reactivity of the paramagnetic nitrosyl complexes [M(NO)(NCMe)5]2+(M = Cr or Mo), and the crystal structures of [Cr(NO)(S2CNEt2)3] and [CrF(NO)(dppe)2],” *J. Chem. Soc., Dalton Trans.,* no. 11, pp. 2162-2169, 1980.

[32] P. Legzdins and C. R. Nurse, “Organometallic nitrosyl chemistry. 22. New halo nitrosyl complexes of chromium resulting from the reactions of halogens with (.eta.5-C5R5)Cr(CO)(NO)L (R = H, Me; L = CO, PPh3),” *ACS Catalysis,* vol. 24, no. 3, pp. 327-332, 1985.

[33] N. A. Cooley, M. C. Baird, J. R. Morton, K. F. Preston and Y. Le Page, “The EPR spectrum of CpCr(CO)2P(C6H5)3 in a single crystal of its Mn analog,” *Journal of Magnetic Resonance (1969),* vol. 76, no. 2, pp. 325-330, 1988.

[34] C. C. Scarborough, S. Sproules, C. J. Doonan, K. S. Hagen, T. Weyhermüller and K. Wieghardt, “Scrutinizing Low-Spin Cr(II) Complexes,” *Inorganic Chemistry,* vol. 51, no. 12, pp. 6969-6982, 2012.

[35] P. M. Becker, C. Fçrster, L. M. Carrella, P. Boden, D. Hunger, J. van Slageren, G. Markus, E. Rentschler and K. Heinze, “Spin Crossover and Long-Lived Excited States in a Reduced Molecular Ruby,” *Che. Eur. J,* vol. 26, pp. 7199-7204, 2020.

[36] D. Turnbull, Solid State Physics, Vol. 17, Academic Press Inc., 1965.

[37] P. J. Alonso and J. I. Martinéz, Magnetic Properties of a Kramer's Doublet. An Univocal Bridge Between Experimental Results and Theoretical Predictions, Instituto de Ciencia de Materiales de Aragón (Universidad de Zaragoza); Consejo Superior de Investigaciones Científicas) Facultad de Ciencias, Universidad de Zaragoza, 2020.

[38] R. P. Bonomo and A. J. Bilio, “EPR investigation of chromium (III) complexes: analysis of their frozen solution and magnetically dilute powder spectra,” *Chemical Physics,* vol. 151, pp. 323-333, 1990.

[39] D. A. Summerville, R. D. Jones, B. M. Hoffman and F. Basolo, “Chromium(III) porphyrins. Chemical and spectroscopic properties of chloro-meso-tetraphenylporphinatochromium(III) in nonaqueous solutions,” *Journal of the American Chemical Society,* vol. 99, p. 8195–8202, 1977.

[40] E. Pendersen and H. Toftlund, “Electron Spin Resonance Spectra of Tetragonal Chromium(III) Complexes. I. trans-[Cr(NH3)4XY]n+ and trans-[Cr(py)4XY]n+in Frozen Solutions and Powders. A Correlation between Zero-Field-Splittings and Ligand Field Parameters via Complete d-Electron Calcula-,” *Inorganic Chemistry,* vol. 13, no. 7, pp. 1603-1612, 1974.

[41] N. Shaham, H. Cohen, D. Meyerstein and E. Bill, “EPR Measurements corroborate information concerning the nature of (H2O)5CrIII–alkyl complexes,” *J. Chem. Soc., Dalton Trans,* pp. 3082-3085, 2000.

[42] W. T. M. Andriessen, “Electron Paramagnetic Resonance and Line Width Behavior of trans-Bis(oxalato)chromium(III) Complexes in Frozen Solution,” *Inorganic Chemistry,* vol. 14, no. 4, pp. 792-795, 1975.

[43] K. P. Bryliakov and E. P. Talsi, “CrIII(salen)Cl Catalyzed Asymmetric Epoxidations: Insight into the Catalytic Cycle,” *Inorganic Chemistry,* vol. 42, no. 22, pp. 7258-7265, 2003.

[44] N. Y. Garces, N. C. Giles, L. E. Halliburton, K. Nagashio, R. S. Feigelson and S. P. G., “Electron paramagnetic resonance of Cr(II) and Cr(IV) ions in CdGeAs2,” *Journal of Applied Physics,* vol. 94, pp. 7567-7570, 2003.

[45] Y. Xie, S. Holmgren, D. M. K. Andrews and M. S. Wolfe, “Evaluating the Impact of the U.S. National Toxicology Program: A Case Study on Hexavalent Chromium,” *Environmental Health Perspectives,* pp. 181-188, 2017.

[46] D. M. L. Goodgame and M. A. Joy, “EPR study of the Cr(V) and radical species produced in the reduction of Cr(VI) by ascorbate,” *Inorganica Chimica ACTA,* vol. 135, no. 2, pp. 115-118, 1987.

[47] K. J. Liu, J. J. Jiang, H. M. Swartz and X. G. Shi, “Low-Frequency EPR Detection of Chromium(V) Formation by Chromium(VI) Reduction in Whole Live Mice,” *Archives of Biochemistry and Biophysics,* vol. 313, no. 2, pp. 248-252, 1994.

[48] G. R. Eaton and S. S. Eaton, EPR Imaging and In Vivo EPR, CRC press, 2018.

[49] J. P. Hogan and R. L. Banks, “Polymers and production thereof”. United States of America Patent US2825721A, 4 March 1958.

[50] M. P. McDaniel, “Chapter 3 - A Review of the Phillips Supported Chromium Catalyst and Its Commercial Use for Ethylene Polymerization,” *Advances in Catalysis,* vol. 53, pp. 123-606, 2010.

[51] E. Groppo, G. A. Martino, A. Piovano and C. Barzan, “The Active Sites in the Phillips Catalysts: Origins of a Lively Debate and a Vision for the Future,” *ACS Catalysis,* vol. 8, no. 11, p. 10846–10863, 2018.

[52] B. M. Weckhuysen, R. A. Schooheyydt, F. E. Mabbs and C. David, “Electron Paramagnetic Resonance of Heterogeneous Chromium Catalysis,” *J. Chem. Soc., Faraday Trans.,* vol. 92, no. 13, pp. 2431-2436, 1996.

[53] B. M. Weckhuysen and R. A. Schoonheydt, “Alkane dehydrogenation over supported chromium oxide catalysts,” *Catalysis Today,* vol. 51, no. 2, pp. 223-232, 1999.

[54] Y.-K. Liao, P. C. Bruzzese, M. Hartmann, A. Pöppl and M. Chiesa, “Chromium Environment within Cr-Doped Silico-Aluminophosphate Molecular Sieves from Spin Density Studies,” *Journal of Physical Chemistry C,* vol. 125, no. 15, pp. 8116-8124, 2021.

[55] L. Yu-Kai, Paramagnetic Transition Metal Ions on Oxide Surfaces: an EPR Investigation (Thesis), 2022.

[56] J. Telser, L. A. Pardi, J. Krzystek and L.-C. Brunel, “EPR Spectra from “EPR-Silent” Species: High-Field EPR Spectroscopy of Aqueous,” *Inorganic Chemistry,* vol. 37, pp. 5769-5775, 1998.

Chapter 3
Experimental

3.1 General synthetic laboratory equipment

The paramagnetic chromium (I) state is an uncommon oxidation state because of its intrinsic reactivity towards redox reaction so all sample handling requires minimizing contact with any source of O_2 and H_2O. For this purpose, Schlenk lines were required for the synthesis of all compounds investigated in this Thesis, while gloveboxes were used for sample handling and preparation. Therefore, a brief overview of the laboratory equipment and handling procedures undertaken during the course of this work are given below.

3.1.1 Schlenk lines

A Schlenk line is a system of pumps and tubes designed to provide both a vacuum and controlled atmosphere, usually of nitrogen or argon, when synthesising air sensitive samples. The design is modular, with the possibility to attach and detach elements as needed and, with some care, operate several reactions in parallel. The system was originally devised by Wilhelm Schlenk in 1913 for the synthesis of ketyl radical anions [1]. The Schlenk line, and the degree of standardization of its components has been a success of contemporary chemistry and it is difficult, at present, to imagine a synthetic chemistry laboratory without one [2].

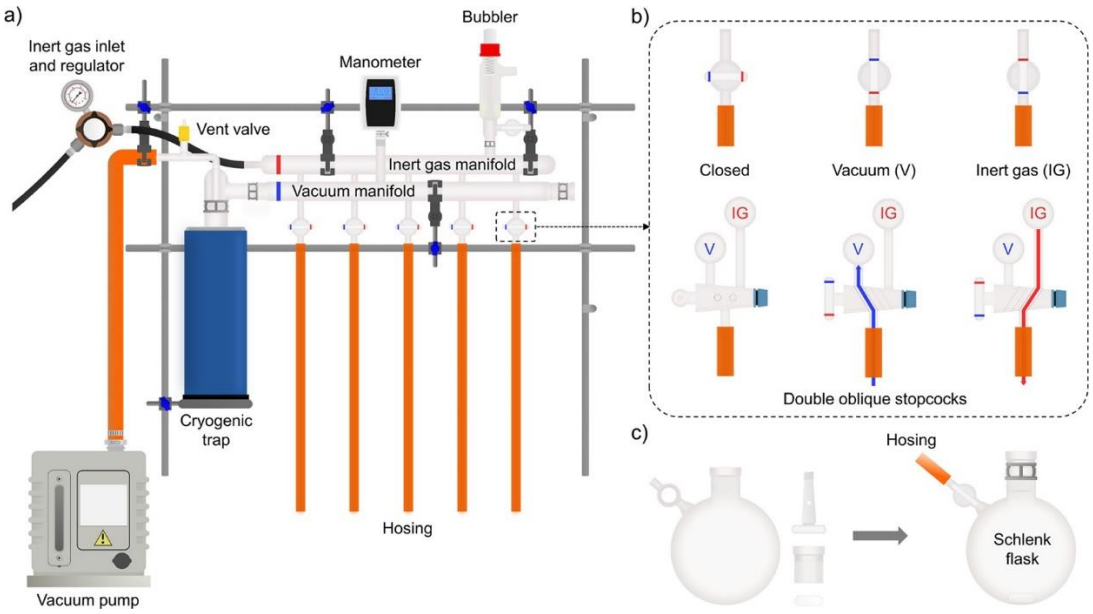

Figure 3.1: Basic schematic of a Schlenk line system and its individual components [1].

The system operates by having a low vacuum pump that removes all air from the system which is then replaced on demand with inert gas. Nitrogen and argon are the most commonly used inert gasses, and argon is typically regarded as the superior to nitrogen, but more expensive, since N_2 can react with some materials and Ar is denser than air so it tends to form a protective layer even if small amounts of air enter the system. The pump itself is protected from the influx of solvents and other volatile chemicals by a cold trap, cooled with liquid nitrogen. Schlenk lines cannot operate at high gas pressures and have relief valves to prevent explosions, but the system can switch between modes very easily and even provide constant flow of gas (counter-flow) as a temporary shield against the atmosphere for certain operations (such as connecting two flasks or introducing a reagent).

In a typical test reaction, all glassware is heated for an extended period to at least 75° C to dry the components as much as possible, removing residual traces of moisture. Then the still hot Schlenk flask is connected to a system where all atmosphere is purged by alternating vacuum and inert gas.

Solvents to be used in the glovebox (referred to as ‘degassed’ solvents in Chapters 4 and 5) are prepared by taking an anhydrous solvent, placing it in a Schlenk flask while under nitrogen flow conditions and then freezing the solvent with liquid nitrogen. In its solid and cooled state, it is possible to evacuate the atmosphere above the solvent

and then restore nitrogen or argon atmosphere while allowing the solvent to thaw. This process called *freeze-thaw degassing* needs to be repeated several (at least three) times and was used to prepare the dichloromethane, tetrahydrofuran solvents used in all experiments reported in this work.

3.1.2 Gloveboxes

A glovebox is a sealed chamber, isolated from external atmosphere and filled with a chosen gas, typically an inert one such as nitrogen or argon. As the name implies, a set of rubber gloves allows the operator to manipulate objects inside the protected chamber without affecting the internal atmosphere. In ideal conditions a glovebox will have less than 1 ppm of both O_2 and H_2O, which are the main parameters monitored and maintained automatically by the device. In practice it is not uncommon for O_2 values to rise which means the scrubber unit needs to undergo a regular regeneration cycle. The gloveboxes used in this work were primarily argon based though two nitrogen-based ones were also occasionally used. Besides providing the operator with the location to prepare EPR samples, the glovebox and the freezer within (when available) were the primary long-term storage units of all powder complexes, degassed solvents and pre-prepared stock solutions of the Cr(I) complexes. With the freezer module (not available during the secondment periods) the samples were functionally stable over extended periods of time even when inspected over a year later.

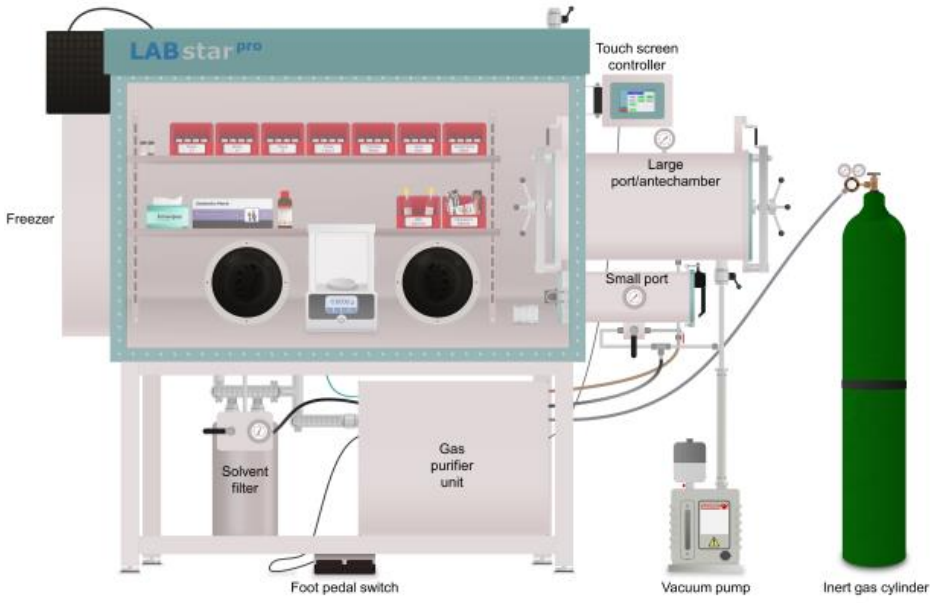

Figure 3.2: Schematic illustration of a typical glovebox [4].

Materials are brought in and out of the glovebox using the side ports, alternating 3 times between vacuum and inert gas. Care must be taken during this step to allow for all pockets of gas to be released during the vacuum phase (to prevent contamination from O_2 and also that all sealed containers (such as the Schlenk tubes containing degassed solvents) are rated to withstand a vacuum to prevent explosion.

A typical sample solution preparation consists of mixing the desired amount of Cr(I) complex in crystalline/powder form with 5 mL of DCM which are kept in a screw top vial, with Teflon tape wrapped around the screw section to ensure as little of the solvent is lost due to evaporation.

A Wilmad EPV 7 EPR airtight quartz tube is filled with between 0.1 mL and 0.2 mL of solution within the glovebox. This type of tube is sufficiently airtight to ensure the sample will be usable at least for 24 hours. In the case of the photo- or chemical-reactivity studies the tube is kept frozen at all times except during EPR measurements.

3.2 EPR spectrometers

3.2.1 Continuous Wave (CW) EPR spectrometers

The main spectroscopic technique used in this Thesis is Electron Paramagnetic Resonance (EPR), and the theory of this technique was covered in detail in Chapter 2. An EPR spectrometer is to some extent of a modular design with many components that can be swapped or replaced from variable temperatures units to electrochemical capabilities to rapid scan components, etc [5].

The spectrometers used in this project are the Bruker EMX and Bruker E500 series equipped with X-band cavities and suitable temperature control units. The cooling element on the Bruker EMX spectrometer operates with a flow of nitrogen gas cooled by circulation in a coil immersed in a liquid nitrogen dewar, and this system can achieve temperatures as low as 120 K, although more typical values were around 140 K. The Bruker E500 spectrometer was set up with a gas transfer arm that could be connected directly to a suitable dewar. A heating element within the transfer arm boiled liquid nitrogen from the dewar and delivered the cold gas to the cavity, allowing this system to reach temperatures as low as 100-90 K. During the secondment period at Turin University, the EMX spectrometer used a quartz finger dewar that could be fitted directly inside the cavity which housed the sample tube in direct immersion. With this

setup the only possible temperature obtained is 77 K; although a lower temperature is reached, this system suffers from the disadvantage of bubbling caused by the evaporating nitrogen, which in turn introduce mechanical vibrations to the sample.

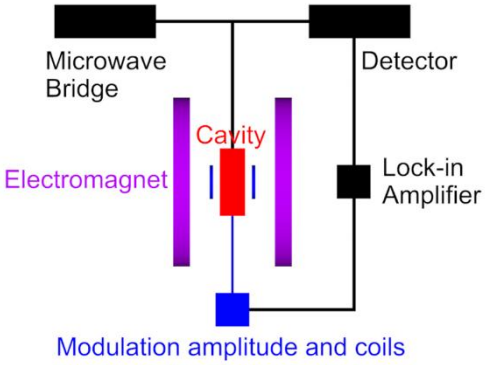

Figure 3.3: Basic schematic illustration of a CW-EPR spectrometer.

A full review of every component of a continuous wave spectrometer is beyond the scope of this Thesis, so only a brief overview will be covered here. The microwave bridge is the source of radiation in most EPR applications, which employ either a Klystron or Gunn diode at their core (Figure 3.3). Unlike many sources in the radiofrequency range, a typical Gunn diode cannot be swept over a large range which is why most experimental setups will sweep the magnetic field rather than the frequency. Microwave radiation exits the operational end of the bridge through a slit connected to a metal waveguide. The full output of a microwave bridge is typically far too powerful to be used directly, so an isolator element attenuates the amount of microwave energy that is allowed through. In practical terms this is how the operator chooses the experimental microwave power which for most experiments in this Thesis was set to *ca.* 10 mW. The microwave is then split and sent into detector and the resonator elements through their own waveguides, but phase shifted by 180°. Phase sensitive detectors can compare the microwave energy from the bridge and subtract the reflected microwave energy from the resonator. This allows the signal to be recorded as an absorbance and is less sensitive to fluctuations of the source.

For an X band (~9.5 GHz) or Q band (~33 GHz) spectrometer, the magnetic field range is achievable with most modern electromagnets, typically water cooled. These are far less complex than those needed in W band (~95 GHz) which need to be helium cooled

superconducting magnets. It is also relatively easy to perform a field intensity sweep with these systems.

Perhaps one of the more crucial components of the spectrometer is its cavity. Here the microwave bridge is allowed to interact with the sample. A resonator cavity will convert the incoming radiation into a standing wave inside the cavity. In this configuration the components of the electromagnetic wave can be separated so that there are regions inside the cavity where the magnetic field component is at its highest and the electric field component is at its lowest. It is thus possible to subject the sample to a magnetic field while largely excluding the dielectric heating effect. To achieve this state the geometry of the cavity and the incoming microwave radiation need to create a resonance state, so an iris screw at the entrance of the cavity allows the operator to manually adjust the overall geometry to reach this state. The Q-factor for a cavity is a measure of how effective the cavity is at storing energy without reflecting any of it back to the detector or dissipating it [5].

$$Q = \frac{\nu}{\Delta\eta} = \frac{2\pi(energy\ stored)}{(energy\ dissipated)} \tag{3.1}$$

Most cavities used for CW-EPR measurements contain an additional series of coils that introduce an oscillating magnetic field, typically at 100 KHz frequency and with ranges between 0.5 mT and 0.05 mT (most results reported in this Thesis have 0.1 mT modulation amplitude). This additional magnetic field makes every point recorded on the spectrometer an average of the point itself and all points within the modulation amplitude range. This is a great method of increasing the signal to noise ratio in transition metal spectra but care must be taken in making sure that small features are not averaged out. One of the consequences of using field modulation is that the signal in CW- EPR is obtained in first derivative mode of the absorbance.

In a standard operation the sample is loaded into an EPR tube inside the glovebox. The spectrometer is then turned on; the cooling system is activated, and the temperature control system is readied, if needed. Once the cavity has reached the desired temperature, the spectrometer is tuned by controlling the iris screw, frequency, phase and power. If the tuning procedure has been performed correctly the cavity should be critically coupled and the spectrometer should remain tuned even when changing the microwave power (in practice this state is not always possible to achieve, depending on the solvent some degree of adjustment when changing power is always

required). The cavities used for the photochemistry experiments have an optical slit to allow line of sight with a chosen light source.

3.2.2 Pulsed EPR spectrometers

The theory of pulsed EPR spectroscopy was already covered in Chapter 2. A pulsed spectrometer has some additional components compared to a CW-EPR spectrometer, whilst some components act differently. The microwave bridge is designed to provide short and powerful bursts of microwave radiation while a pulse generator shapes these bursts into the controlled sequences of microwave pulses that are necessary for pulsed EPR. The cavity also has to be designed specifically for use in pulsed EPR and as such they are not interchangeable with CW-EPR systems. As a pulse spectrometer measures the spin echo and thus almost always operate at very low temperature (30 K to 10 K in the case of ENDOR and HYSCORE experiments) requiring a steady flow of helium gas from a transfer arm connected to a liquid helium dewar. As such a pulsed spectrometer is more expensive to operate and usually reserved for those experiments where a CW spectrometer would be insufficient.

Two Bruker E580 series spectrometers were used for this Thesis during the secondment periods in the Universities of Turin and Antwerp. The spectrometer in Turin University could be fitted with either an X-band cavity or Q-band cavity while the system in Antwerp University was operated only with an X-band cavity. Both of these instruments also had a radiofrequency generator for ENDOR measurements.

The tuning procedure for an E580 spectrometer is more complex than that for a CW system as it requires the operator to first locate the echo of the species under study. Each individual technique, such as pulse ESEEM or HYSCORE, have a preset that the user can load and adjust to meet their needs in optimising the signal and pulse sequence.

The cavity used for liquid helium operations is not compatible with the Wilmad EPV 7 EPR tubes so regular EPR tubes had to be employed. To preserve the sample from contact with the atmosphere, the tubes were sealed using Teflon wrap. In Antwerp University special caps were 3D printed to be used in conjunction with Teflon wrap. While this type of seal is far inferior to the one provided by EPV 7 EPR, it was still sufficient for the task of preserving the sample long enough to be inserted in the spectrometer, especially if kept in liquid nitrogen once outside the glovebox.

3.3 Radiation light sources

A Scitech Tuneable Light Source (abbreviated to TLS) was used as the primary source of light in narrow band irradiation experiments. This device has a white light emitter with a series of filter wheels and a diffraction monochromator to obtain light of a chosen wavelength with a band of 2 nm. The wavelength selection is between 650 nm and 350 nm. The power at the source cannot be calculated exactly as the optical window intercepts a fraction of the outgoing power but the power measured at the optical slit was of 500 mW.

Two Labino LED torches one with a peak emission at 365 nm and one with a peak emission at 505 nm were used from broad band irradiation experiments (bandwidth of 50 nm). The calculated power at the optical slit was of 950 mW.

3.4 Materials

The following section contains a comprehensive list of all the solvents and liquid reagents used in this Thesis, including the source, and purification steps if relevant.

Dichloromethane (DCM): This was acquired from the Solvent Purification System (SPS) of Cardiff University, degassed using the freeze-thaw procedure, preserved with molecular sieves and kept in a Schlenk Flask within the glovebox at all times. For the experiments conducted during the secondment periods, the DCM was acquired from the organic chemistry laboratory at Turin University, degassed by the freeze-thaw procedure, preserved with molecular sieves and kept in a Schlenk Flask within the glovebox at all times.

Tetrahydrofuran (THF): This was acquired from the Solvent Purification System (SPS) of Cardiff University, degassed with the freeze-thaw procedure, preserved with molecular sieves and kept in a Schlenk Flask within the glovebox at all times.

1-hexene: This was purchased from Thermofisher (99.9%) in a glass vial bearing an acroseal septum already packaged under nitrogen atmosphere. The sample (once opened) was preserved in a glovebox and used as delivered. The deuterated 1-hexene (with 99.9% purity) was purchased from Cambridge Isotope Laboratories in a

sealed glass vial under nitrogen atmosphere, opened in glovebox and preserved in a screw cap vial. The sample was used as delivered.

Triethylaluminium (TEA): This was purchased from Thermofisher (as a 0.7 M solution in heptane) in a bottle with an acroseal septum already packaged under nitrogen atmosphere. The opened bottle was preserved in glovebox and used as delivered.

Hexene Isomers: Cis 2-hexene, Trans 2-hexene, Cis 3-hexene, and Trans 3-hexene, were all purchased from Thermofisher (98%) and packaged under a nitrogen atmosphere. The opened glass vials were preserved in a glovebox and used as delivered.

The following section contains a comprehensive list of all the solid compounds used in this Thesis.

Chromium hexacarbonyl ($Cr(CO)_6$): The starting Cr(0) hexacarbonyl complex was purchased from Sigma-Aldrtich and used as received. The sample was stored in its original container throughout.

Silver tetrakis(perfluoro-tert-butoxy)aluminate ($Ag[Al(OC(CF_3)_3)_4]$): The silver salt used in the synthesis step was purchased from Iolitec, stored in the glovebox and used as delivered.

1,3-Bis(diphenylphosphino)propane ($Ph_2PC_3H_6PPh_2$): The phosphine ligand used for the synthesis of the compounds presented in Chapter 4 were purchased from Sigma Aldrich and used as delivered.

Bis[2-(diphenylphosphino)ethyl]amine $HN(CH_2CH_2PPh_2)_2$: This ligand was previously prepared by the Wass research group at Cardiff University and used as received.

Phenanthroline and Bipyridine: Both compounds were purchased from Sigma Aldrich and used as received.

Bibliography

[1] A. M. Borys, "An Illustrated Guide to Schlenk Line Techniques," *Organometallics,* vol. 42, no. 3, pp. 175-284, 2023.

[2] W. Schlenk and A. Thal, "Über Metallketyle, eine große Klasse von Verbindungen mit dreiwertigem Kohlenstoff II," *Ber. Dtsch.Chem.Ges.,* vol. 46, no. 3, pp. 2840-2854, 1913.

[3] T. T. Tidwell, " Wilhelm Schlenk: The Man Behind the Flask," *Angew.Chem.,Int. Ed.,* vol. 40, pp. 331-337, 2001.

[4] JoVE, Cambridge, "Laboratory Safety, Operating the Glovebox," JoVE Science Education Database, 2023.

[5] V. Chechik, E. Carter and D. Murphy, Electron Paramagnetic Resonance, Oxford University Press, 2016.

Chapter 4

A CW-EPR Investigation of the photochemical intermediates formed from the chromium(I) complex, $[Cr(CO)_4$bis(diphenylphoshino)$]^+$ and its reactions with 1-hexene

4.1 Introduction

For many years, ethylene trimerisation and tetramerization have been a widely sought-after transformation leading to the formation of linear alpha-olefins (LAO's) [1]. These are highly valuable chemicals used in the production of low-density polyethylene, surfactant precursors and synthetic lubricants. The shorter chain LAO's, such as 1-hexene and 1-octene are particularly important, and therefore a number of successful catalysts have been developed based on chromium with suitable ancillary ligands employing bis(phosphino)amines and bis(sulfanyl)amines moieties, which avoid the wide product distribution observed with traditional ethylene oligomerisation catalysts [2, 3, 4, 5, 6, 7, 8]. These chromium-based catalysts have been found to be particularly effective for the selective trimerisation of ethylene to 1-hexene [9], and are generally considered to operate through a metalacyclic mechanism [10, 11]. Despite their commercial success and considerable scientific investigations to date, the detailed mechanistic insights into the reaction cycle still remains elusive, particularly with respect to the oxidation states of the active chromium centres during the catalytic cycle and the redox couple involved in the chemistry.

In most cases, these Cr-based complexes are generally activated prior to use in the catalytic reaction with ethylene, usually by using Al based activators such as methylaluminoxane (MMAO) or $AlEt_3$ (TEA) [1]. Most recently, combined EPR, XAS and computational studies have focussed on these challenging mechanistic studies following catalyst activation with these precursors [12, 13, 14]. Chromium I, II and III oxidation states have all been invoked depending on the nature of the catalysts and the activator used. However, early work showed that cationic Cr(I) complexes of the form $[Cr(CO)_4(L)]^+$ where L = a PNP ligand ($Ph_2PN(R)PPh_2$), can also be successfully

used for ethylene tetramerization in the presence of a weakly coordinating anion, such as $[Al(OC(CF_3)_3)_4]^-$, along with excess $AlEt_3$ [15]. In order to produce the active catalysts, the carbonyl ligands must be removed to enable ethylene coordination and thereby enable oxidative coupling from the metallacycle intermediate, so both UV photolysis and direct reaction with $AlEt_3$ were considered as a means of decarbonylation, with the latter step in particular found to create an effective and active catalysts [3]. We therefore studied the nature of the paramagnetic speciation that occurs when these $[CrCO_4(L)]^+$ type complexes [15] were activated using triethylaluminium ($AlEt_3$) [16, 17]. Indeed, successful decarbonylation of the pre-catalyst complexes was found to occur rapidly, resulting in the formation of several different types of unstable complexes, including Cr(I)-bis-η^6-arene complexes [16] and 'piano-stool' type species $[Cr(CO)_2(L)]^+$ [17] as evidenced by EPR spectroscopy.

Rucklidge *et al*., [3] also showed by IR spectroscopy that UV irradiation of the complex in solution could result in the loss of the carbonyl bands associated with the cationic $[CrCO_4(L)]$ starting complex with concomitant formation of new carbonyl bands suggestive of formation of a Cr(0) complex, whilst also indicating (from quantitative analysis of the data) that some of the Cr centres no longer possessed any coordinated CO ligands.

Interestingly, UV decarbonylation alone did not produce an active catalyst from the cationic $[Cr(CO)_4(L)]^+$ complex unless, it was proposed, a scavenger species was present to permanently remove the carbonyl ligands from Cr [3]. Using EPR spectroscopy, we recently studied the photochemistry of the cationic $[Cr(CO)_4(L)]^+$ complex ($[Cr(CO)_4(Ph_2P(C_3H_6)PPh_2)]^+$ (1,3 bis-(diphenylphosphino)propane, $Ph_2P(C_3H_6)PPh_2$ = dppp), following UV irradiation in order to identify and characterise the nature of any paramagnetic complexes formed [18]. Despite extensive photochemistry and photoelectrochemistry studies of Cr(0) metal carbonyl complexes [19, 20, 21, 22, 23] there have been relatively few photochemistry studies performed on the air-sensitive Cr(I) complexes. Rieger did study the influence of UV irradiation on the electrochemically generated *fac*- and *mer*-$[Cr(CO)_3(\kappa^1\text{-}L_2)(\kappa^2\text{-}L_2)]^+$ (L_2 = bidentate phosphine, abbreviated as dppe) complexes using EPR [24] whereby the *mer*- complex was shown to lose CO in a photochemical UV driven transformation to produce the *trans*-$[Cr(CO)_2(L_2)_2]^+$ complex. In our previous study, we found that room temperature UV irradiation of a similar Cr(I) complex resulted in the rapid

transformation of $[Cr(CO)_4(dppp)]^+$ into a *trans*-$[Cr(CO)_2(dppp)_2]^+$ complex, whereas low temperature (77 – 120 K) UV irradiation revealed the presence of a transient intermediate, the *mer*-$[Cr(CO)_3(\kappa^1\text{-dppp})\ (\kappa^2\text{-dppp})]^+$ complex [18]. The photo-induced reaction was shown to be concentration dependent, with a bimolecular mechanism proposed to account for the formation of *mer*-$[Cr(CO)_3(\kappa^1\text{-dppp})\ (\kappa^2\text{-dppp})]^+$ and *trans*-$[Cr(CO)_2(dppp)_2]^+$ along with indirect evidence for the additional formation of EPR silent Cr(0) and/or Cr(I) centres in solution based on the EPR analysis [18], similar to the findings of Rucklidge *et al*., [3].

Owing to the importance of the many experimental variables in this photochemistry, including sample concentration, temperature, wavelength and power, we sought to explore further the effects of UV irradiation on this important class of $[Cr(CO)_4(dppp)]^+$ complex using EPR spectroscopy, and in particular identify any new complexes formed following the addition of 1-hexene to the UV treated complex.

4.2 Experimental

The experimental conditions used in the preparation of the air sensitive $[Cr(CO)_4(dppp)]^+$ complex (**1**) was described in detail elsewhere [17]. In brief, the necessary manipulations in the preparation and handling of the complexes were carried out under a dry and inert atmosphere (N_2 or Ar) using standard Schlenk-line and glovebox techniques. The dppp ligand and the silver tetrakis(perfluoro-tert-butoxy)aluminate ($Ag[Al(OC(CF_3)_3)_4]$) were purchased from Sigma and Iolitec respectively. The neutral $[Cr(CO)_4(dppp)]$ and cationic $[Cr(CO)_4(dppp)]^+$ $[Al(OC(CF_3)_3)_4]^-$ complexes were synthesised according to literature procedures [5]. The spectroscopic properties of these two compounds (^1H, ^{13}C, ^{19}F and ^{31}P NMR, IR, MS) were consistent with literature data [17]. 1-hexene and the other hexene isomers were purchased from Thermofisher and used as is. The fully deuterated 1-hexene-d12 was purchased from Cambridge Isotope Laboratories.

Sample preparation for EPR measurements: All sample preparations carried out in an Ar or N_2 glovebox. 4.63 mg of $[Cr(CO)_4(dppp)]^+[Al(OC(CF_3)_3)_4]^-$ were dissolved in 3 mL of dichloromethane (DCM) to obtain a solution 1 mM of Cr complex (**1**) in DCM. The sample was stored at 253 K in a screw cap vial to prevent the solvent innate

volatility; the samples are reasonably stable under these conditions over extended periods of time. For EPR analysis, Wilmad LPV-7 EPR tubes bearing airtight caps were used and found to be reliable up to 24 hrs once outside the glove box. The total volume used for EPR analysis was 150 µL; where dilution was necessary, an aliquot was taken from the stock solution inside the glovebox and the requisite amount of DCM added to give a total volume of 150 µL within the EPR tube. UV irradiation was performed using different light sources inside the EPR cavity. Great care was needed to correctly align the sample to the cavity-slit and ensure that all the entire sample volume is irradiated. UV irradiation was conducted using either a Labino UVG 2.0 Torch UV LED light source with an output power of 112 mW at the sample (50 nm bandwidth centred at 365 nm). Alternatively, a Scitech Tuneable Light System (abbreviated TLS) was used for the narrow band irradiation at different wavelengths (2 nm bandwidth with selectable wavelengths between 700 nm and 350 nm).

EPR Instrumentation: The continuous wave (CW) EPR spectra were recorded on an X-band Bruker EMX spectrometer operating at 100 kHz field modulation frequency, 1 Gauss field modulation amplitude, 10 mW microwave power, and equipped with a high-sensitivity cavity (ER 4119HS). EPR computer simulations were performed using the Easyspin [25] toolbox operating in the Mathworks Matlab environment.

Details of DFT calculations: On the basis of our previous work, geometry was optimised using Turbomole27 at the uBP86/def2-TZVP level of theory and confirmed as a true minimum via harmonic frequency calculation. Hyperfine coupling and g tensor data was calculated in ORCA 31 PBEO level of theory, 32 with EPR-II basis set for C and H, 33 def2-TZVP(-f) basis set for P,30 and the Core Properties (CP) basis set (defined in ORCA for 1st row transition metals) for Cr [26].

4.3 Results and Discussion

4.3.1 Overview of the Cr(I) Photochemistry for $[Cr(CO)_4(dppp)]^+$

The CW X-band EPR spectrum of the starting $[Cr(CO)_4(dppp)]^+$ complex (**1**) is shown in Figure 4.1. The structure of this complex (**1**) is also shown in Scheme 4.1. A similar series of EPR spectra has previously been reported by us for analogous Cr(I) bis(diphenylphosphino) type complexes [15]. Therefore, only a brief summary of the spin Hamiltonian parameters will be presented here, in order to clearly distinguish these parameters for (**1**) compared to the newly formed complexes presented in this

work following UV irradiation and treatment with 1-hexene. The frozen solution CW-EPR spectrum of (**1**) is characterised by an axial *g* profile and well resolved super-hyperfine structure arising from the two equivalent ^{31}P nuclei (I =1/2) of the dppp ligand responsible for the 1:2:1 intensity pattern. The hyperfine structure associated with the Cr(I) centre is not visible (in frozen solution) owing to the low natural abundance of ^{53}Cr (I =3/2, ca. 9.5%) and the intrinsic board line width of the signal.

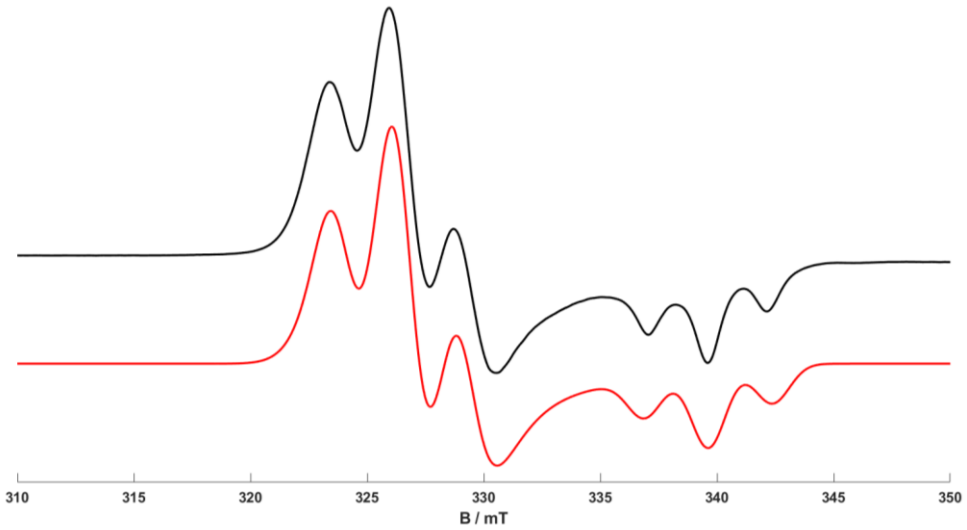

Figure 4.1: X-band CW-EPR spectrum of the $[Cr(CO)_4(dppp)]^+$ complex (**1**) recorded at 140 K (1 mM of (**1**) in dichloromethane, DCM). The corresponding simulation is shown in red font.

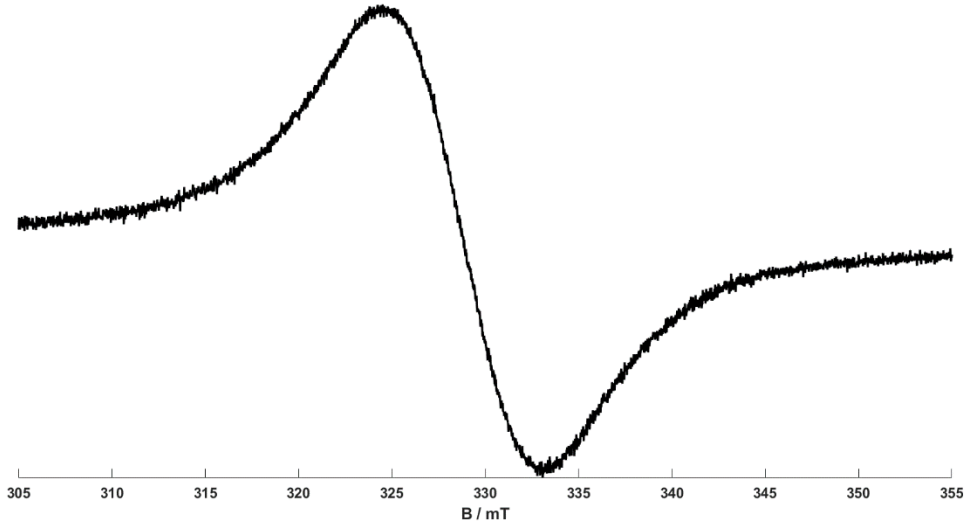

Figure 4.2: X-band CW-EPR spectrum of the $[Cr(CO)_4(dppp)]^+$ complex (**1**) recorded at 292 K (1 mM of (**1**) in dichloromethane, DCM).

The spin Hamiltonian parameters for (**1**) (Table 4.1) are consistent with a six-coordinate Cr(I) environment and the strong ligand field splittings between the t_{2g} and e_g orbitals, created by the carbonyl and phosphino ligands. This large splitting is ultimately responsible for the observed low spin Cr(I) state (S = 1/2). In general for any d^5 system, the tetragonal distortion away from O_h to D_{4h} symmetry creates a ground state $(d_{xy})^2(d_{xz},d_{yz})^3$ or $(d_{xz},d_{yz})^4(d_{xy})^1$ electron configuration depending on whether the ligand field splitting Δ_{LF} is positive or negative, respectively [23]. Simple ligand field arguments predict a $(d_{xz},d_{yz})^4(d_{xy})^1$ ground state for $[Cr(CO)_4(dppp)]^+$, as π-back donation to CO stabilises d_{xz}, d_{yz} relative to d_{xy}. As a result, the d_{xz} and d_{yz} orbitals lie just below the SOMO (*i.e.*, $E_{xz\text{-}yz}$ -E_{xy} is small and positive), while $d_{x2\text{-}y2}$ will be empty and much higher in energy (*i.e.*, $E_{x2\text{-}y2}$ - E_{xy} is large and negative). One therefore predicts that g_{xx} and g_{yy} should be significantly larger than g_e (producing a positive g shift), due to the admixture of the excited state resulting from promotion of an electron from the doubly occupied $d_{xz,yz}$ to the singly occupied d_{xy} orbital. For g_{zz}, a negative g shift will be expected, arising from the promotion of the electron from d_{xy} into the empty $d_{x2\text{-}y2}$ orbital. These estimated trends are all observed experimentally, with $g_\perp$ (g_{xx} = g_{yy}) = 2.068 and $g_e > g_{||}$ (g_{zz}) = 1.991 (Table 4.1), agreeing with a d_{xy} ground state of $[Cr(CO)_4(dppp)]^+$.

When this $[Cr(CO)_4(dppp)]^+$ complex (**1**) is exposed to UV radiation (from a broad band light source, using the Labino UVG 2.0 UV LED light; peak maximum at 365 nm) at room temperature, the deep blue colouration of the solution is immediately bleached resulting in an almost colourless solution. The original EPR spectrum of the starting complex (Figure 4.1) is subsequently transformed into a new signal arising from a *trans*-$[Cr(CO)_2(dppp)_2]^+$ complex (**3**) [18]. This new *tran*s- complex (**3**) is the only observable EPR signal (with 100% contribution to the signal) following room temperature UV irradiation of (**1**) [18]. This photochemical transformation of (**1**) into the *trans*- complex, rather than the *cis*- complex was in agreement with the known preference for the stabilization of *trans*- Cr(I) complexes compared to their *cis*-counterparts [24]. In contrast, when the UV irradiation was conducted at lower temperatures (typically 77-120 K), an intermediate species in this photochemical transformation was identified by EPR. This intermediate was assigned to a *mer*-$[Cr(CO)_3(\kappa^1\text{-dppp})\ (\kappa^2\text{-dppp})]^+$ complex (**2**), which subsequently reacts further under UV illumination and elevated temperatures into the *trans*-$[Cr(CO)_2(dppp)_2]^+$ complex

(i.e., the step-wise transformation of (**1**) into (**2**) and (**3**) is illustrated in Scheme 4.1) [24].

This photoinduced reaction was also shown to be concentration dependent (*i.e.*, the mechanism operates under a bimolecular pathway [18]), and a distribution of all three (**1** – **3**) species was found depending on the concentrations of (1) by EPR [24]. In all cases, the observed contributions of species (**1** – **3**) in the low temperature experiments were typically *ca*. 40% for complex (**1**) and *ca*. 60% for complex (**2**), whereas at room temperature only 100% of complex (**3**) is observed. The spin Hamiltonian parameters of all three complexes (**1** – **3** in Scheme 4.1) are given in Table 4.1.

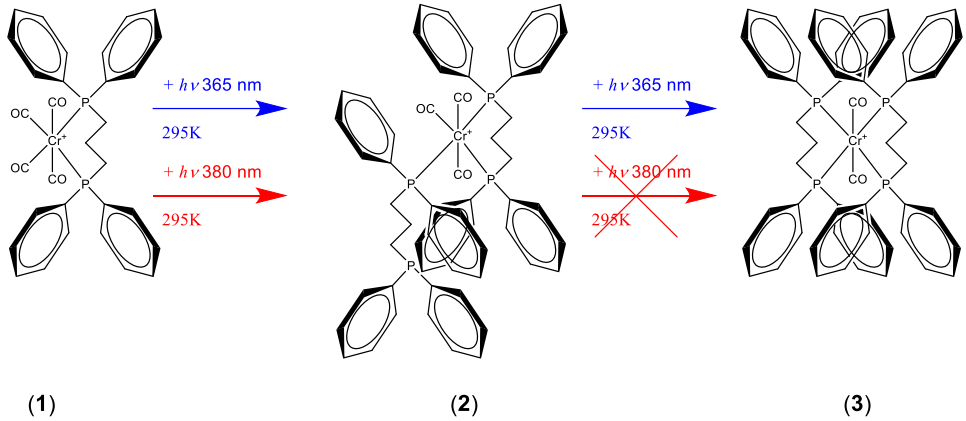

Scheme 4.1: Photochemical transformation of (**1**) $[Cr(CO)_4(dppp)]^+$, into different complexes depending on the wavelength, including (**2**) *mer*-$[Cr(CO)_3(\kappa^1\text{-dppp})\ (\kappa^2\text{-dppp})]^+$ and (**3**) *trans*-$[Cr(CO)_2(dppp)_2]^+$.

4.3.2 Wavelength dependency of the Cr(I)

As stated above, using a broad band UV light source, complex (**3**) was found to be the most dominant species identified in the EPR spectra, with (**2**) only observed at low temperature. The latter complex quickly transforms into (**3**) following prolonged UV exposure [24]. We therefore considered whether any wavelength dependencies existed for this photochemical reaction. As a result, we used different UV sources including a low power LED source (output 350 – 390 nm with a peak emission at 365 nm) and a narrow band Tuneable Light Source (TLS).

When irradiating a 1 mM solution of $[Cr(CO)_4(dppp)]^+$ (**1**) in dichloromethane at 295 K using the LED source (peak emission at 365 nm), the *trans*-$[Cr(CO)_2(dppp)_2]^+$ complex

(**3**) was exclusively observed in the low temperature (140 K) EPR spectrum (Figure 4.3).

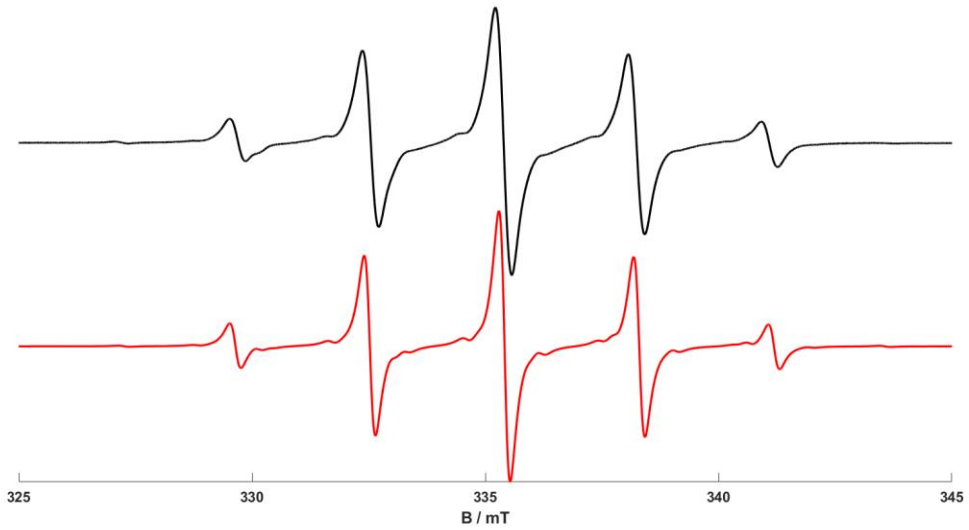

Figure 4.3: X-band CW-EPR spectrum of the *trans*-$[Cr(CO)_2(dppp)_2]^+$ complex (**3**) recorded at 292 K (1 mM of (**1**) in dichloromethane, DCM).

This result, obtained at 365 nm peak emission, is consistent with our previous reported work [18]. However, when irradiating (**1**) using the tuneable light source (TLS) at longer wavelengths (380 ± 2 nm), the resulting EPR spectra observed were notably different (Figure 4.4). This spectrum was recorded at 140 K following room temperature UV irradiation of (**1**) at 380 nm. The spectrum could not be simulated using only a single component (or species). Instead, the experimental spectrum was could only be satisfactorily simulated using a contribution of three species, including the starting $[Cr(CO)_4(dppp)]^+$ complex (11% contribution), the *mer*-$[Cr(CO)_3(\kappa^1\text{-dppp})\ (\kappa^2\text{-dppp})]^+$ complex (86% contribution) and the homoleptic *trans*-$[Cr(CO)_2(dppp)_2]^+$ (3% contribution). Remarkably, the *mer*-$[Cr(CO)_3(\kappa^1\text{-dppp})\ (\kappa^2\text{-dppp})]^+$ complex dominates the EPR spectrum in Figure 4.4 even after UV irradiation at room temperature. Reproducibility of this particular experiment was troublesome, but it was ultimately possible to not only confirm these findings but also improve on them nearly three years after the initial observation (Figure 4.5). By comparison, when using a broad band UV source (at 365 nm), the *trans*-$[Cr(CO)_2(dppp)_2]^+$ complex was exclusively formed at the same temperature. It should also be noted that when irradiating (**1**) using the tuneable light source (TLS) at even longer wavelengths (400 ± 2 nm), no changes

were detected in the EPR spectrum, *i.e.,* only the EPR signal of the starting (**1**) complex was observed. Crucially these results clearly evidence for the first time a wavelength dependency to the observed photochemical transformations of $[Cr(CO)_4(dppp)]^+$ (**1**).

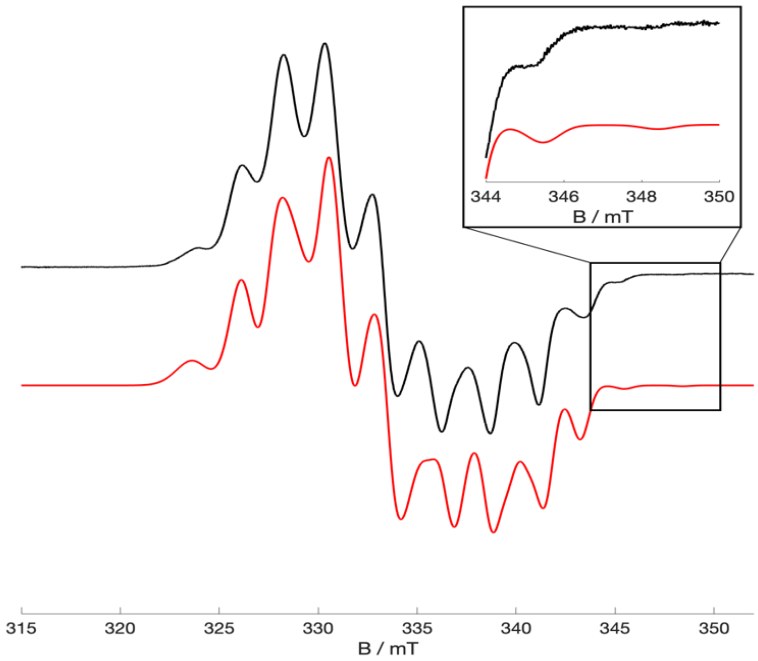

Figure 4.4: X-band CW-EPR spectrum (recorded at 140 K) obtained following room temperature UV irradiation (at 380 nm) of $[Cr(CO)_4(dppp)]^+$ (1 mM in DCM). The simulated spectrum (in red) was obtained using weighted contributions of $[Cr(CO)_4(dppp)]^+$ (11%), *mer*-$[Cr(CO)_3(\kappa^1\text{-dppp})\ (\kappa^2\text{-dppp})]^+$ (86%) and *trans*-$[Cr(CO)_2(dppp)_2]^+$ (3%).

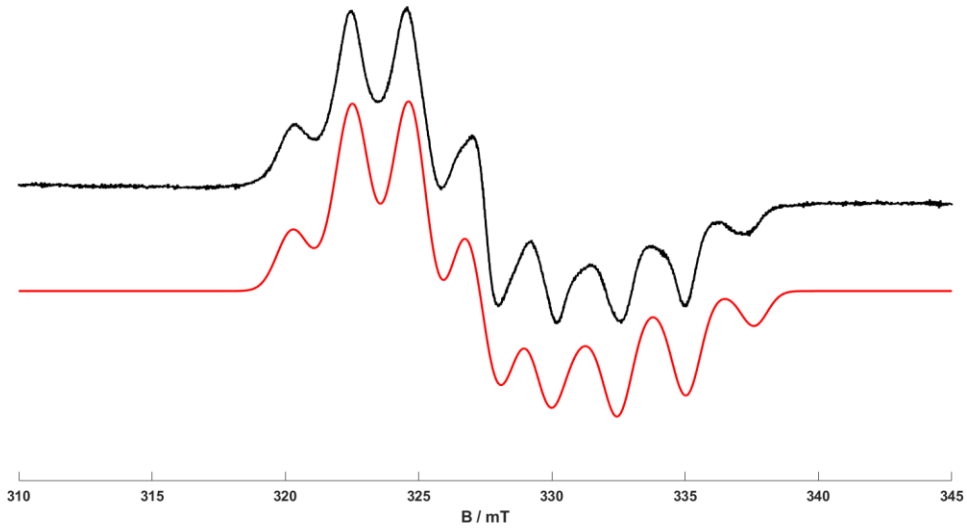

Figure 4.5: X-band CW-EPR spectrum (recorded at 170 K) obtained following room temperature UV irradiation (at 380 nm) of $[Cr(CO)_4(dppp)]^+$ (1 mM in DCM). The simulated spectrum (in red) was obtained using only *mer*-$[Cr(CO)_3(\kappa^1\text{-dppp})\ (\kappa^2\text{-dppp})]^+$.

Table 4.1. Spin Hamiltonian parameters for the three Cr(I) complexes (**1** - **3**; Scheme 4.1).

Compound	g_1	g_2	g_3	α /deg	β /deg	γ /deg	^{31}P A_1 /MHz	^{31}P A_2 /MHz	^{31}P A_3 /MHz	‘α /deg	‘β /deg	‘γ /deg
1	1.991	2.068	2.068	-180	90	60	-65	-77	-77	-120	160	120
							-65	-77	-77	-60	160	60
2	1.984	2.030	2.049	15	60	180	-46	-50	-60	-120	85	-68
							-70	-70	-83	0	90	60
							-46	-50	-60	90	60	-180
3	1.970	2.024	2.024	90	117	180	-80	-82	-82	-20	120	45
							-80	-82	-82	20	120	120
							-80	-82	-82	-20	120	45
							-80	-82	-82	20	120	120

Note: The Euler angles (α, β, γ) for rotation of the *g* frame with respect to the molecular frames, and the Euler angles (‘α, ‘β, ‘γ) for rotation of the A frame with respect to the g frame, are given above (in degrees).

4.3.2 Selective formation of *mer*-[Cr(CO)$_3$(κ^1-dppp) (κ^2-dppp)]$^+$ complex.

It is well known that the Cr-CO and Cr-P bonds are photolabile in a number of Cr(0) complexes, such as [$Cr^0(CO)_4(L)_2$] (where L = bis(diphenylphosphino) ligands) [16]. A competitive photo-dissociation reaction must also be operative in the current Cr(I) complex (**1**), [$Cr(CO)_4(L)]^+$ (where L is also a bis(diphenylphosphino) ligand, dppp) such that an intramolecular exchange of P and CO ligands occurs between neighbouring Cr(I) complexes. This results in the ‘scrambling’ of the ligands that ultimately leads to formation of (**2**) and (**3**) (as shown in Scheme 4.1). In particular, a transient bridged Cr-dppp-Cr dimer must form, resulting in the eventual exchange of one dppp ligand from one Cr(I) centre to a nearby Cr(I) centre, already bearing a η^2-coordinated dppp ligand. This can then lead to the formation of the EPR visible *mer*-complex (**2**). However, it appears from the current findings that at longer UV wavelengths (380 nm versus 365 nm) the final step of the photochemical transformation of (**2**) into (**3**) (i.e., from *mer*-[Cr(CO)$_3$(κ^1-dppp) (κ^2-dppp)]$^+$ to the *trans*-[$Cr(CO)_2(dppp)_2]^+$ complex which requires dissociation of the Cr-CO bond) does not occur. Furthermore, at even longer wavelengths used in this study, 400 nm, no photochemical transformation was detected at all.

We previously showed that the photochemically generated *mer*-[Cr(CO)$_3$(κ^1-dppp) (κ^2-dppp)]$^+$ (**2**) complex was unstable; leaving a solution of (**2**) to stand in the dark at 298 K for several hours resulted only in the observation of a weak residual signal assigned to the starting [$Cr(CO)_4(dppp)]^+$ complex. In other words, the photochemically

generated (**2**) complex does not thermally transform into the kinetically inert (**3**) complex. Indeed, even prolonging the irradiation time at 380 nm indefinitely (for several hours) does not result in the formation of the *trans*-$[Cr(CO)_2(dppp)_2]^+$ (**3**) but only in ever increasing sample degradation. This step, requiring the photo-initiated breakage of a final Cr-CO bond in (**2**) and subsequent ligand rearrangement, can only be accomplished with higher energy UV radiation (365 nm). These results demonstrate for the first time, the potential selective control of the photochemically formed species that can possibly be achieved. In summary, following room temperature irradiation of (**1**) at 365 nm the dominant signal observed in the EPR spectrum is due to (**3**), whereas for similar experimental conditions conducted with 380 nm irradiation, the dominant signal observed in the EPR spectrum is due to (**2**), while at 400 nm only the starting (**1**) complex is observed throughout.

It is important to state that detailed quantitative EPR measurements were not performed here. The spin relaxation characteristics of all three complexes (**1** – **3**) are very different. Therefore whereas (**3**) produces a strong room temperature signal, the signal from (**1**) is virtually absent at the same temperature, so attempting such absolute quantitative measurements is fraught with difficulties. This is why we state the 'dominant' signal is (**2**) or (**3**) rather than give an absolute estimated of spin concentration.

4.3.3 Formation of $[Cr(CO)_2(dppp\text{-}\eta^6\text{-arene})]^+$ complex

Figures 4.4 and 4.5 showed the low temperature CW-EPR spectrum of (**1**) irradiated at room temperature with 380 nm UV radiation. As discussed above this spectrum was dominated by the signal of complex (**2**) with only a small amount of (**1**) and a trace quantity of (**3**). However, when the EPR spectrum of the sample was recorded at 298 K, the resulting signal observed is shown in Figure 4.6. This spectrum is once again dominated by the isotropic component of complex (**2**), noting that the signal of complex (**1**) is not visible at 298 K. However, an additional series of resolved multiplets with narrow line widths to higher field are also visible in the spectrum (Figure 4.6). To understand the origin of this new species, we must first consider the nature of the paramagnetic species that can be formed by chemical activation of complex (**1**).

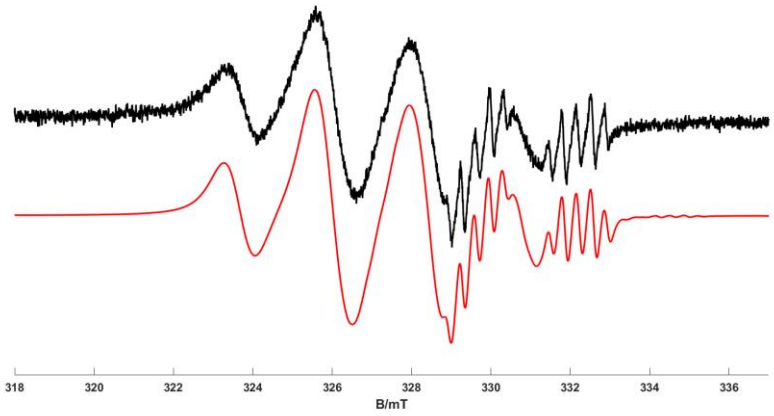

Figure 4.6: X-band CW-EPR spectrum (recorded at 298 K) obtained following room temperature UV irradiation (at 380 nm) of $[Cr(CO)_4(dppp)]^+$ (**1**) (1 mM in DCM). The simulated spectrum (in red) was obtained using weighted contributions of (**2**) *mer*-$[Cr(CO)_3(\kappa^1\text{-dppp})(\kappa^2\text{-dppp})]^+$ (95%) and (**4**) $[Cr(CO)_2(dppp\text{-}\eta^6\text{-arene})]^+$ (5%).

In previous EPR studies from our group [17], we examined the chemical activation of a Cr(I) bis(diphenylphosphino)amine complex, $[Cr(CO)_4(PNP)]$ (where PNP = $Ph_2PN(iPr)PPh_2$), using triethylaluminium (TEA) which can be used as the co-catalyst in ethylene oligomerisation reactions. Treatment of this $[Cr(CO)_4(PNP)]$ complex with high levels of TEA (>10 equivalents) resulted in the complete removal of all CO groups from the complex. A characteristic EPR signal was then identified in the solution and assigned to the fully decarbonylated $[Cr(PNP\text{-bis-}\eta^6\text{-arene})]^+$ complex [17], present in low amounts (in fact most of the Cr(I) EPR signal disappears under these conditions). However, when the Cr(I) sample was treated with lower levels of TEA (from 0.5 up to 10 equivalents), the step-wise intermediates involved in the eventual formation of this bis-arene complex were systematically isolated and identified; these intermediates include a *cis*-$[Cr(CO)_3(PNP)]^+$ complex and a 'piano-stool' type complex $[Cr(CO)_2(PNP\text{-}\eta^6\text{-arene})]^+$. All of these paramagnetic intermediates [17] (Scheme 4.2) were characterised by CW-EPR and the spin Hamiltonian parameters verified using DFT calculations [17]. Crucially, the distribution and type of $[Cr(CO)_X(PNP)]^+$ intermediate formed was found to be very sensitive to the experimental conditions, including the quantity of TEA addition, the temperature of activation and the aging time of the solution. A similar study was also performed using $Cr(CO)_4(dppp)]^+$ (**1**), albeit at >10 equivalents of TEA, and a similar $[Cr(CO)_2(dppp\text{-}\eta^6\text{-arene})]^+$ complex was also identified [16].

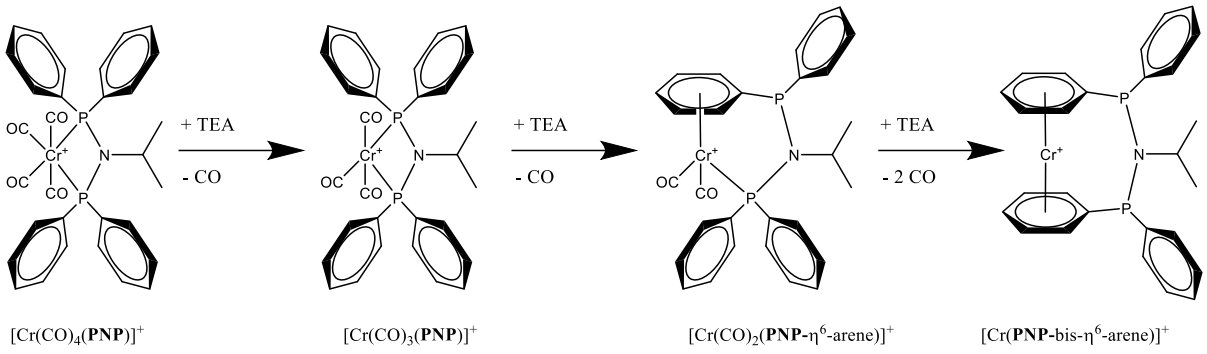

Scheme 4.2: Reaction scheme showing the transformations of $[Cr(CO)_4(PNP)]^+$ following treatment with triethylaluminium (TEA) [17].

The EPR spectra of Cr(I) 'piano-stool' type complexes have been reported in the literature, and they are all expected to produce a rhombic ***g*** tensor [24]. Indeed Cr(I) 'piano-stool' type complexes bearing specifically a diphenylphosphino ligand have been isolated and structurally characterised in the past, so their formation in the TEA activated system is not unexpected following decarbonylation of the corresponding Cr(I) complex [24] and their EPR signal is very characteristic. Therefore, in the current study, we simulated the additional high field multiplet in Figures 4.7 and 4.8 using the known spin Hamiltonian parameters for a 'piano-stool' type complex, $[Cr(CO)_2(dppp\text{-}\eta^6\text{-arene})]^+$ (Table 4.2) and the match between the experimental and simulated profile is excellent.

We know from our previous study on the photochemistry of (**1**) that the formation of (**2**) and (**3**) is concentration dependent [18]. By operating at lower concentrations (for example 0.25 mM or less), the intermolecular exchange pathway for the ligands is supressed, and this may favour the observation of paramagnetic species associated with any unimolecular transformation. As a result, a weaker concentration of complex (**1**) (0.25 mM in DCM) was exposed to 365 nm radiation at low temperatures (140 K) and the sample subsequently warmed to room temperature to record the isotropic signal. The resulting spectrum is shown in Figure 4.7. The multiplet signal originally observed in Figure 4.6 is now clearly visible, owing to the absence of any overlapping signals from (**2**) or (**3**) (which require higher concentrations of (**1**) to observe in the room temperature spectrum). The spectrum in Figure 4.7 was simulated using the spin Hamiltonian parameters listed in Table 4.2.

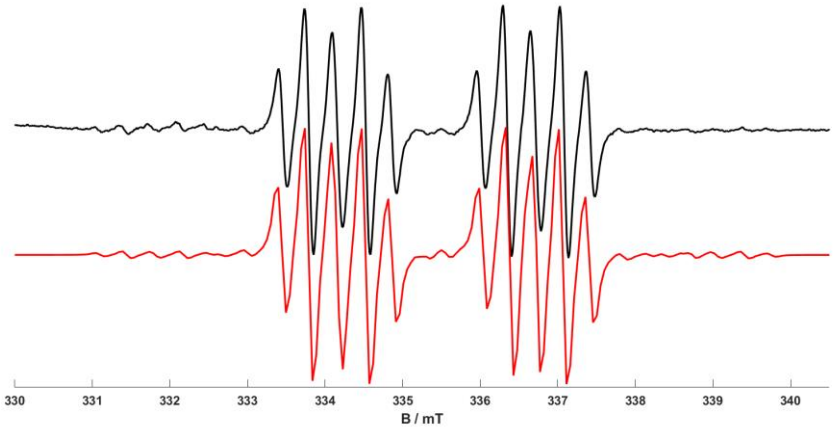

Figure 4.7: X-band CW-EPR spectrum of the of $[Cr(CO)_2(dppp\text{-}\eta^6\text{-arene})]^+$ complex recorded at 295 K after thawing the frozen solution irradiated at 140 K (0.25 mM in DCM). The corresponding simulation is shown in red.

Interestingly, this is the first time that the piano-stool complex (**4**) was observed following a photochemical transformation. Previously this complex was only observed by TEA activation [16, 17] or electrochemically generated [24]. However, there was no evidence in the current work for the formation of the bis-arene sandwich complex shown in Scheme 4.2. Certainly when $[Cr(CO)_4(PNP)]^+$ was exposed to small quantities of TEA at low temperature, the piano-stool complex was first formed, and this slowly transformed into the bis-arene sandwich complex upon warming to room temperature. This similar transformation does not occur in the current photochemical reactions. Unlike the TEA reaction which selectively remove CO ligands only, enabling facile formation of $[Cr(dppp\text{-bis-}\eta^6\text{-arene})]^+$ (Scheme 4.3), UV irradiation results in both Cr-CO and Cr-P photolysis so it is unlikely that the 'piano-stool' complex (**4**) can survive long enough to transform into the $[Cr(dppp\text{-bis-}\eta^6\text{-arene})]^+$ (Scheme 4.3).

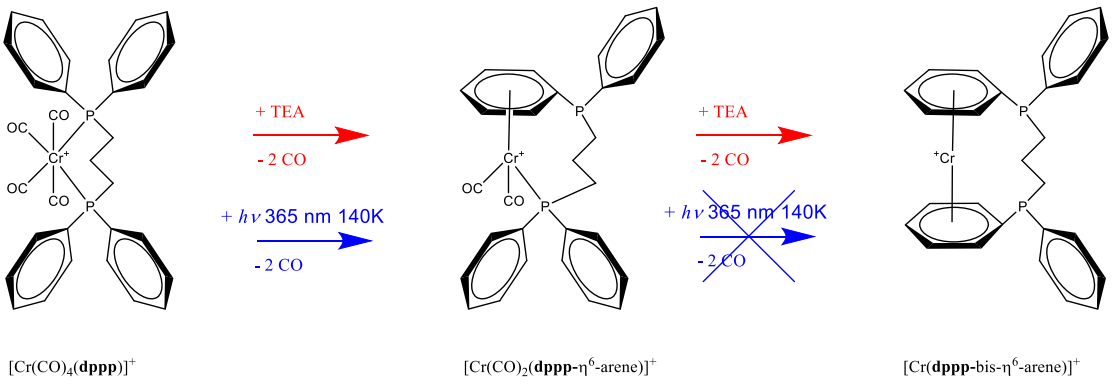

Scheme 4.3: Proposed reaction path for $[Cr(CO)_4(dppp)]^+$ in frozen solution (140K) compared to previous studies with TEA.

The structure of the signal is composed of a doublet originating from the single ^{31}P still within the coordination sphere of the metal centre. This doublet is further divided by the ^{1}H of the aromatic ring coordinating the metal centre, these have 3 distinct super-hyperfine values as can be seen in Table 4.2, one larger super-hyperfine coupling from the ^{1}H in the Para position, two each from the Orto and Meta (which are too small to be resolved in CW-EPR). There are 18 expected lines originating from this system but the overlapping signals reduce the total visible to 6. The contribution of ^{53}Cr (S = 3/2) hyperfine coupling provides the additional features on both sides of the spectrum and in the centre.

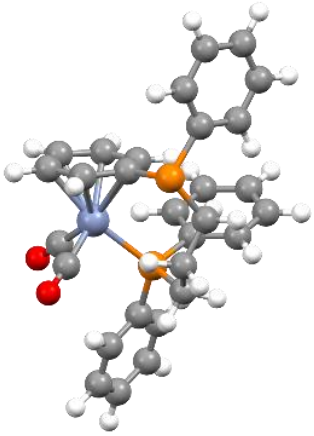

Figure 4.8: DFT geometry optimised structure of $[Cr(CO)_2(dppp\text{-}\eta^6\text{-arene})]^+$.

Table 4.2: Spin Hamiltonian parameters (experimental and DFT) for the $[Cr(CO)_2(dppp\text{-}\eta^6\text{-arene})]^+$ complex (**4**).

$[Cr(CO)_2(dppp\text{-}\eta^6\text{-arene})]^+$	g_{iso}	^{53}Cr a_{iso} /MHz	^{31}P a_{iso} /MHz	^{1}H (para) a_{iso} /MHz	^{1}H (orto) a_{iso} /MHz	^{1}H (orto) a_{iso} /MHz	^{1}H (meta) a_{iso} /MHz	^{1}H (meta) a_{iso} /MHz
Experimental	2.0078	44	-72	20.2	9.5	9.5	<2	<2
DFT	2.0215	27	-107	0.8	3.2	2.5	-0.7	-2.6

Nevertheless, the current results demonstrate that in addition to the dominant photochemical transformations of $[Cr(CO)_2(dppp)]^+$ into *trans*-$[Cr(CO)_2(dppp)_2]^+$ through the intermediary *mer*-$[Cr(CO)_3(\kappa^1\text{-dppp})(\kappa^2\text{-dppp})]^+$ complex, other photochemical side reactions are also possible leading to the formation of a new paramagnetic species identified as a piano-stool $[Cr(CO)_2(dppp\text{-}\eta^6\text{-arene})]^+$. Further

experiments are underway to examine the feasibility of selectively controlling the nature and abundance of the Cr(I) centres in these photochemical reactions.

4.4 Formation of $[Cr(CO)_3(dppp)(1\text{-hexene})]^+$ complex

The above studies described so far have shown that the $[Cr(CO)_4(dppp)]^+$ complex displays a complex photochemistry dependent on multiple factors such as concentration, temperature and wavelength of UV light. Whilst the intermolecular transformed complexes (**2**) and (**3**) are unique to the photochemical reactions, the additional formation of the 'piano-stool' $[Cr(CO)_2(dppp\text{-}\eta^6\text{-arene})]^+$ complex (**4**) shows that, at least under the right conditions, it is possible to reproduce at least some of the species conventionally obtained with TEA through a photochemical pathway. It was therefore necessary to next probe whether, under the conditions examined so far, it is possible to bind an olefin to the Cr(I) complex under UV irradiation conditions. For the purpose of this study, 1-hexene was used as the model substrate. 1-hexene is the shortest chain olefin available in liquid form, can be safely stored and hence is widely used in oligomerisation studies.

The data presented here has been collected using 1-hexene as part of the solvent itself with an estimated ratio of 10^4 equivalents relative to the Cr(I) complex. Interestingly, it is possible to observe that a new species is formed even without any form of activation. Reproducibility without activation is quite poor, with very inconsistent ratios; while it was impossible to work in absolute darkness Figure 4.9 was produced taking as much care as possible to minimize the effect of ambient light by using aluminium wrap and dimming lights to the extent where it was still possible to operate safely in a glovebox. Even under these conditions a small amount of new complex was produced.

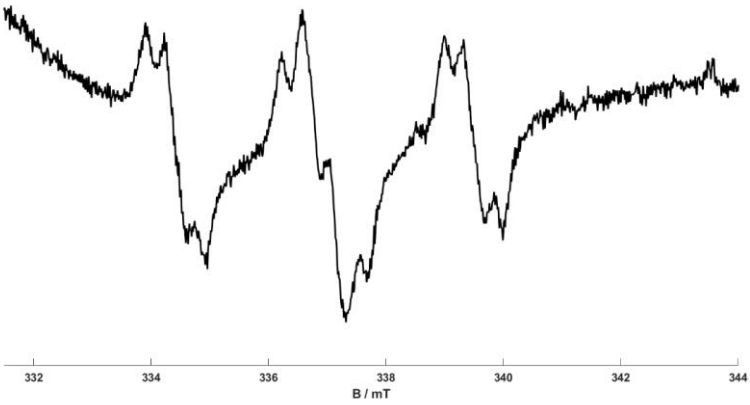

Figure 4.9: X-band CW-EPR spectrum of (**1**) recorded at 298 K containing an excess of 1-hexene (0.33 mM in DCM/1-hexene 1:3 solution).

The room temperature spectrum (Figure 4.9) is composed of a quasi-triplet of smaller multiplets, and this indicates the formation of a new species likely associated with 1-hexene coordination, hereafter referred to as complex (**5**).

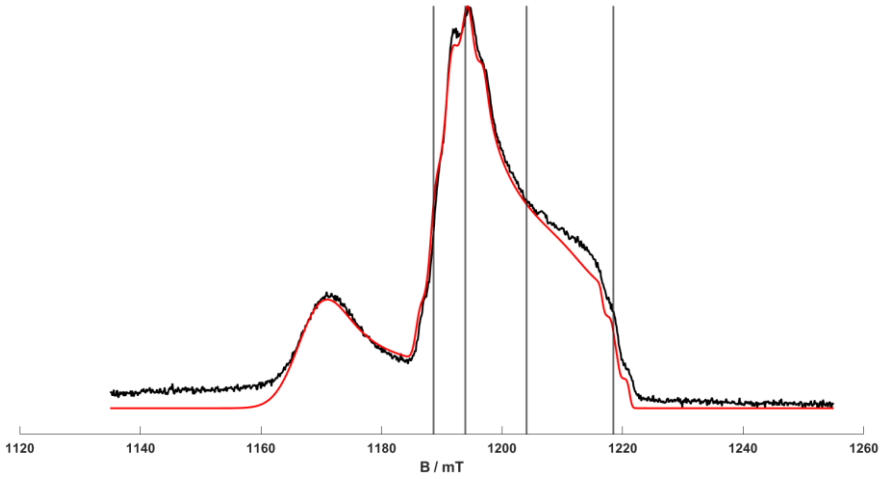

Figure 4.10: Field swept echo detected Q-band spectrum of $[Cr(CO)_3(dppp)(1\text{-hexene})]^+$ complex (70%) and $[Cr(CO)_4(dppp)]^+$ complex (30%) recorded at 30 K. 0.33 mM in DCM/1-hexene 1:3 solution. The corresponding simulation is shown in red. The vertical lines indicate the field positions at which pulse Q-band ENDOR was recorded (1193.9 mT, 1188.6 mT, 1204.1 mT, 1218.5 mT) (Figure 4.11).

As can be seen in the Figure 4.10 there are two components in this spectrum, with the precursor species accounting for 30% in weight in the simulation (peak at 1170 mT). The new species of interest is dominant contribution with 70% weight. To perform pulse Q-band ENDOR several field positions were chosen, and the results can be seen below in Figure 4.11.

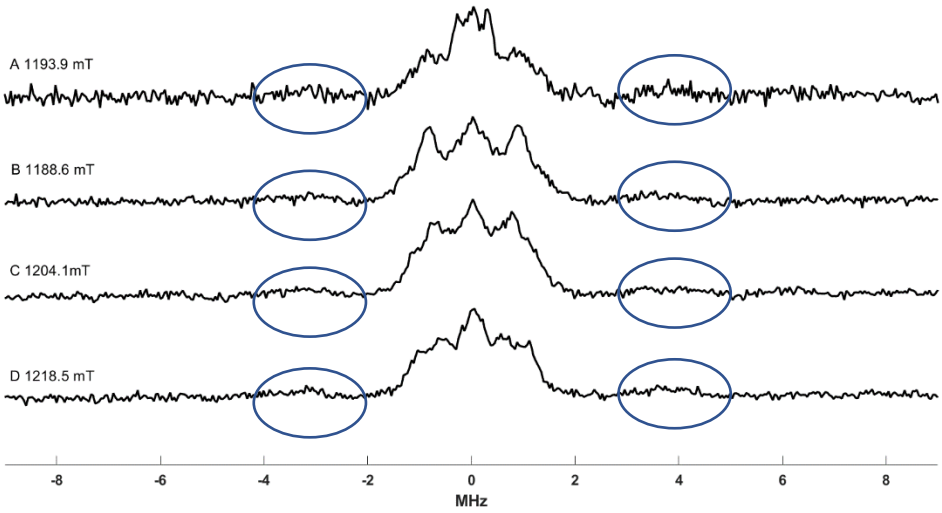

Figure 4.11: Pulse Q-band Mims ENDOR of $[Cr(CO)_3(dppp)(1\text{-hexene})]^+$ complex recorded at 30 K. 0.33 mM in DCM/1-hexene 1:3 solution. Location of field positions (1193.9 mT, 1188.6 mT, 1204.1 mT, 1218.5 mT) can be seen in figure 8. X axis displayed as deviation from ^1H Larmor frequency A) 50.8333; MHz B) 50.6076 MHz; C) 51.2675 MHz; D) 51.8807 MHz.

The central peaks are protons with small couplings to the metal centre, likely these are the contribution of all the protons on the dppp ligand and potentially other minor contributions from 1-hexene (both in the coordination sphere and as a solvent). There are smaller peaks visible but these at 4 MHz from the proton Larmor frequency but these are not strong enough in these spectra to be able to make meaningful conclusions. Due to time constraints, it was impossible to make a second attempt at Turin university to record another pulse Q-band ENDOR spectrum, the project was continued at Antwerp University, where a secondment period had already been planned from January to February 2022, where it was possible to record pulse X-band ENDOR.

This part of the project proved more difficult than expected, in large part due to difficulties in obtaining samples with high concentrations of the complex coordinated with 1-hexene. At this point in the study the experimental procedure to reproducibly obtain high concentration of the target species was still not completely understood and significant differences in the equipment available between the two laboratories made it impossible to accurately follow the same procedures employed at the University of Turin.

While it was ultimately possible to obtain a sample of acceptable quality, this came at the very end of the allocated period and liquid helium allotment. While the spectra in Figure 4.13 represent an improvement over those obtained in Turin, the signal to noise ratio was still too high to deem the result satisfactory other than confirming the presence of protons with couplings to the metal centre too large to be assigned to bulk and distant protons.

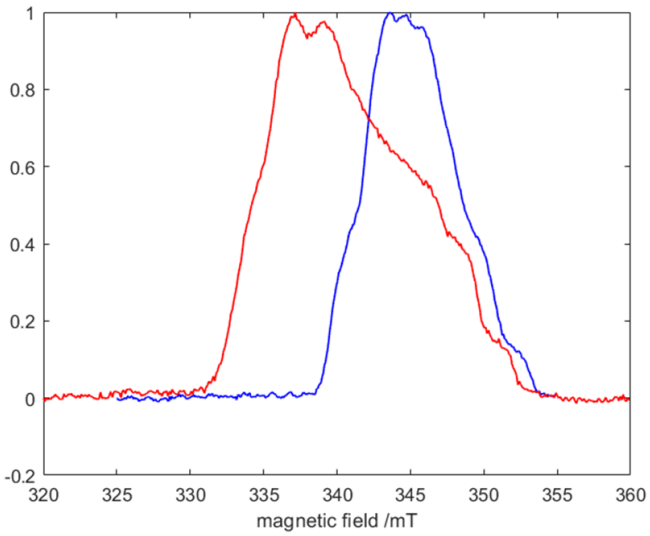

Figure 4.12: Field swept echo detected X-band spectrum of $[Cr(CO)_3(dppp)(1\text{-hexene})]^+$ (blue) compared against the precursor $[Cr(CO)_4(dppp)]^+$ (red). 0.33 mM in DCM/1-hexene 1:3 solution recorded at 10K.

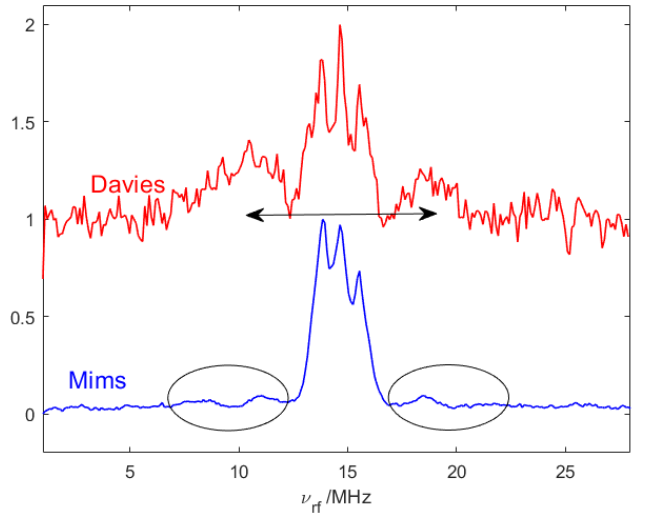

Figure 4.13: Pulse X-band ENDOR (Mims blue; Davies red) EPR spectrum of the of $[Cr(CO)_3(dppp)(1\text{-hexene})]^+$ complex. 0.33 mM in DCM/1-hexene 1:3 solution. 0.33 mM in DCM/1-hexene 1:3 solution recorded at 10K.

A solution of $[Cr(CO)_4(dppp)]^+$ (**1**) in dichloromethane containing an excess of 1-hexene was therefore prepared and exposed briefly to UV irradiation at room temperature. The irradiation time employed was short (*ca*. 2 mins, Figures 4.14 and 4.15) as prolonged exposure of complex (**1**) to UV light of 365 nm wavelength will result in the formation of complex (**3**), even when exceeding the optimal irradiation time by a few minutes (Figure 4.16).

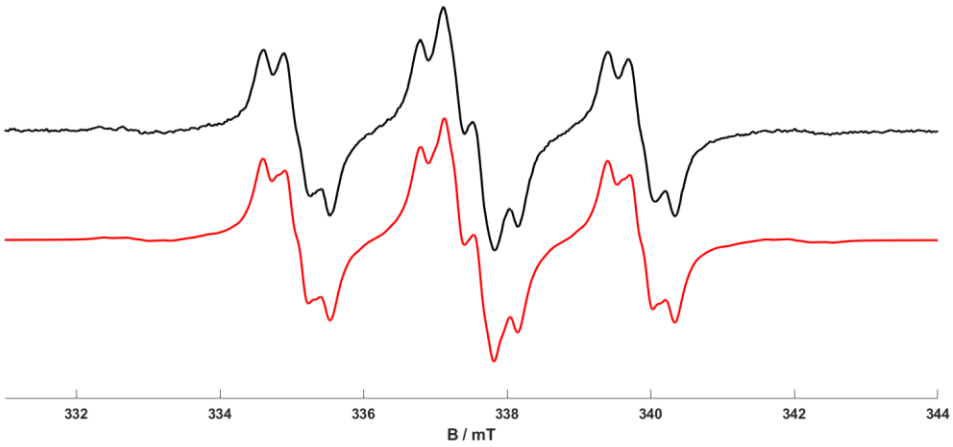

Figure 4.14: X-band CW-EPR spectrum of (**1**) recorded at 298 K following brief (*ca*. 2 mins) room temperature irradiation at 365 nm containing an excess of 1-hexene (0.33 mM in DCM/1-hexene 1:3 solution). The corresponding simulation is shown in red.

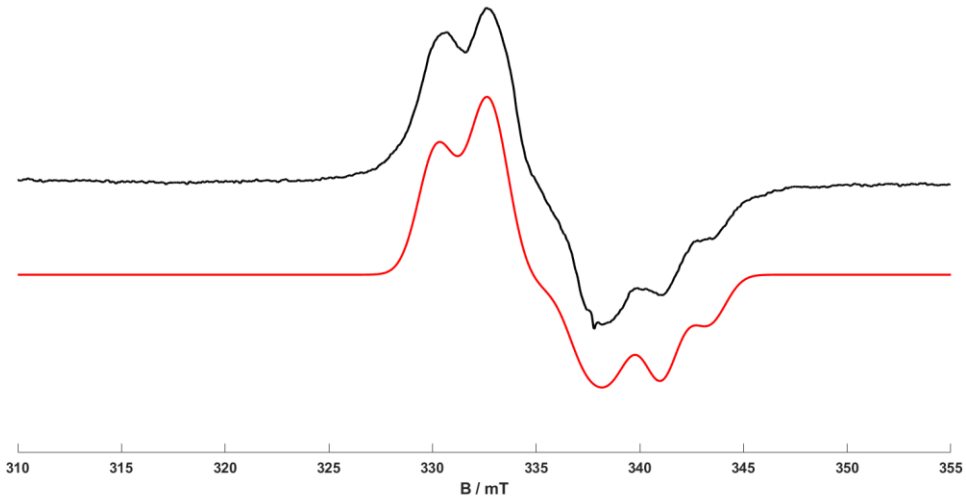

Figure 4.15: X-band CW-EPR spectrum of (**1**) recorded at 140 K following brief (*ca*. 2 mins) room temperature irradiation at 365 nm containing an excess of 1-hexene (0.33 mM in DCM/1-hexene 1:3 solution). The corresponding simulation is shown in red.

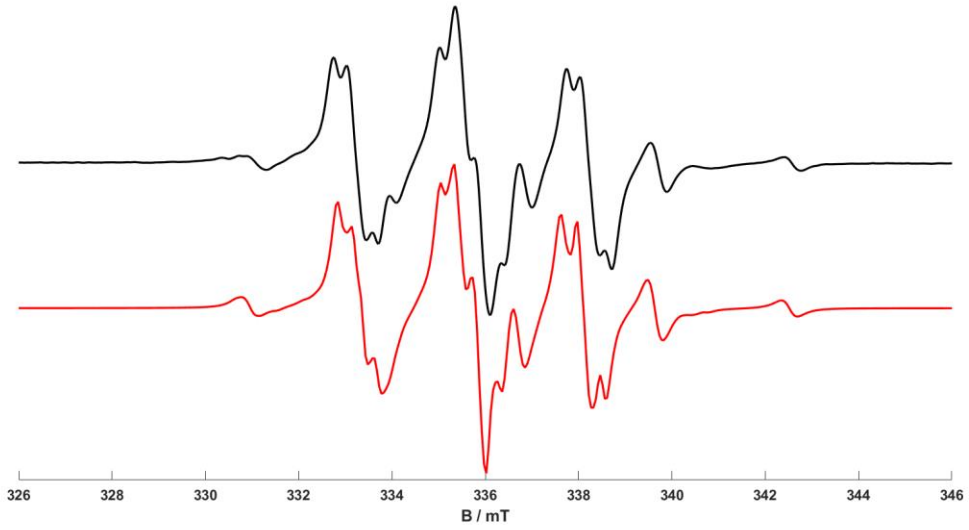

Figure 4.16: X-band CW-EPR spectrum of (**1**) recorded at 295 K following (*ca*. 5 mins) room temperature irradiation at 365 nm containing an excess of 1-hexene (0.33 mM in DCM/1-hexene 1:3 solution). The corresponding simulation is shown in red (simulation weights (**5**) 85%, (**2**) 15%).

Even irradiation at 400 nm will lead to formation of (**5**) although only very slowly over the course of 30 to 40 minutes. These experiments were noteworthy particularly because there was no formation of *trans*-$[Cr(CO)_2(dppp)_2]^+$ or *mer*-$[Cr(CO)_3(\kappa^1\text{-dppp})(\kappa^2\text{-dppp})]^+$ complexes. Ultimately, it was impossible to obtain a pure EPR spectrum of the new complex through this pathway, beyond the indicated time intervals the only thing observed is that the intensity declines slowly over time without any further changes in ratio. This suggests that irradiation at 365 nm with a broad band source is more likely to be under kinetic control while the irradiation at 400 nm, with the narrow band source, is under thermodynamic control.

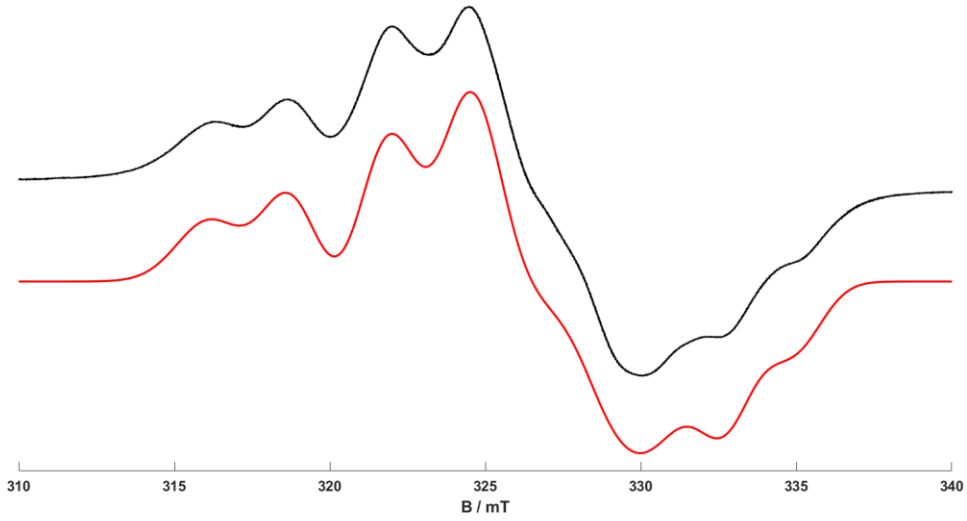

Figure 4.17: X-band CW-EPR spectrum of (**1**) recorded at 140 K following 40 mins room temperature irradiation at 400 nm containing an excess of 1-hexene (0.33 mM in DCM/1-hexene 1:3 solution). The corresponding simulation is shown in red (simulation weights $[Cr(CO)_3(dppp)(1\text{-hexene})]^+$ 67.5%, $[Cr(CO)_4(dppp)]^+$ 37.5%).

From a spectroscopic perspective, the room temperature EPR spectrum (Figure 4.14) is very informative on the identity and structure of the new complex (**5**). Assuming the two interacting ^{31}P nuclei are magnetically equivalent, then strictly a 1:2:1 intensity hyperfine pattern should be observed. This is not observed, and the quasi-triplet pattern suggests the two ^{31}P nuclei are inequivalent. The additional features superimposed on the quasi-triplet likely arise from ^{1}H couplings associated with the coordinated 1-hexene molecule. To test this hypothesis, the experiment was repeated using fully deuterated 1-hexene. In this case, quasi triplet pattern assigned to the two ^{31}P nuclei should be retained, whereas the mutiplets assigned to ^{1}H couplings should disappear. These observations were indeed confirmed through the resulting EPR spectrum shown in 4.18. Indeed, the additional signal resolution afforded by the deuterated 1-hexene enabled us to more accurately observe the small inequivalences in the ^{31}P nuclei. To further confirm these experimental observations, DFT calculations were performed on complex (**1**) with one CO group replaced by 1-hexene. The resulting structure is shown in Figure 4.21, and the agreement between the experimental and DFT calculated spin Hamiltonian parameters is excellent (Table 4.3).

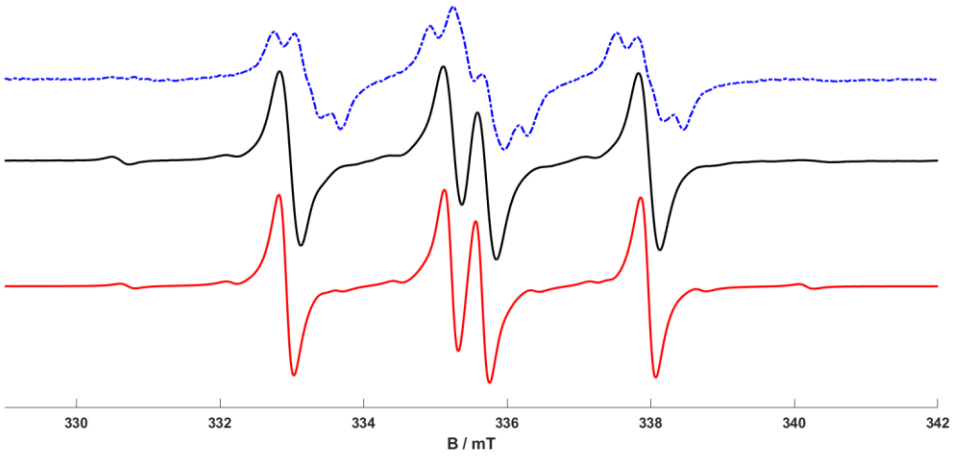

Figure 4.18: X-band CW-EPR spectrum of (**1**) recorded at 298 K following brief (*ca*. 2 mins) room temperature irradiation at 365 nm containing an excess of protic or fully deuterated 1-hexene (0.33 mM in DCM/1-hexene 1:3 solution). Black trace: $[Cr(CO)_3(dppp)(1\text{-hexene-}d_{12})]^+$ Red trace: simulation, Blue trace: $[Cr(CO)_3(dppp)(1\text{-hexene-}H_{12})]^+$ (previously given in Figure 4.14).

The deuterated 1-hexene allows us to both confirm that the attribution of the signals was correct and also better resolve the ^{31}P peaks, which can be resolved as a near double doublet, at room temperature. There is no detectable difference at low temperature as the ^{1}H were not resolved.

Table 4.3: Spin Hamiltonian parameters (experimental and DFT) for the $[Cr(CO)_3(dppp)(1\text{-hexene})]^+$ complex (**5**).

$[Cr(CO)_3(dppp)(1\text{-hexene})]^+$	g_1	g_2	g_3	$^{53}Cr\ a_{iso}$ /MHz	$^{31}P\ A_1$ /MHz	$^{31}P\ A_2$ /MHz	$^{31}P\ A_3$ /MHz	$^{1}H\ a_{iso}$ /MHz
Experimental	1.990	2.059	2.046	-41	-74 -53	-81 -66	-77 -63	9 9 5
DFT	1.9789	2.0115	2.0176	36	-84 -68	-85 -70	-97 -80	9 11 8

One of the interesting observations from the DFT structure is that in order to coordinate effectively to the Cr(I) centre, 1-hexene must orient perpendicular to the plane bearing the diphosphine ligand such that the carbon chain points away from the bulky diphosphine ligand surrounding the Cr(I) complex. This suggests that only some of the 1-hexene isomers will be suitably able to coordinate with the Cr(I) complex. To validate this, the experiments were repeated with a series of 1-hexene isomers including cis-2

hexene, *cis*-3 hexene (which DFT predict should bind), *trans*-2 hexene and *trans*-3 hexene (which DFT predict would not bind) (Scheme 4.4). Indeed, the isotropic EPR results showed that two *cis* isomers did indeed coordinate with Cr(I), though with more difficulty compared to 1-hexene, while the *trans*-isomers did not coordinate. The latter is clearly due to the excessive steric hinderance of the bulkier isomers (Scheme 4.4). The isotropic EPR spectra of $[Cr(CO)_3(dppp)(cis\text{-}2\text{-hexene})]^+$ and $[Cr(CO)_3(dppp)(cis\text{-}3\text{-hexene})]^+$ had to be recorded at slightly lower temperatures (180 K and 230 K, just above the freezing point of the solvent) owing to the poorer stability of these complexes compared to $[Cr(CO)_3(dppp)(1\text{-hexene})]^+$.

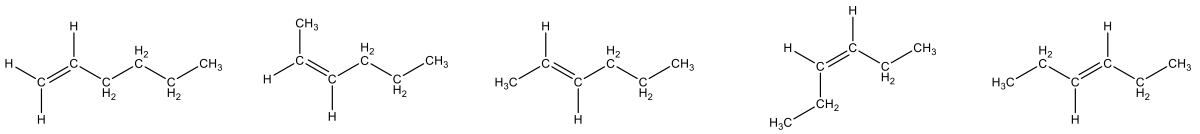

1-hexene | *cis*- 2-hexene | *trans*- 2-hexene | *cis*- 3-hexene | *trans*- 3-hexene

Scheme 4.4: Linear isomers of hexene.

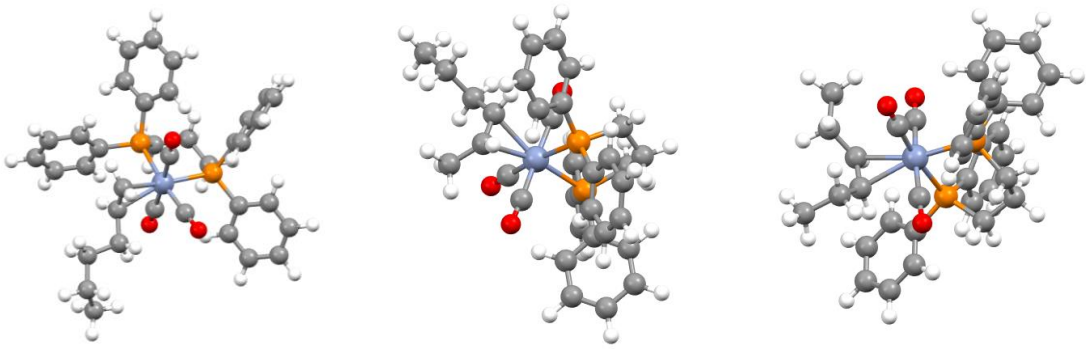

Figure 4.21: From left to right: DFT geometry optimised structure of $[Cr(CO)_3(dppp)(1\text{-hexene})]^+$, $[Cr(CO)_3(dppp)(cis\text{-}2\text{-hexene})]^+$ $[Cr(CO)_3(dppp)(cis\text{-}3\text{-hexene})]^+$.

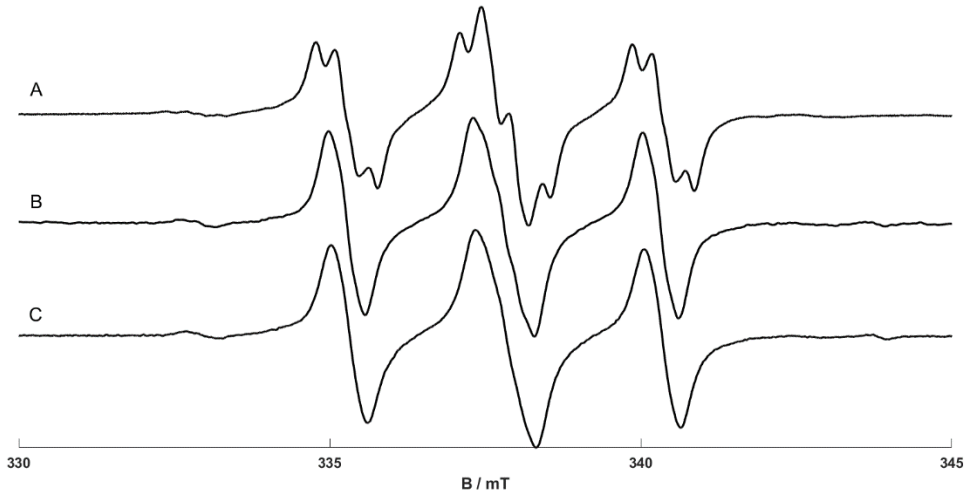

Figure 4.22: X-band CW-EPR spectrum of $[Cr(CO)_4(dppp)]^+$ (**1**) in the presence of different 1-hexene isomers (0.33 mM solution of (1) in DCM/hexene 1:3 solution) following UV irradiation at 365 nm and 298 K: A) $[Cr(CO)_3(dppp)(1\text{-hexene})]^+$ recorded at 292 K; B) $[Cr(CO)_3(dppp)(cis\text{-}2\text{-hexene})]^+$ recorded at 180 K; C) $[Cr(CO)_3(dppp)(cis\text{-}3\text{-hexene})]^+$ recorded at 230 K. Some cooling was introduced for the *cis*-isomers to extend their lifetime long enough to collect the spectra, solution freezes at 150 K.

It can be observed that the complexes bearing *cis*-2-hexene and *cis*-3-hexene display smaller ^1H super-hyperfine couplings than 1-hexene, which are not resolved in CW-EPR. This is likely due to the ligands being unable to coordinate as effectively as 1-hexene, leaving a greater distance between the metal centre and the ^1H involved.

4.5 Reactivity with other ligands

4.5.1 Reactivity with Tetrahydrofuran

Tetrahydrofuran (THF) and dichloromethane (DCM), when mixed together in a 1:3, form a solution which, when frozen, yields a glass of excellent quality. This property has been used to record spectra of $[Cr(CO)_4(dppp)]^+$ and $[Cr(CO)_3(HN(CH_2CH_2PPh_2)_2)]^+$ (see Chapter 5) with excellent results and is the reason why the 1:3 ratio was also used with 1-hexene which also improved glass quality significantly. A high-quality glass makes all orientations of the complex equally probable and results in lowered peak broadness compared to systems where even small degrees of crystallization occur.

In all of the previous experiments, the presence of a solvent with known coordinating properties represented an undesirable complication. However, it was observed that

while the reaction between $[Cr(CO)_4(dppp)]^+$ and THF is spontaneous, the kinetics of it are particularly slow, especially at low temperatures. Indeed, a sample preserved in the glovebox at -20°C for over a year was found largely unreacted despite the overwhelming ratio of THF relative to the $[Cr(CO)_4(dppp)]^+$ complex.

Like 1-hexene however, if coordination sites are opened up by irradiation the reaction will proceed in the time scale of minutes (30 min). As expected, at 400 nm the reaction will only yield $[Cr(CO)_4(THF)]^+$ (Figure 4.23) which is very similar in aspect to Figure 4.18, though with slightly wider peaks.

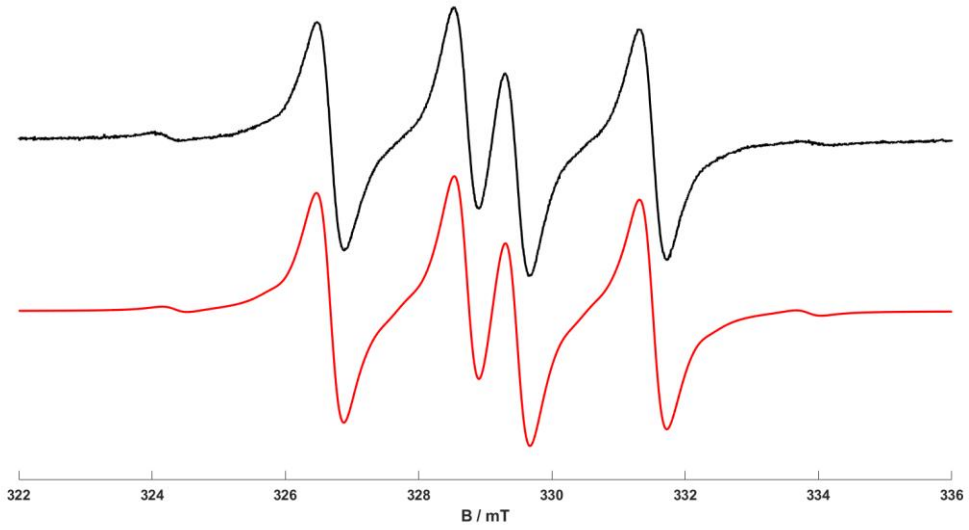

Figure 4.23: X-band CW-EPR spectrum of the of $[Cr(CO)_3(dppp)(THF)]^+$ complex recorded at 292 K. 0.33 mM in DCM/THF 1:3 solution. The corresponding simulation is shown in red.

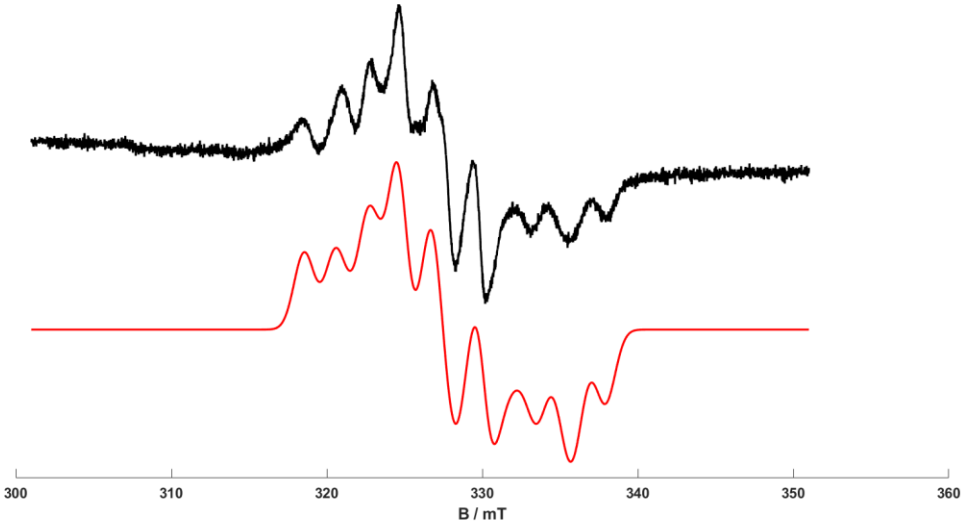

Figure 4.24: X-band CW-EPR spectrum of $[Cr(CO)_3(dppp)(THF)]^+$ complex recorded at 120 K. 0.33 mM in DCM/THF 1:3 solution. The corresponding simulation is shown in red.

Table 4.5: Spin Hamiltonian parameters of $[Cr(CO)_3(dppp)(THF)]^+$

$[Cr(CO)_2(dppp\text{-}THF)]^+$	g_{iso}	$^{53}Cr\ a_{iso}$ /MHz	$^{31}P\ a_{iso}$ /MHz	$^{31}P\ a_{iso}$ /MHz	g_1	g_2	g_3	$^{31}P\ A_1$ /MHz	$^{31}P\ A_2$ /MHz	$^{31}P\ A_3$ /MHz
Experimental	2.008	44	-79	-58	1.984	2.033	2.071	-69	-62	-120*
								-53	-83	-59

Note: the calculated values from the room temperature isotropic spectrum do not perfectly reflect the calculated average of the corresponding anisotropic values from the low temperature spectrum. It is very like that the latter are incorrect, especially the unusually high coupling of 120 MHz. Adding to the simulation a contribution from the precursor did not lead to an improvement in the simulation, if an additional species is present, it was not possible to resolve it or evaluate its individual contribution.

4.5.2 Reactivity with bipyridine and phenanthroline

It was decided to quickly test the reactivity of (**1**) towards other ligands, the choice fell on bipyridine (BIPY) and phenanthroline (PHEN) mostly out of convenience as these ligands were already available and are inexpensive.

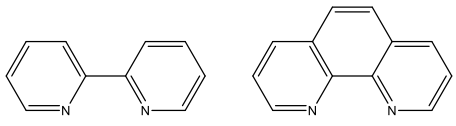

BIPY PHEN

Scheme 4.5: Left: bipyridine (BIPY). **Right:** phenanthroline (PHEN).

The solution was prepared by combining 0.08 mL of 1 mM in DCM solution of (**1**) with 0.02 mL of 4 mM DCM of PHEN or BIPY. In the case of the reaction with BIPY the vast majority of the complex appears to remain in its unreacted form (Figure 4.25) but there is a very narrow unidentified multiplet that cannot be resolved at the scale required to observe the isotropic spectrum of (**1**).

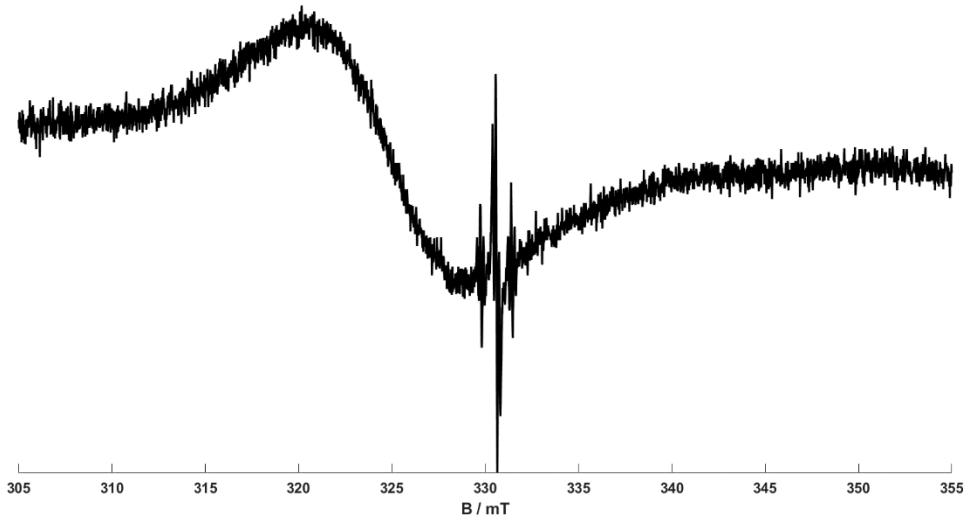

Figure 4.25: X-band CW-EPR spectrum of (**1**) recorded at 292 K. 0.08 mL of 1 mM in DCM solution of (**1**) with 0.02 mL of 4 mM DCM of BIPY.

Zooming into the specific section and performing a new more detailed signal a multiplet composed of a primal 1:2:1 signal each further divided in 1:2:1 structure (Figure 4.26). These couplings are far too small to be associated with ^{31}P nuclei but they can indeed be simulated using 2 magnetically equivalent ^{14}N nuclei to account for the larger couplings and 2 magnetically equivalent ^{1}H nuclei for the smaller couplings. These are likely part of the aromatic rings of BIPY (though if all were visible there should be more signals). There is little evidence to suggest that any coordination is being observed, but the presence of this signal has led to the hypothesis that this is an organic radical being formed by stripping away the unpaired electron away from the complex.

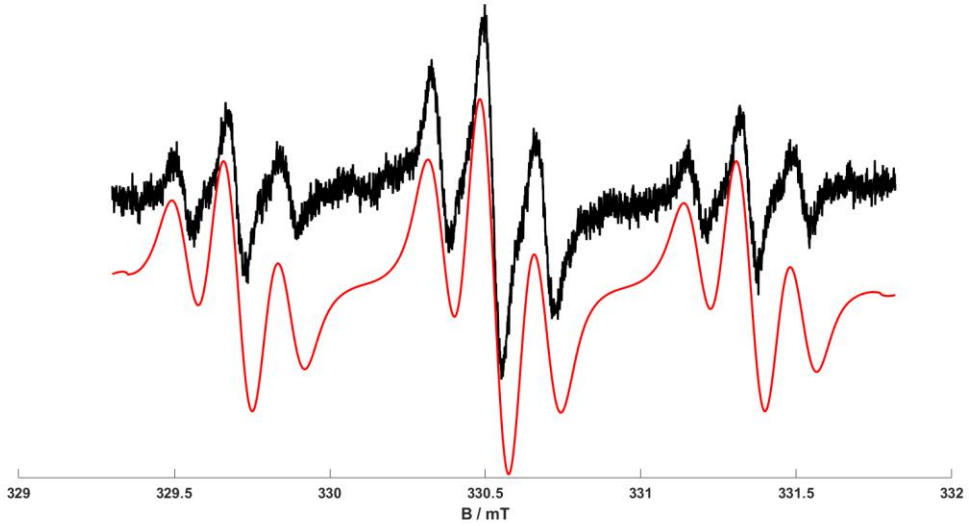

Figure 4.26: X-band CW-EPR spectrum of (**1**) recorded at 292 K. 0.08 mL of 1 mM in DCM solution of (**1**) with 0.02 mL of 4 mM DCM of BIPY (g_{iso} = 2.0135, $a_{iso\ 1}$ = 23.2 MHz, $a_{iso\ 2}$ = 23.2 MHz, $a_{iso\ 3}$ = 4.6 MHz, $a_{iso\ 4}$ = 4.6 MHz.

The reaction with PHEN instead resulted in the complete disappearance of any trace of the starter complex. Given the structural similarity of the two complexes such dramatically different results were not expected. Measuring at the range used for Figure 4.26 it was possible to find a very similar signal to the one measured before, however this signal is so weak to be barely glimpsed out of the baseline noise.

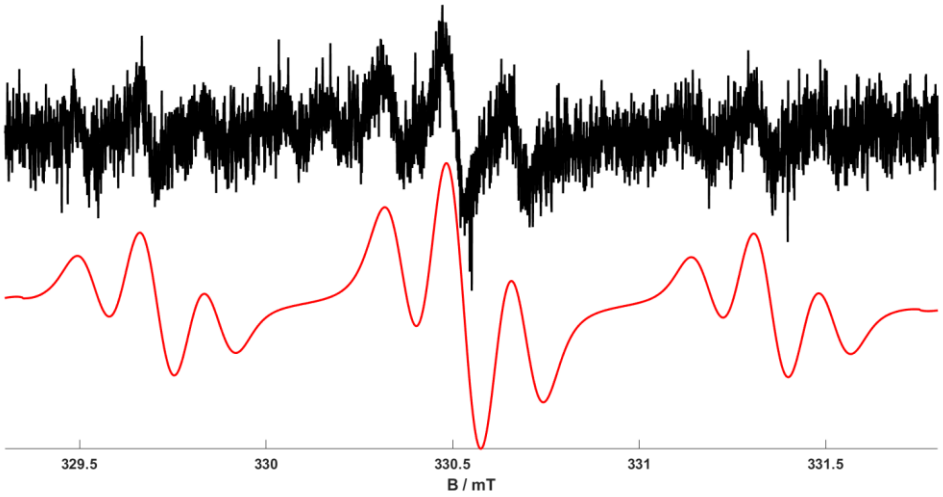

Figure 4.27: X-band CW-EPR spectrum of (**1**) recorded at 292 K. 0.08 mL of 1 mM in DCM solution of (**1**) with 0.02 mL of 4 mM DCM of BIPY.

4.6 Conclusions

The photochemistry of Cr(I) complexes bearing a diphosphine ligand was examined using EPR spectroscopy. The results evidence that this photochemistry can be fine-tuned to produce different complexes as a function of the UV source, wavelength, concentration, and temperature. Of note was the formation the piano stool complex $[Cr(CO)_2(dppp\text{-}\eta^6\text{-arene})]^+$ which is proof that it is possible to photochemically reproduce at least some of the aspects of chemical activation through TEA and MMAO.

The ability of 1-hexene to spontaneously coordinate with $[Cr(CO)_4(dppp)]^+$ was unexpected but likely due to the very large excess of 1-hexene used being able to counter the equilibrium constant favouring coordination with the carbonyl ligand. Finding that at 400 nm we were able to promote the formation of $[Cr(CO)_3(dppp)(1\text{-hexene})]^+$ without displacing the diphosphine ligand was also quite remarkable. As this spontaneous coordination was observed even when employing THF we can conclude that it is not a unique property of olefin ligands, however as BIPY and PHEN have reminded us, Cr(I) one is ultimately a fragile metal centre with the potential for easy oxidation which renders it invisible to EPR investigation.

The experiments performed shed some light into how the different components of the complex are able to interact with selective wavelengths. With our current understanding we can claim that at 400 nm we observe selective scrambling of the carbonyl ligands as indicated by the formation of an equilibrium when we irradiate in the presence of 1-hexene. An equilibrium that is driven by the large amount of 1-hexene used and by the fact that ultimately prolonged irradiation in these conditions will degrade the complex into a state in which it can no longer be observed through EPR. At 380 nm instead we are able to both interact with carbonyl ligands and the phosphine ligand, with the potential to remove it from one metal centre and initiate transfer to a second metal centre. The fact that we were eventually able to obtain an EPR spectrum with only *mer*-$[Cr(CO)_3(\kappa^1\text{-dppp})(\kappa^2\text{-dppp})]^+$ indicates that at this wavelength that can interact with the carbonyl required to create *trans*-$[Cr(CO)_2(dppp)_2]^+$ is at a higher energy than the others. This result lines up with *trans*-$[Cr(CO)_2(dppp)_2]^+$ seemingly being the most stable of all these complexes as when using UV light at 365 nm, and in particular when using the broad band source, we are

scrambling all possible bonds and eventually we form only *trans*-$[Cr(CO)_2(dppp)_2]^+$ even in the presence of 1-hexene.

We hypothesize that our failure to observe coordination of multiple molecules of 1-hexene is due to steric hindrance around the metal centre. From the proposed DFT structures and our studies with the other hexene isomers we can conclude that the size and orientation of the carbon chain plays a significant role in the system and may well be the limiting factor that caps the coordinated molecules to 1. This is proof that while 1-hexene was a very convenient way for testing whether photochemistry was a valid tool for activating these complexes, further progress into the catalytic properties of this system will require the use ethylene gas.

Bibliography

[1] D. S. McGuinness, “Olefin oligomerization via metallacycles: Dimerization, trimerization, tetramerization, and beyond,” *Chemical Reviews,* vol. 111, no. 3, pp. 2321-2341, 2011.

[2] J. T. Dixon, M. J. Green, F. M. Hess and D. H. Morgan, “Advances in selective ethylene trimerisation - A critical overview,” vol. 689, no. 23, pp. 3641-3668, 2004.

[3] A. J. Rucklidge, D. S. Mcguinness, R. P. Tooze, A. M. Z. Slawin, J. D. A. Pelletier, M. J. Hanton and P. B. Webb, “Ethylene Tetramerization with Cationic Chromium(I) Complexes,” *Organometallics,* vol. 26, no. 10, pp. 2782-2787, 2007.

[4] A. Brückner, J. K. Jabor, A. E. McConnell and P. B. Webb, “Monitoring structure and valence state of chromium sites during catalyst formation and ethylene oligomerization by in situ EPR spectroscopy,” *Organometallics,* vol. 15, no. 3849-3856, p. 27, 2008.

[5] I. Y. Skobelev, V. N. Panchenko, O. Y. Lyakin, K. P. Bryliakov, V. A. Zakharov and E. P. Talsi, “In Situ EPR Monitoring of Chromium Species Formed during

Cr−Pyrrolyl Ethylene Trimerization Catalyst Formation," *Organometallics,* vol. 29, p. 2943–2950, 2010.

[6] J. E. Radcliffe, A. S. Batsanov, D. M. Smith, J. A. Scott, P. W. Dyer and M. J. Hanton, "Phosphanyl Methanimine (PCN) Ligands for the Selective Trimerization/Tetramerization of Ethylene with Chromium," *ACS Catalysis,* vol. 5, no. 12, pp. 7095-7098, 2015.

[7] Q. Lo, D. Pye, S. Gesslbauer, Y. Sim, F. García, A. J. White and G. J. Britovsek, "Single- and double-bridged PNP ligands in chromium-catalysed ethylene oligomerisation," *Catalysis Science & Technology,* vol. 12, no. 14, pp. 4544-4551, 2022.

[8] D. S. McGuinness, P. Wasserscheid, W. Keim, D. Morgan, J. T. Dixon, A. Bollmann, H. Maumela, F. Hess and U. Englert, "First Cr(III)-SNS Complexes and Their Use as Highly Efficient Catalysts for the Trimerization of Ethylene to 1-Hexene," *Journal of American Chemical Society,* vol. 125, no. 18, p. 5272–5273, 2003.

[9] D. S. McGuinness, P. Wasserscheid, W. Keim, C. Hu, U. Englert, J. T. Dixon and C. Grove, "Novel Cr-PNP complexes as catalysts for the trimerisation of ethylene," *Chemical Communications,* vol. 3, no. 3, pp. 334-335, 2003.

[10] R. Emrich, O. Heinemann, P. W. Jolly, C. Krüger and G. P. J. Verhovnik, "The Role of Metallacycles in the Chromium-Catalyzed Trimerization of Ethylene," *Organometallics,* vol. 16, no. 8, pp. 1511-1515, 1997.

[11] T. Agapie, S. J. Schofr, J. A. Labinger and J. E. Bercaw, "Mechanistic Studies of the Ethylene Trimerization Reaction with Chromium-Diphosphine Catalysts: Experimental Evidence for a Mechanism Involving Metallacyclic Intermediates," *Journal of the American Chemical Society,* vol. 126, no. 5, pp. 1304-1305, 2004.

[12] B. Venderbosch, J. P. H. Oudsen, D. J. Martin, B. de Bruin, T. J. Korstanje and M. Tromp, "Investigating the Active Species in a [(R-SN(H)S-R)CrCl3] Ethene Trimerization System: Mononuclear or Dinuclear?," *ChemCatChem,* pp. 881-892, 2020.

[13] B. Venderbosch, J. P. H. Oudsen, L. A. Wolzak, D. J. Martin, T. J. Korstanje and M. Tromp, “Spectroscopic Investigation of the Activation of a Chromium-Pyrrolyl Ethene Trimerization Catalyst,” *ACS Catalysis,* vol. 9, no. 2, pp. 1197-1210, 2019.

[14] R. Grauke, R. Schepper, J. Rabeah, R. Schoch, U. Bentrup, M. Bauer and A. Brückner, “Impact of Al Activators on Structure and Catalytic Performance of Cr Catalysts in Homogeneous Ethylene Oligomerization – A Multitechnique in situ/operando Study,” *ChemCatChem,* vol. 12, no. 4, pp. 1025-1035, 2020.

[15] L. E. McDyre, T. Hamilton, D. M. Murphy, K. J. Cavell, W. F. Gabrielli, M. J. Hanton and D. M. Smith, “A cw EPR and ENDOR investigation on a series of Cr(i) carbonyl complexes with relevance to alkene oligomerization catalysis: [Cr(CO)4L] + (L = Ph2PN(R)PPh2, Ph2P(R)PPh 2),” *Dalton Transactions,* vol. 39, no. 33, pp. 7792-7799, 2010.

[16] L. E. McDyre, E. Carter, K. J. Cavell, D. M. Murphy, J. A. Platts, K. W. B. D. Sampford, W. F. Gabrielli and M. J. Hanton, “Intramolecular formation of a CrI(bis-arene) species via TEA activation of [Cr(CO)4(Ph2P(C3H 6)PPh2)]+: An EPR and DFT investigation,” *Organometallics,* vol. 30, no. 17, pp. 4505-4508, 2011.

[17] E. Carter, K. J. Cavell, W. F. Gabrielli, M. J. Hanton, A. J. Hallett, L. E. McDyre, J. A. Platts, D. M. Smith and D. M. Murphy, “Formation of [Cr(CO)x(Ph2PN(i Pr)PPh 2)]+ structural isomers by reaction of triethylaluminum with a chromium N,N -Bis(diarylphosphino)amine complex [Cr(CO) 4(Ph2PN(i Pr)PPh2)]+: An EPR and DFT investigation,” *Organometallics,* vol. 32, no. 6, pp. 1924-1931, 2013.

[18] S. L. J. Luckham, A. Folli, J. A. Platts, E. Richards and D. M. Murphy, “Unravelling the Photochemical Transformations of Chromium(I) 1,3 Bis(diphenylphosphino), [Cr(CO)4(dppp)]+ , by EPR Spectroscopy,” *Organometallics,* vol. 38, no. 12, pp. 2523-2529, 2019.

[19] D. Mingos and P. Michael, “The Electronic Factors Governing the Relative Stabilities of Geometric Isomers of Octahedral Complexes with π-acceptor and π-donor Ligands,” *Journal of Organometallic Chemistry,* vol. 179, no. 2, 1979.

[20] R. G. Compton, R. Barghout, J. C. Eklund, A. C. Fisher, S. G. Davies, M. R. Metzler, A. M. Bond, R. Coltonc and J. N. Walterc, “Photoelectrochemistry of Some Organochromium Carbonyl Compounds,” *1993,* pp. 3641-3646, 1993.

[21] T. Szymańska-Buzar, “Photochemical reactions of Group 6 metal carbonyls with alkenes,” *Coordination Chemistry Reviews,* vol. 250, no. 9-10, pp. 976-990, 2006.

[22] M. Gutmann, J. M. Janello, M. S. Dickebohm, M. Grossekathöfer and J. Lindener-Roenneke, “Ultrafast dynamics of transition metal carbonyls: Photodissociation of Cr(CO)6 and Cr(CO)6·(CH3OH)n heteroclusters at 280 nm,” *Journal of Physical Chemistry A,* vol. 102, no. 23, pp. 4138-4147, 1998.

[23] M. Brookhart, W. Chandler, R. J. Kessler, Y. Liu, N. J. Pienta, C. C. Santin, C. Hall, R. N. Perutz and J. A. Timney, “Matrix Isolation and Transient Absorption Studies of (Bis(bis(pentafluoroethyl)phosphino)ethane)tetracarbonylchromium: Intermolecular Alkane Complexes and Intramolecular F-Coordination,” *Journal of the American Chemical Society,* vol. 114, no. 10, pp. 3802-3815, 1992.

[24] A. L. Rieger and P. H. Rieger, “EPR Study of Photochemical Reactions of fac- and mer-[Cr(CO) 3 (η 1-L 2)(η 2-L 2)] + (L 2) Bidentate Phosphine, Arsine, or Phosphonite Ligand),” *Organometallics,* vol. 21, no. 26, pp. 5868-5873, 2002.

[25] S. Stoll and A. Schweiger, “EasySpin, a comprehensive software package for spectral simulation and analysis in EPR,” *Journal of Magnetic Resonance,* vol. 178, no. 1, pp. 42-55, 2006.

[26] V. Barone, In Recent Advances in Density Functional Methods, Part 1 (ed. D. P. Chong), World Scientific, 1995.

Chapter 5

Synthesis and EPR characterisation of a novel chromium pincer complex, $([Cr(CO)_3(HN-(CH_2CH_2-PPh_2)_2)]^+$ and its chemical and photochemical reactivity with1-hexene

5.1 Introduction

The complex $([Cr(CO)_4(Ph_2P(C_3H_6)PPh_2)]^+$ (**1**)(1,3 bis-(diphenylphosphino)propane, $Ph_2P(C_3H_6)PPh_2$ = dppp) and its properties have allowed us to explore in detail the reactivity of this family of Cr(I) complexes in regard to irradiation and reactivity towards 1-hexene. These types of ligands are called collectively diphosphinoamines or diphosphazanes as discussed earlier in Chapter 1. However, the formation of the homoleptic $[Cr(CO)_2(dppp)_2]^+$ complex, while interesting from a reactivity point of view, is ultimately an undesirable outcome for this complex with the potential for any potential catalytic activity being considerably reduced. As we have demonstrated in Chapter 4, it is possible to fine tune the wavelength of the applied radiation to ensure that some potentially undesirable species are not formed during the reaction, and instead this usually comes with the trade-off of either rendering the reaction slower or reducing the total amount of desired product visible in the EPR spectrum. By moving our investigation to a pincer type ligand, it may be possible to preserve the coordination environment surrounding the metal centre even while subjugating it to chemical and photochemical activation. It is also possible that a pincer ligand, due to its innately higher steric hinderance, would not be able to participate in intermolecular reactions to form complexes analogous to $[Cr(CO)_2(dppp)_2]^+$. Such class of PNP ligands with carbon chains being optional spacers between the two phosphine atoms and the nitrogen have been the subject of much investigation over the years.

An excellent and comprehensive review on metal complexes with diphosphinoamines ligands was presented by Balakrishna *et al.*, [1] which illustrates the synthesis and coordination of these ligands with many different metal centres. More recent works by

Smith [2], von Koten *et al*., [3] and Stradiotto *et al*., [4] have reviewed the topic of hybrid P, N ligands and their complexes more broadly.

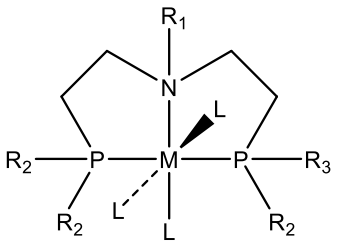

R1 = H, Me, Et, i-Pr, ...

R2 = Ar, Cy, OMe, OBut, ...

Scheme 5.1: Schematic illustration of a metal complex bearing a ligand with a P-C_2H_4-N-C_2H_4 backbone [3].

Generally speaking, these ligands are synthesized by combining a chlorinated phosphine with a suitable ammine in the correct proportions but by necessity of their varied structures each synthesis is somewhat unique. For the simplest systems the mechanism is as reported in Scheme 5.2 below:

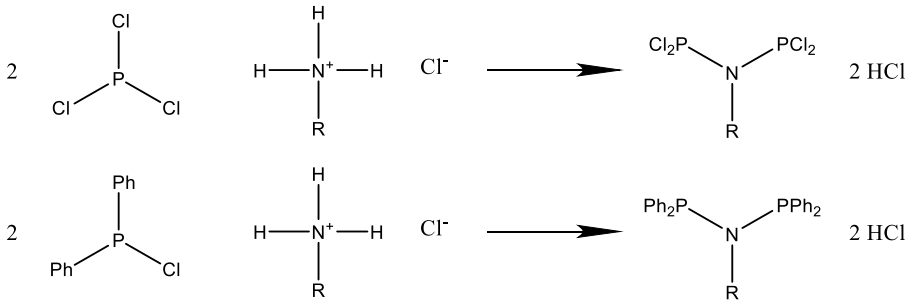

Scheme 5.2: Synthesis of $NR(PPh_2)_2$·HCl [1].

With regards to their coordinating capabilities, these ligands are viable in a wide range of the transition metal series, and typically are used in an octahedral coordination but they are equally capable of coordinating through either η^1, η^2 or η^3 hapticity depending on their geometry and bite angle. For example, the system reported in Scheme 5.2 typically coordinates in η^2 configuration through the P sites. Conversely, those with metylenic chains separating the P and N sites can coordinate with all 3 sites at once (η^3). Besides the changes in hapticity, their activity is highly customizable through several modifications such as the metal centre, the secondary functional groups linked to the nitrogen or phosphorous atoms and the length of the connector chains between the three coordination sites.

The metals that can be accommodated and coordinated by the ligands is wide ranging and diverse. For example, group V metals such as vanadium and niobium have been found to be capable of interacting with ligands such as $(CH_3)N(PF_2)_2$ from their sandwich complexes with cyclopentadiene (Cp) of structure MCp_2. It is also possible to react diphosphinoamines with piano-stool type complexes bearing a structure of $CpM(CO)_4$. This will form a piano stool complex such as $CpV((CH_3)N(PF_2)_2)_2$ [5]. These reactions are photochemically catalysed by UV radiation, not unlike the reactions examined in Chapter 4.

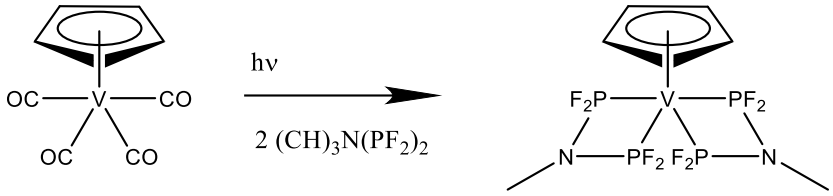

Scheme 5.3: Synthesis of $CpV((CH_3)N(PF_2)_2)_2$ [1].

On the other hand, group VI metals such as chromium, molybdenum and tungsten appear to have some of the greatest variety of complexes formed with diphosphinoamines through a thermal reaction from their respective carbonyl complexes. These complexes can form even as bimetallic complexes with a variety of configurations such as having the diphosphinoamines ligands acting as bridging ligands, having a secondary ligand acting as the bridging element or having the metal connect through a direct M-M bond [6].

With regards to the current work, many of the Cr(I) complexes of relevance to the oligomerisation work were already presented in Chapter 1. It is worth mentioning again that the work reported by the Wass group on Cr(III) based catalysts is directly relevant to this PhD Thesis as the ligand was prepared in collaboration with their group [7].

The group VII metals such as manganese have received a lot of attention, particularly for PNP ligands separated by alkylic chains such as the one used in this Chapter, since they are employed with manganese for the catalysis of formic acid from CO_2 hydrogenation as a form of hydrogen storage and synthetic fuel production [8]. The list of reactions that have been examined with these types of Mn catalysts include acceptor-less dehydrogenation, hydrogenation, dehydrogenative coupling, hydrogen

borrowing, hydrogen transfer, H–X additions, C–C coupling, alkene polymerization and N_2 fixation [9].

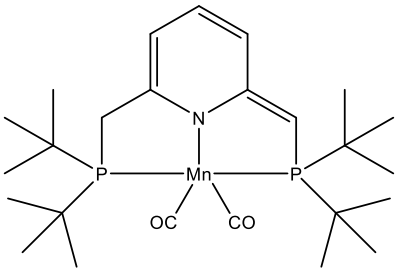

Scheme 5.4: Schematic illustration of the Mn based complex for dehydrogenation catalysis of aldehydes from alcohols [10].

The use of Group VIII metals is also prevalent in these studies including iron and ruthenium. Ruthenium and iron have also displayed hydrogenation and dehydrogenation catalytic activity similar to the previously mentioned Mn [11, 12, 13]. Ruthenium in particular spawned a whole new class of hydrogenation catalysts, typically for ketones, referred to as Noyori type catalysts [14] which are enantioselective and thus of invaluable importance in the synthesis of drugs in which the selective synthesis of the correct isomer is crucial. This is one of several fields in which the economical drive away from expensive second and third transitions metals has been particularly active. There is an ongoing effort to replicate the successes of metals such as ruthenium complexes with first row transition metals and the adaptable nature of these pincer ligands has proven a great asset in this line of research [15].

The group IX metals, including cobalt, rhodium and iridium are also popular metal centre for PNP ligands such as the one earlier presented for manganese and have a lot of overlap with the types of reaction that are reported to be possible, to the point where they are often found together in scientific literature [9].

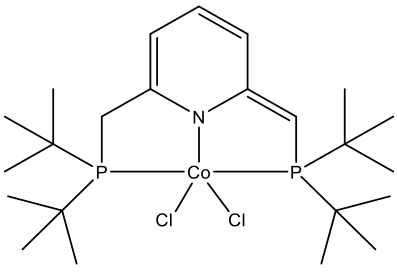

Scheme 5.5: Example of a Co-based catalyst for the synthesis of pyrroles [10].

The group IX metals such as nickel can also catalyse the dehydrogenation of alcohols in conjunction with amines to form imines [16] and in alkenylation reactions [17]. There is even a reported instance of a complex in which the activated site isn't on the metal itself but on the para position of the pyridine ring which includes the nitrogen atom [18].

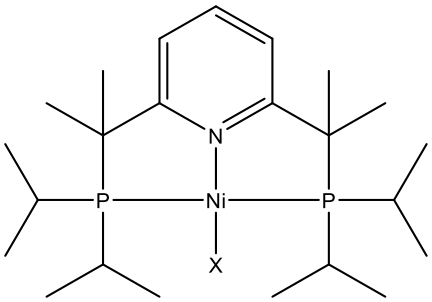

Scheme 5.6: Example of a Ni-based complex with an activate *para* position, opposite to the N atom on the pyridine ring [18] for ligand deraromatization.

Palladium(II) based catalysts with PNP ligands have also been reported for polyketone synthesis [19] while a recent example of a platinum PNP complex is [20], which is a catalyst for tandem P-C cleavage / P-N formation reaction.

To the best of our knowledge there is no precedent for the synthesis of a Cr(I) based system similar to the ones already investigated using the pincer ligands, let alone the spectroscopic characterisation of the resulting paramagnetic complex by EPR. The synthesis procedure was carried out using a combination of the synthesis procedure for the Cr(0) version of the complex in conjunction with the final oxidation step also used for the synthesis of $[Cr(CO)_4dppp]^+$.

5.2 Experimental

5.2.1 Synthesis of the $[Cr(CO)_3(HN(CH_2CH_2PPh_2)_2)]^+$ $[Al(OC(CF)_3)_4]^-$ complex

For long term storage, the $Ph_2P(C_2H_4)NH(C_2H_4)Ph_2$ ligand is preserved as $HCl{\cdot}HN(CH_2CH_2PPh_2)_2$ which is more stable. Phosphines are not particularly stable, though every specific phosphine is different, and instances of these compounds being pyrophoric are not uncommon. All operations were therefore necessarily carried out in N_2 atmosphere, operating within a Schlenk line (see Chapter 3 for details).

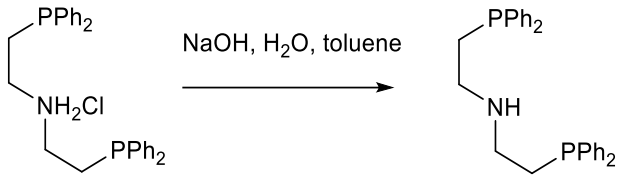

Scheme 5.7: Removal of HCl from the $HCl{\cdot}HN(CH_2CH_2PPh_2)_2$ compound.

$HCl{\cdot}HN(CH_2CH_2PPh_2)_2$ (477.95 g/mol; 0,201 g; 0.421 mmol) was dissolved in 5 mL of toluene and loaded into a Schlenk flask. Then 2 mL of a degassed, 15 wt.% aqueous solution of NaOH (40 g/mol; 0,3 g; 7,5 mmol) was added and stirred for 90 minutes. As much of the diphosphinoamine remained in solid form an additional 2 mL of NaOH solution was added and left to stir overnight. Once all the solid $HCl{\cdot}HN(CH_2CH_2PPh_2)_2$ was dissolved, the organic toluene layer was washed with degassed water (2 x 5 mL). The aqueous layer was extracted with toluene (2 x 10 mL). The organic layer from both sources was then dried with Na_2SO_4. The slurry was then filtered and washed with toluene (2 x 5 mL). The reaction was, ultimately, a lot slower than what had been expected from the literature. A yellowish oil was recovered, dissolved in 10 mL of toluene and analysed through ^{31}P NMR spectroscopy. A single peak at -21 ppm was detected which matched the expected value from literature. The experimental procedure described above was adapted from this literature source [21].

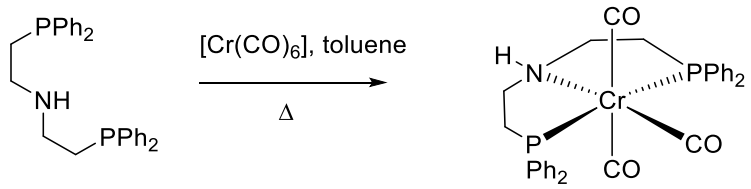

Scheme 5.8: Synthesis of $[Cr(CO)_3(HN(CH_2CH_2PPh_2)_2)]$.

Once the ligand had been prepared, it was possible to synthesize the Cr(0) complex using the following literature reference which also employed for the dppp complex [22]. An alternative procedure which involved use of C_4H_9Li to facilitate coordination was considered, if necessary. As the synthesis was successful this alternative method was not necessary [23].

The solution of 10 mL of the $HN(CH_2CH_2PPh_2)_2$ (441.49 g/mol; 0,186 g; 0.421 mmol) in toluene was used in the same Schlenk flask employed in the previous stage. To this, $Cr(CO)_6$ (220.06 g/mol; 0,093 g; 0.421 mmol) was added as a powder, which sublimed very quickly on the flask walls. After being left in reflux conditions for 24 hours the solution was found to have turned orange. Examination the ^{31}P NMR spectra revealed a new signal at -60.5 ppm that was likely the desired complex. However, at this stage, a significant amount of ligand remained free (signal at -20.4 ppm). Additional signals at -42.6 ppm and -27.6 ppm were hypothesized to be potential intermediate stages (ligation through only one or two of the sites).

The solution was refluxed for an additional 24 hours after scraping the sublimated $Cr(CO)_6$ back into solution from the cooling column. The solution turned to a darker shade of red but further ^{31}P NMR analysis revealed that, while the signal at -60.5 ppm had increased the signal at 20.5 ppm remained quite intense, the additional signals at -42.6 ppm and -27.6 ppm were also still present.

After 5 days some of the solution was found to have precipitated into an orange/red powder. The solution was refluxed and darkened considerably as it did so and was left in reflux condition for an additional two days. At this stage the ^{31}P NMR analysis only revealed a peak at -58 ppm, attributed to the phosphine being ligated to the metal complex. Some minor impurities in ^{1}H NMR were attributed to the $CDCl_3$ used for the NMR sample. The Cr(0) complex is relatively stable, the Cr(0) complex of dppp can even be exposed to atmosphere.

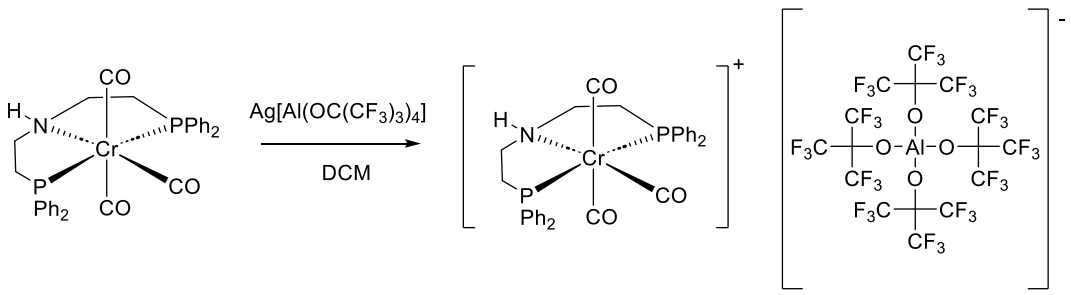

Scheme 5.9: Synthesis of $[Cr(CO)_3(HN(CH_2CH_2PPh_2)_2)]^+[Al(OC(CF_3)_3)_4]^-$.

The final step of the synthesis is to oxidize the complex using $Ag[Al(OC(CF_3)_3)_4]$ silver(tetrakis[perfluoro-tert-butoxy]aluminate), also known as Krossing's salt, as done successfully with $([Cr(CO)_4(dppp)]^+$ following the recommended procedure from this

literature reference [24] and using [25] for additional guidance in adapting the procedure.

The $Ag[Al(OC(CF_3)_3)_4]^-$ salt was found to be brown rather than white, which indicated potential issues such as partial oxidation. It was ultimately decided to continue after a purity test with ^1H, ^{19}F, ^{27}Al proved inconclusive in determining how much the reagent was degraded and acquiring a new batch of reagent was both costly and time consuming.

$Cr(CO)_3(HN(CH_2CH_2PPh_2)_2)$ (557.52 g/mol; 0.112 g; 0.193 mmol) was dissolved in 10 mL of degassed dichloromethane (DCM) and placed in a Schlenk flask. 10 mL of a DCM solution containing the $Ag[Al(OC(CF_3)_3)_4]^-$ salt (1074.96 g/mol; 0.234 g; 0.218 mmol) was added in slight excess to ensure all of the metal complex was oxidized. The solution turned a murky dark-green and was left to stir for 24 hours at room temperature. Ag(0) was removed from the solution using cannula filtration. The dark green solution was tested with ^{31}P NMR but no signal was detected. As the target species is paramagnetic this was actually a promising sign that the desired outcome had potentially been achieved. The ^{19}F spectra collected before and after oxidation indicated only a small change in broadening from 5.6 Hz to 6.7 Hz (expected from literature [25]).

The solution was dried in vacuo to recover a sticky green solid, then redissolved in 3 mL of DCM and filtered with a syringe to remove fine particles of Ag that had escaped the previous filtration step. The solution was dried again and the solid was triturated with hexane (3 x 10 mL) to remove excess oxidant. A yellow solid was recovered after being dried in vacuo and tested with NMR one last time. Once again, ^{31}P NMR yielded no signal, ^{19}F NMR signal displayed a much more noticeable broadening (17.7 Hz), while ^1H NMR also shows the presence of broad signals likely caused by the presence of a paramagnetic species.

5.2.2. Attempted preparation of $[Cr(CO)_3(HN(CH_2CH_2PCy_2)_2)]^+$.

In addition to the above $HN(CH_2CH_2PPh_2)_2$ ligand, a similar attempt was made to prepare another pincer ligand suitable for formation of the Cr(I) complex, namely using $(HN(CH_2CH_2PCy_2)_2)$ (Cy = Cyclohexane). The first stage, removal of HCl proceeded smoothly, following the same procedure reported earlier for $(HN(CH_2CH_2PPh_2)_2)$. However in the subsequent stage, it was ultimately not possible to synthesize the Cr(0)

complex $[Cr(CO)_3(HN(CH_2CH_2PCy_2)_2)]$. During reflux conditions to combine $Cr(CO)_6$ with the ligand $(HN(CH_2CH_2PCy_2)_2)$ it was observed that the solution changed colour to a vivid orange red, visual proof of a reaction occurring. However, every subsequent test with ^{31}P NMR displayed signals very close to that of the free ligand and even extending the reflux phase ultimately did not change the outcome. Additionally, there was no more $Cr(CO)_6$ sublimating on the cooling element, proof that the metal remained in solution as a different species.

Comparing the two ligands with each other it is clear that the major structural difference between the two is how much bulkier the cyclohexyl group is compared to an aryl group. Arene rings are flat and have 5 hydrogen atoms along the same plane occupied by the ring of carbon atoms and the connection point to the phosphorus atom. Cyclohexane rings exist in two structures, neither of which is planar. There are also 11 hydrogens, one of which is on the atom that links the ring to the phosphorus atom. This causes the two ligands to have very different levels of steric hindrance.

The only explanation that could be hypothesized to reconcile the change in colour, the lack of sublimating metal and ^{31}P NMR was that the ligand was only coordinating through its nitrogen atom, with the phosphorus atoms being unable to coordinate and thus, largely magnetically similar to the free ligand. While it was ultimately impossible to synthesize the desired complex this was a reminder of how much this system is affected by steric hinderance as a whole, as can be been seen later when performing reactivity studies on $[Cr(CO)_3(HN(CH_2CH_2PPh_2)_2)]^+$.

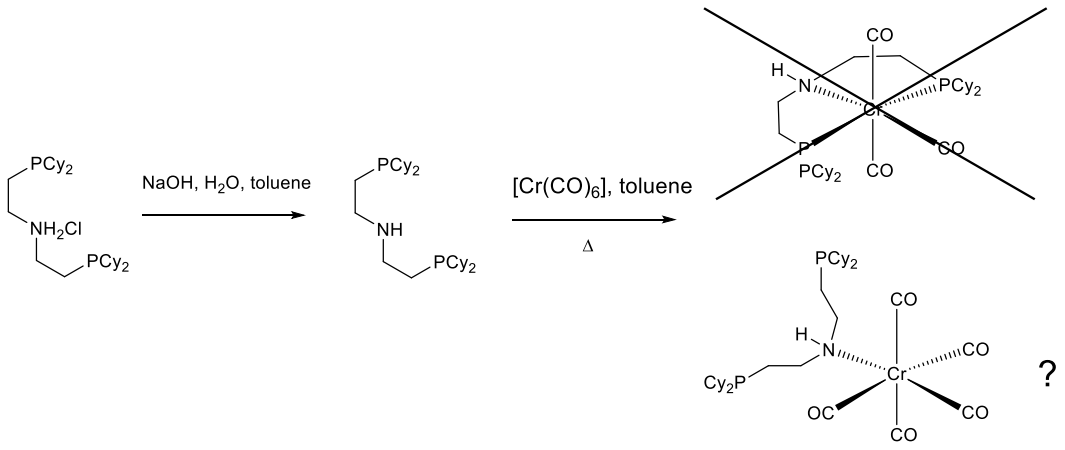

Scheme 5.10: Synthesis of $Cr(CO)_3(HN(CH_2CH_2PCy_2)_2)$.

5.2.3 Sample preparation for EPR/HYSCORE analysis.

Details of the sample preparation stage and EPR instrumentation were given in Chapter 2. Therefore, only a brief summary of the experimental aspects of this work will be presented here.

Sample preparation for EPR measurements: All sample preparations were carried out in an Ar or N_2 glovebox. 4.63 mg of $[Cr(CO)_4(HN(CH_2CH_2\text{-}PPh_2)_2)]^+[Al(OC(CF_3)_3)_4]^-$ (1544.63 g/mol were dissolved in 3 mL of dichloromethane (DCM) to obtain a solution 1 mM of Cr complex in DCM. Preserved at 253 K in a screw cap vial to counter the solvent innate volatility these samples are stable over extended periods of time (at least a year). For EPR analysis Wilmad LPV-7 EPR tubes were used for their airtight caps, found to be reliable up to 24 hours once outside the glove box. Total volume used in EPR samples was 150 µL. Where dilution was necessary, an aliquot was taken from the stock solution inside the glovebox and the requisite amount of DCM added to give a total volume of 150 µL within the EPR tube. Irradiation was performed using different sources in an EPR cavity outfitted with an optical slit. Great care needs to be taken to correctly align the sample to the slit and ensure that all of the volume of the solution is irradiated. When working in frozen solution at low temperature any volume residing within the EPR cavity but not irradiated will keep contributing the signal of the starting complex. Irradiation experiments were conducted using a Labino UVG 2.0 Torch UV LED light source with an output power of 112 mW at the sample (50 nm bandwidth centred at 365 nm). A Labino 505 nm torch from Nova 2.0 ALS Kit. A Scitech Tuneable Light System (TLS) was used for the narrow band irradiation at different wavelengths (2 nm bandwidth with selectable wavelengths between 700 nm and 350 nm).

EPR Instrumentation: The Continuous Wave (CW) EPR spectra were recorded on an CW X-band Bruker EMX spectrometer operating at 100 KHz field modulation frequency, 1 G field modulation amplitude, 10 mW microwave power, and equipped with a high-sensitivity cavity (ER 4119HS). EPR computer simulations were performed using the Easyspin toolbox operating in the Mathworks Matlab environment. HYSCORE experiments were carried out with a Pulse Q- and X-band Bruker E580.

5.3 Results and Discussion

5.3.1 CW-EPR and HYSCORE analysis of the $[Cr(CO)_3(HN(CH_2CH_2\text{-}PPh_2)_2)]^+$ $[Al(OC(CF)_3)_4]^-$ complex

CW-EPR Spectra: Following the successful synthesis of the new Cr(I) complex $[Cr(CO)_3(HN(CH_2CH_2PPh_2)_2)]^+$ from here on referred to as (**6**), the EPR analysis of the compound was performed. The CW X-band spectra of (**6**) recorded at 298 K and 77 K are shown below in Figures 5.1 and 5.2 respectively. The associated simulations are also shown in the corresponding spectra and the resulting spin Hamiltonian parameters are given in Table 5.1. Based on the observed *g* values, with g_{iso} = 2.031, this confirms the presence of the paramagnetic Cr(I) centre. Owing to the broad nature of the isotropic signal, the hyperfine structure from the ^{53}Cr (*I* = 3/2) nucleus is not immediately visible in this instance. However, the presence of ^{53}Cr hyperfine changes the shape of the peaks in Figure 5.1, particularly by adding small extra features at their bases (seen at the field positions of 322 mT and 333 mT). This contribution was observed while simulating the spectra. On the other hand, a well-resolved and dominant (super)hyperfine structure is easily observed and characteristic of two magnetically similar *I* = 1/2 spin centres. A slight deviation from pure axial symmetry could be expected to in (**6**) occur due to the P-C_2H_4-NH-C_2H_4-P backbone not being perfectly aligned along a plane and this potential distortion of the structure away from a perfect octahedron. Indeed, this could be potentially picked up through the ^{31}P a_{iso} values (manifested in the intensity pattern). It is not possible however from the isotropic spectrum alone (and corresponding a_{iso} values) to resolve any differences in the two ^{31}P nuclei. No evidence of any ^{14}N (*I* = 1) interaction could be identified from the room temperature spectrum.

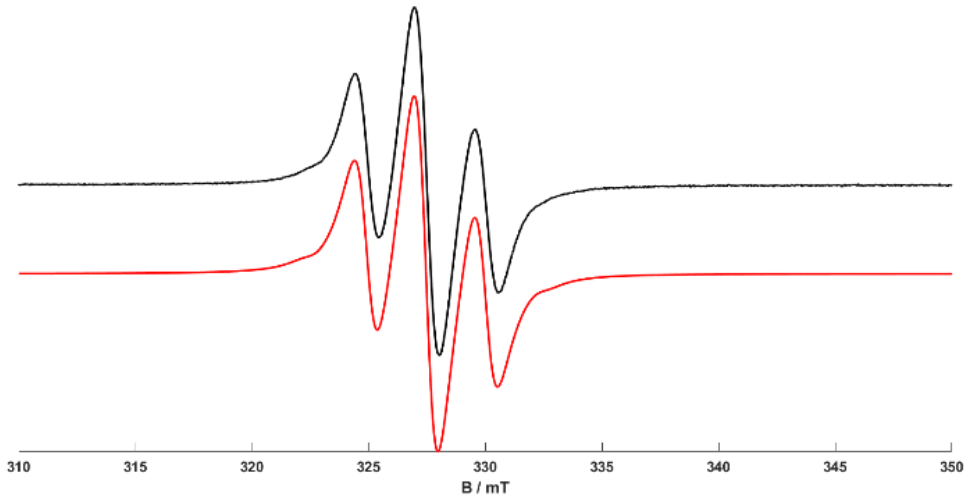

Figure 5.1: CW X-band EPR spectrum (black trace) and simulation (red trace) of the $[Cr(CO)_3(HN(CH_2CH_2PPh_2)_2)]^+$ complex in 1 mM in THF/DCM 3:1 solution recorded at 295 K.

The low temperature (77 K) spectrum is shown in Figure 5.2, and owing to the excellent resolution of the peaks, it is far more informative for extracting detailed insights into the *g* and *A* tensors. At first glance, the spectrum appears to be broadly axial in nature, as expected based on the symmetry of the complex itself. Like in Figure 5.1, the ^{53}Cr hyperfine interaction is not immediately detectable but there are very small peaks before and after the main spectrum that are only visible by including ^{53}Cr hyperfine interaction (seen at 317 mT, 339 mT and 342 mT) in the simulation, the presence of this component also improves the shapes of the peaks to better fit the recorded data. However closer analysis and simulation reveals a slight asymmetry or rhombic character to the **g** matrix values $g_{x,y,z}$ = [2.059, 2.046, 1.990] , (g_{iso} = 2.031), whereby the x, y, z labels are assigned according to the convention $g_x \geq g_y > g_z$. Similar to the spin Hamiltonian parameters described in Chapter 4 for complex (**1**), these new parameters for complex (**6**) are also consistent with a six-coordinate Cr(I) environment displaying strong ligand field splittings between t_{2g} and e_g orbitals and correspondingly the low spin low spin Cr(I) state. The tetragonal distortion away from O_h to D_{4h} symmetry creates the expected ground state, $(d_{xy})^2(d_{xz},d_{yz})^3$ or $(d_{xz},d_{yz})^4(d_{xy})^1$ electron configuration depending on whether the ligand field splitting Δ_{LF} is positive or negative, respectively [26]. Once again, g_x and g_y should be significantly larger than g_e (+ve Δg shift), due to the admixture of the excited state arising from electron promotion from the doubly occupied $d_{xz,yz}$ to the singly occupied d_{xy} orbital. For g_z, a negative *g* shift

is again expected (-ve Δg shift), arising from electron promotion from d_{xy} into the empty d_{x2-y2} orbital. A slight rhombic character ($g_x \neq g_y$) is observed in (**6**) such that g_x = 2.059 and g_y = 2.046) whilst $g_e > g_z$ = 1.990. Nevertheless, this overall confirms the expected d_{xy} ground state of (**6**) and is entirely consistent with the schematic structure illustrated in Figure 5.6 bearing the three CO-Cr-CO, P-Cr-P and N-Cr-CO plane directions.

The *g* matrix depends on the energy of the SOMO, which in turn is affected by the extent of tetragonal distortion in the complex. As a result, any perturbation or changes in the coordination and symmetry of the system will be manifested in the *g* components (as opposed to the ^{31}P couplings). The *g* values for a series of $[Cr(CO)_4\mathbf{L}]^+$ complexes were reported by this group several years ago [27] where L = $Ph_2PN(R)PPh_2$, PNP, or $Ph_2P(R)PPh_2$, PCP). For all these tetracarbonyl complexes a purely axial *g*-matrix was observed with $g_{x,y}$ values falling in the range of 2.089-2.063 and g_z = 1.983-1.987. In the current system $[Cr(CO)_3\mathbf{L}]^+$ (where L = P-C_2H_4-N-C_2H_4), the observed *g* values are of a similar magnitude, with the only difference being the lifting of the equivalency in the $g_{x,y}$ direction where two values are now observed. This is expected based on the structure of (**6**).

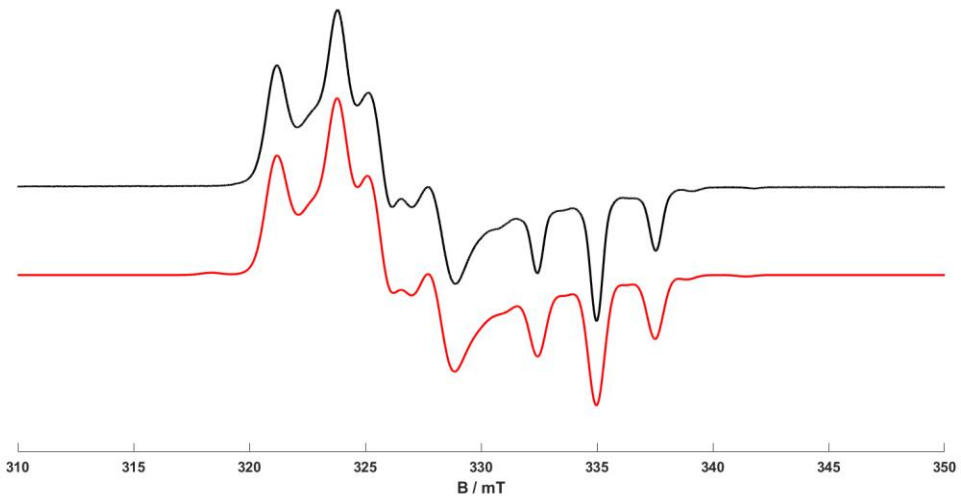

Figure 5.2: CW X-band EPR spectrum (black trace) and simulation (red trace) of the $[Cr(CO)_3(HN(CH_2CH_2PPh_2)_2)]^+$ complex in 1 mM in THF/DCM 3:1 solution recorded at 77 K.

The very distinctive 1:2:1 (super)hyperfine pattern arising from the ^{31}P nuclei, is also observed in the spectrum (Figure 5.2). These isotropic ^{31}P hyperfine couplings arise from the ^{31}P 3s character in the SOMO, from polarisation of inner shell P *s* orbitals by

spin density on the metal or in P 3p orbitals. This summation of all these contributions to the (super)hyperfine can, in principle, be analysed by EPR to account for all of the observed spin densities. As discussed by Rieger *et al.*, [28] reliable interpretation of the ^{31}P hyperfine matrix should be treated carefully as the anisotropies in ^{31P}A are often small and the *g* matrix anisotropy is much greater than the ^{31P}A matrix (hence observed spectral features correspond to orientations of the magnetic field along one of the *g* matrix principal axes). This will depend on the symmetry of the complex. Nevertheless, the ^{31}P a_{iso} values (of 72.3 MHz) observed for (**6**) are very similar to the $^{31P}a_{iso}$ values for the $[Cr(CO)_4\mathbf{L}]^+$ family of complexes (with a_{iso} values (of 78.7 - 70.7 MHz).

Overall, when considering the spin Hamiltonian parameters obtained from the X-band EPR spectra shown above, it can be summarised that the observed *g* and *A* values are entirely consistent with the structure of (**6**) presented in Scheme 5.9. Furthermore, it appears that the electronic properties of the Cr(I) centre, as manifested in the SOMO characteristics and ^{31}P spin densities, are very similar to the tetracarbonyl series of Cr(I) complexes.

HYSCORE Spectra. As discussed in Chapter 2, HYSCORE [29] is a two-dimensional experiment where correlation of nuclear frequencies in one electron spin (m_S) manifold to nuclear frequencies in the other manifold is created by means of a mixing π pulse. X- and Q-band HYSCORE experiments were performed at two different magnetic field settings at both frequencies, corresponding to the “perpendicular” orientation (position 1 in Figure 5.3) at which molecules with their g_z axes oriented perpendicular to the external magnetic field and “quasi-single-crystal” positions (positions in Figure 5.3), where molecules with a narrow sets of orientations of g_z ($\theta \approx$ 0-12°, where θ is the angle between the g_z axes and the external magnetic field) are selected. The specific reason why HYSCORE spectroscopy was performed for this system is to access information about the nitrogen hyperfine interactions, which was not visible in the continuous wave experiments.

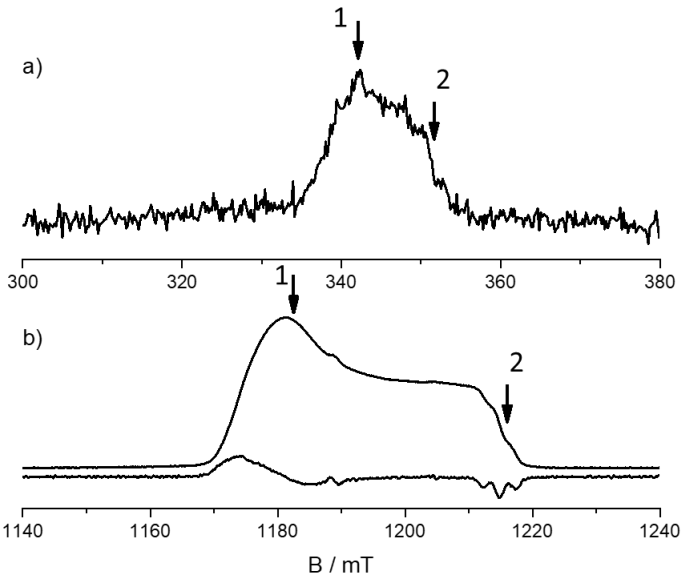

Figure 5.3: a) X-band ESE EPR spectrum of $[Cr(CO)_3(HN(CH_2CH_2PPh_2)_2)]^+$ complex (**6**), 1 mM in DCM solution, ν = 9.748893 GHz, $\pi/2$ = 16 ns, τ = 140 ns. b) Q-band ESE EPR spectrum of the same sample. ν = 33. 7391 GHz $\pi/2$ = 16 ns, τ = 140 ns. Labels 1 and 2 indicate the observer positions taken for the HYSCORE measurements. Both spectra recorded at 30 K.

The X-band HYSCORE spectra (Figure 5.4a and b) show a rich set of cross peaks arising from the interaction of the unpaired electron with ^{14}N (I = 1) and ^{1}H (I = 1/2) nuclei in the local environment. A small ridge in the (+,+) quadrant, centred at the ^{1}H nuclear Larmor frequency, with a width of about 2 MHz is due to the hyperfine interaction with protons of the ligands.

Beside the proton ridge, the spectra show clear correlation peaks in both (-,+) and (+,+) quadrants arising from hyperfine and nuclear quadrupole interactions of the coordinating nitrogen nuclei. For a nuclear spin I = 1 with a substantial nuclear quadrupole interaction, such as ^{14}N, six nuclear frequencies, three in each M_S manifold, are present. Two such frequencies, $\upsilon_{sq1}^{\alpha,\beta}$ and $\upsilon_{sq2}^{\alpha,\beta}$ correspond to single-quantum transitions ($\Delta M_I \pm 1$), whereas the third, $\upsilon_{dq}^{\alpha,\beta}$, is related to the double-quantum transition ($\Delta M_I \pm 2$). Cross peaks can then arise between any nuclear frequency in the α electron spin manifold and any nuclear frequency in the β manifold, including frequencies of transitions with $\Delta M_I \pm 2$.

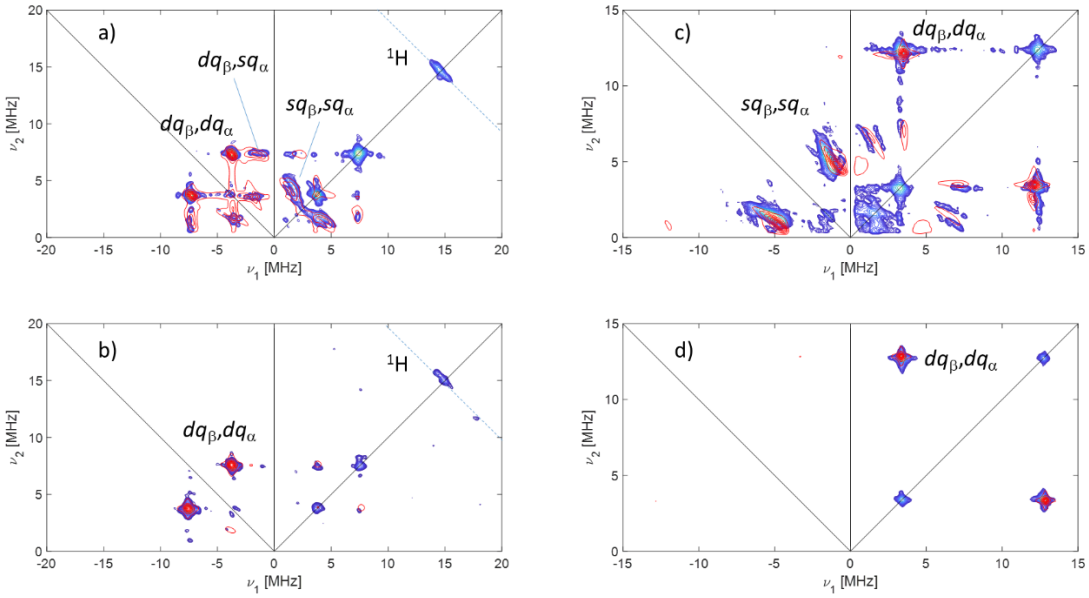

Figure 5.4 Experimental (blue) and simulated (red) HYSCORE experiments of $[Cr(CO)_3(HN(CH_2CH_2PPh_2)_2)]^+$ complex (**6**), 1 mM in DCM solution; a,b) X-band HYSCORE spectra. The spectra reported in Figure 5.4a is the sum of two spectra recorded with two different τ values (τ = 132 ns and τ = 172 ns). The spectra were summed after Fourier transformation in order to avoid blind spot effects. The spectrum reported in Figure 5.4b was recorded with τ = 172; c,d) Q-band HYSCORE spectra recorded with τ = 100 ns. Observer field positions: a) 342.39 mT (position 1 in Figure 3.3a (a)), b) 350.69 mT (position 2 in Figure 3.3a), c) 1181.1 mT (position 1 in Figure 5.3b); d) 1215.0 mT (position 2 in Figure 5.3b). All spectra were recorded at 30 K. All spectra were simulated considering the two spin systems S = 1/2, I = 1 and the same set of spin Hamiltonian parameters listed in Table 5.2.

Some of the cross peaks have been labelled in Figure 5.4. Single-crystal-like spectra are observed at the high-field observer positions at X- and Q-band (positions 2 in Figure 4.3) since only molecules with their $g_{||}$ axis close to $\mathbf{B}_0$ contribute to the spectrum. This results in narrow peaks in the (-,+) quadrant in X-band at (-3.6, 7.6) MHz assigned to double quantum transitions of the form (dq_β,dq_α). At Q-band, where the strong coupling case ($|A|>2|\nu_I|$) holds and these transitions fall in the (+,+) quadrant with values (3.4, 12.7) MHz. The cross peaks between the dq frequencies have frequencies given by:

$$\nu_{\mathrm{dq}}^{\alpha,\beta} = 2\sqrt{\left(\frac{a}{2} \pm \nu_I\right)^2 + K^2(3+\eta^2)} \qquad (5.1)$$

where a is the hyperfine coupling at a given observer position while $K = e^2qQ/4h$ is the quadrupolar coupling constant and η the so-called asymmetry parameter. K and η are

related to the principal values Q_x, Q_y and Q_z of the traceless $\boldsymbol{Q}$ tensor by the following relations: $Q_x = -K(1-\eta)$, $Q_y = -K(1+\eta)$ and $Q_z = 2K$.

Spectra recorded at an observer position corresponding to the $g_{x,y}$ axes along $\boldsymbol{B}_0$ show the presence of ridges associated to bot single and double quantum transitions in both quadrants since in this case the hyperfine interaction is close to the cancellation regime (($|A| = 2|\nu_I|$) at both frequencies.

The data extracted from the analysis of the HYSCORE spectra provide compelling evidence for the coordination of a nitrogen atom approximately in the equatorial plane of the Cr complex lendig support to the structure of $[Cr(CO)_3(HN(CH_2CH_2PPh_2)_2)]^+$ shown in Scheme 5.9.

Table 5.1: Spin Hamiltonian parameters for $[Cr(CO)_3(HN(CH_2CH_2PPh_2)_2)]^+$ derived from X-band CW-EPR.

Compound	g_x	g_y	g_z	^{53}Cr A_1 /MHz	^{53}Cr A_2 /MHz	^{53}Cr A_3 /MHz	^{31}P A_1 /MHz	^{31}P A_2 /MHz	^{31}P A_3 /MHz
$[Cr(CO)_3(PNP)]^+$	2.059	2.046	1.990	-73	-54	-11	-72 -72	-74 -74	-71 -71

Table 5.2: ^{14}N principal hyperfine values (A) and nuclear quadrupole couplings (K) obtained from the simulation of the Spin Hamiltonian parameters for $[Cr(CO)_3(HN(CH_2CH_2PPh_2)_2)]^+$ derived from the simulation of X- and Q-band HYSCORE spectra. A and K are given in units of MHz. β and β' are the Euler angles between A_z and Q_z and the normal plane, for a rotation about the y axis.

$^{N}A_z$	$^{N}A_x$	$^{N}A_y$	β /°	K	η	β' /°
5.3±0.2	4.5±0.4	4.5±0.4	30-70	2.7±0.2	0.9	50-90

5.3.2 Chemical and photochemical transformations of the $[Cr(CO)_3(HN(CH_2CH_2PPh_2)_2)]^+$ with 1-hexene.

The potential chemical and photochemical behaviour of the new complex (**6**) was examined using both the broadband light source and the TLS system, using similar experimental approaches and methodologies to those already described in Chapter 4. Most notably, complex (**6**) did not reveal the formation of any new paramagnetic compounds following UV irradiation only. No photochemical transformations yielding observable paramagnetic complexes could be detected, unlike those described and observed in Chapter 4 for the dppp complex. The results did reveal that prolonged and

continuous UV irradiation of the complex resulted in the overall loss in Cr(I) signal intensity. It is unlikely that a homoleptic equivalent of $[Cr(CO)_2(dppp)_2]^+$ could be formed using the new pincer complex owing to the considerable steric hinderance created by the ligand backbone. Furthermore, formation of such a phototransformed complex would require photoinduced dissociation of the Cr-N bond in addition to the Cr-P and Cr-CO bonds.

It is well known that the $[Cr(CO)_4\mathbf{L}]^+$ type complexes (**L** = $Ph_2PN(R)PPh_2$ or $Ph_2P(R)PPh_2$) can be easily activated using a suitable co-catalyst such as TEA [30]. Therefore, complex (**6**) was exposed to TEA in order to study any possible changes in the resulting EPR spectra. Rather surprisingly no changes where observed in the EPR spectra following treatment of the complex with TEA. The overall intensity of the EPR signal was noted to decrease as a function of added TEA, but without any new paramagnetic species being detected. This is clearly seen in Figure 5.5 below, where the signal diminishes considerably, but no new signals can be identified.

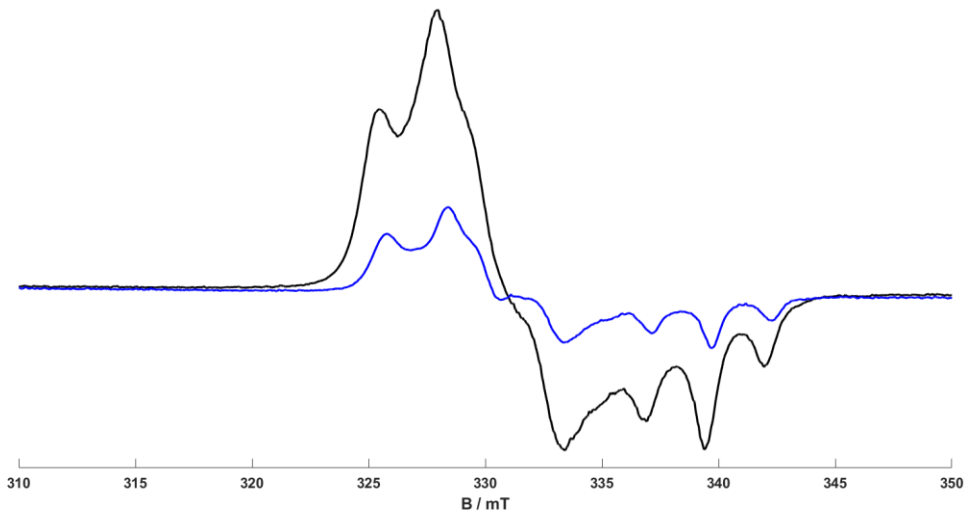

Figure 5.5: CW X-band spectra $[Cr(CO)_3(HN(CH_2CH_2PPh_2)_2)]^+$ at 77 K 1mM in DCM before (black trace) and after (blue Trace) addition of TEA (~50 equivalents in heptane solution).

Therefore, in both chemical and photochemical activation studies, it appears that continued exposure of the new Cr(I) sample to UV light or to increasing equivalents of TEA simply results in more extensive degradation of the starting material. An interesting point to note is that this new complex appears to be more resilient to degradation that compared to (**1**) with multiple instances in which similar amounts of

TEA led to complete obliteration of the EPR signal in (**1**) complex but not in the new (**6**) complex. Once the complex is activated, the intermediates formed may be so unstable, that any traces of residual or intermediate Cr(I) species, are simply too unstable to remain in solution and thus observable by EPR.

The interaction and reactivity of the new complex (**6**) with 1-hexene was next examined. The experimental protocol used in the reactions was similar to that outlined in the previous Chapter; notably a 3:1 solution of 1-hexene and dichloromethane containing 0.33 mM of the Cr(I) complex (**6**) was prepared and the EPR spectrum was recorded. This entire experiment (sample handling) was performed in the dark. No new EPR signals emerged from this solution, *i.e.,* only the EPR spectrum of the starting complex (**6**) was visible. It should be recalled that using complex (**1**), as shown in Chapter 4, that 1-hexene could interact directly with the Cr(I) complex even in dark conditions, albeit yielding only minor amounts of the new Cr(I) 1-hexene complex previously discussed. This 'dark' reaction is clearly not possible with the new Cr(I) pincer complex.

However, when a small quantity of TEA (0.0125 mL) was added to the solution containing the Cr(I) complex plus the 1-hexene, the EPR signal of the starting complex (**6**) was completely transformed and a new EPR signal emerged, indicative of the formation of a new Cr(I) paramagnetic species. This new species $[Cr(CO)_2(HN(CH_2CH_2PPh_2)_2)(1\text{-hexene})]^+$ (**7**) is believed to be structurally similar to (**5**). The resulting EPR signal of this new species recorded at 298 K and 77 K is shown below in Figures 5.6 and 5.7.

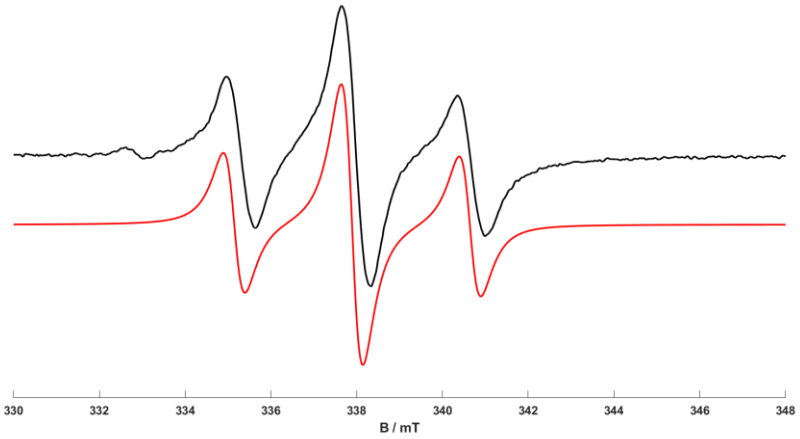

Figure 5.6: CW X-band EPR spectrum and corresponding simulation of the proposed $[Cr(CO)_2(HN(CH_2CH_2PPh_2)_2)(1\text{-hexene})]^+$ (**7**) complex (0.25 mM in 1-hexene/DCM solution 3:1 and TEA; 0.7 mM in heptane at 77 K, ~10 eq. at 295 K).

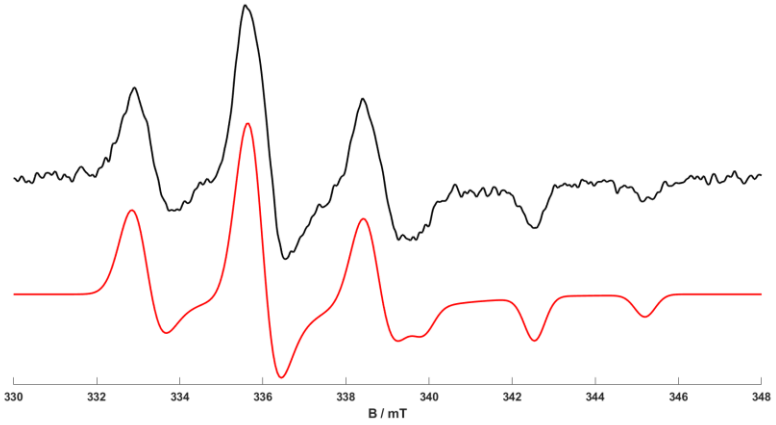

Figure 5.7: CW X-band EPR spectrum and corresponding simulation of the proposed $[Cr(CO)_2(HN(CH_2CH_2PPh_2)_2)(1\text{-hexene})]^+$ (**7**) complex (0.25 mM in 1-hexene/DCM solution 3:1 and TEA; 0.7 mM in heptane at 77 K, ~10 eq. at 295 K).

Owing to the improved resolution of the low temperature spectrum, compared to the room temperature signal, both EPR spectra could be successfully simulated, and the resulting spin Hamiltonian parameters are listed in Table 5.3 below. The significant change in *g* values observed in (**7**) (notably $g_{x,y,z}$ = 2.029, 2.029, 1.999; g_{iso} = 2.019) compared to the original starting complex (**6**) confirms the presence of a new species (Table 5.1 versus 5.3). Owing to the absence of any direct reaction between (**6**) and TEA, one must assume that the new signal formed in the presence of 1-hexene could ostensibly be assigned to a 1-hexene coordinated complex, namely

$[Cr(CO)_2(HN(CH_2CH_2PPh_2)_2)(1\text{-hexene})]^+$ (**7**). The absence of any resolvable ^1H hyperfine from the 1-hexene (diagnostic of 1-hexene coordination in the previous Chapter and confirmed using deuterated 1-hexene) is perhaps not surprising, owing to the importance of steric bulk in the interaction, as indeed observed for some hexene isomers in the previous Chapter. Notably, the bulkier *cis*-2-hexene and *cis*-3-hexene isomers displayed no resolvable hyperfines following coordination with the dppp-based Cr(I) complex. In the current case, the bulky nature of the pincer ligand is likely sufficient to prevent the observable hyperfine interactions.

Owing to the promising nature of the results using TEA to 'activate' a solution bearing the Cr(I) complex and the 1-hexene, attempts were subsequently made to explore whether UV irradiation could also facilitate a similar reaction. Photoactivation of the 1-hexene containing solution was therefore tested under various conditions already considered in Chapter 4, including both low temperature and room temperature conditions. Just to recall, even though exposure of (**6**) to TEA or UV radiation alone did not lead to any observable reactivity (*i.e.*, no new EPR signal), exposure of (**6**) + 1-hexene did result in the formation of a new signal for (**1**) but not for (**6**). Hence the photochemical equivalent experiment was performed. Under low temperture irradiation conditions, no change in the EPR spectrum of the starting complex was observed, *i.e.*, there was no evidence to indicate the photochemical formation of the proposed (**7**) complex. On the other hand, when the irradiation was conducted at room temperature, some changes were indeed noticed in the spectrum. In particular, at least the partial formation of this new 1-hexene coordinated species (**7**) can be identified by simulation. The more interesting fact observed while performing this experiment is that this insertion and coordination step with 1-hexene is observed at long wavelengths (500 nm). However, the reaction appeared to progress more readily when using a shorter and narrower wavelength such as 400 nm. Using a broadband UV torch centred at 505 nm (bandwidth of 50 nm) or a narrow band source at 500 nm (bandwidth of 2 nm), only 10% of the new species was detected (as derived from the composite simulation in Figure 5.8 below).

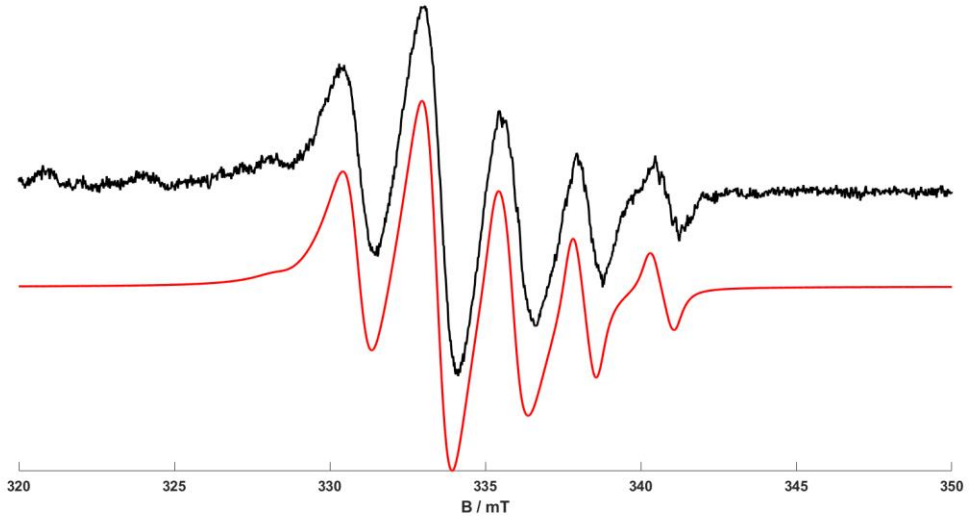

Figure 5.8: CW X-band EPR spectrum and simulation of $[Cr(CO)_3(HN(CH_2CH_2PPh_2)_2)]^+$ (**6**) (simulation weight 90%) and $[Cr(CO)_2(HN(CH_2CH_2PPh_2)_2)(1\text{-hexene})]+$ (**7**) (simulation weight 10%) at 298 K. Conditions: 0.33 mM in 1-hexene/DCM solution 3:1; irradiated for 30 minutes with broad band LED torch at **505 nm** (50 nm bandwidth).

By comparison, Figure 5.9 was obtained after 10 minutes of irradiation at 400 nm with the narrowband source, and the signal of the new 1-hexene complex emerged rather quickly after only 5 to 10 minutes. From that point onward the overall intensity of complex (**7**) did not change markedly but the signal intensity of the precursor instead slowly decreases consistently over the irradiation period (tested with irradiation times of up to 40 minutes).

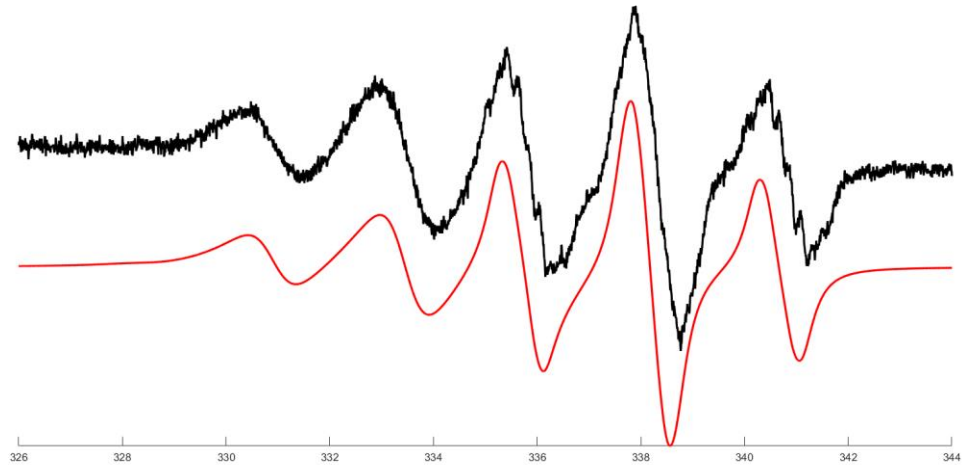

Figure 5.9: CW X-band EPR spectrum and simulation of $[Cr(CO)_3(HN(CH_2CH_2PPh_2)_2)]^+$ (**6**) (simulation weight 70%) and $[Cr(CO)_2(HN(CH_2CH_2PPh_2)_2)(1\text{-hexene})]^+$ (**7**) (simulation weight 30%). Sample irradiated at **400 nm** for ten minutes at 295 K, further irradiation to 40 minutes resulted in only a decreased signal intensity.

As the proposed (**7**) complex appears to be relatively stable (in the absence of continuous UV irradiation) the most likely explanation for how consistent its EPR signal is that there is an equilibrium involved between itself, the precursor and at least one of the EPR silent species that are involved with degradation of the complex that prevents us from building up this species as we were able to do with chemical activation which was more likely to be kinetically driven due to its speed (at least relative to the photochemical pathway).

An important detail that was ultimately not possible to simulate are the small super-hyperfine couplings that are barely visible within the 1:2:1 signal generated by the two ^{31}P nuclei. It is possible that these are the ^{1}H (super)hyperfine couplings visible in (**5**) but due to higher signal to noise ratio, this cannot be said for certain. The reasons why these couplings were not visible when performing the experiment with TEA are not clear, but it is likely due to the linewidth being very sensitive to the concentration of EPR active species and the properties of the solvent making a perfect reproduction of this specific parameter nearly impossible.

Table 5.3: Spin Hamiltonian parameters for $[Cr(CO)_3(HN(CH_2CH_2PPh_2)_2)(1\text{-hexene})]^+$ derived from X-band CW-EPR.

Compound	g_x	g_y	g_z	^{53}Cr a_{iso} /MHz	^{31}P A_1 /MHz	^{31}P A_2 /MHz	^{31}P A_3 /MHz	^{1}H a_{iso1} /MHz	^{1}H a_{iso2} /MHz	^{1}H a_{iso3} /MHz
$[Cr(CO)_2(PNP)(1\text{-hexene})]^+$	2.029	2.029	1.999	-41	-72 -72	-74 -74	-71 -71	<10	<10	<10

5.4 Conclusion

With this series of experiments it was possible to demonstrate that the use of the PNP type ligands for the synthesis of the Cr(I) complex $[Cr(CO)_3(HN(CH_2CH_2PPh_2)_2)]^+$ (**6**) is possible. The resulting EPR and HYSCORE spectra are in agreement with the expected structure of the complex. Structurally, this complex presents itself as a distorted octahedron with a small degree of asymmetry in the *g* tensor and *A* tensors, and this is almost certainly due to being in a *mer-* configuration but the angle between P – N – P formed with the – CH_2CH_2 – linkers does not favour a configuration with the ligand perfectly aligned on one plane. It is possible that a *fac-* configuration would introduce a far greater degree of asymmetry in the EPR data. The small coupling

between the metal centre and the nitrogen present on the ligand seems to indicate that only a small percentage of the spin density is actually present in the N – Cr bond. An interesting consequence of the proposed *mer*- structure is that the three carbonyls (not visible by EPR spectroscopy) are unlikely to have similar properties as two of them find themselves opposite of each other alongside one of the axes of the octahedron while the third is opposing the nitrogen atom of the pincer ligand. Not only will there be an impact from the fact that -CO bonds and N have different effects on the orbitals of opposing bonds (CO is a strong retro-donating group for example) but the large aromatic rings also add steric hinderance to list of considerations. This is particularly evident in that with larger rings such cyclopenthadienyl it was outright impossible to fully coordinate the pincer ligand.

The reactivity of the complex with 1-hexene and the formation of (**7**) has provided greater insights on the wavelengths that affect this system. As expected, TEA was able to selectively remove carbonyl ligands from the complex but without a new species being formed (at least visible by EPR spectroscopy). By using a large excess of 1-hexene in conjunction with TEA activation it was possible to confirm that indeed the complex can be chemically activated, and a new species can be formed (**7**). Of great interest is that when attempting to perform the reaction photochemically it was possible to use light in the 500 nm range which is far less energetic than the 400 nm light needed to activate the CO bonds in the complex bearing the dppp complex. Given the similarities between the two the most likely explanation is that the nitrogen atom has made the carbonyl far more labile for photochemical activation. An interesting observation to be made by comparing the EPR parameters of the starting complex compared to its counterpart coordinating with 1-hexene is that the new species appears to be completely axial. This higher degree of symmetry is probably due to changes in the steric bulk of the new ligand we have introduced pushing the PNP ligand to be better aligned along one plane. By extrapolating from what we have observed with complex (**1**) one can assume that 1-hexene is similarly aligned perpendicularly to the plane of the pincer ligand to keep as much of its aliphatic tail away from the crowded centre.

Bibliography

[1] M. S. Balakrishna, V. S. Reddy, S. S. Krishnamurthy, J. F. Nixon and J. C. B. St Laurent, “Coordination chemistry of diphosphinoamine and cyclodiphosphazane ligands,” *Coordination Chemistry Reviews,* vol. 129, no. 1-2, pp. 1-90, 1994.

[2] M. B. Smith, “The Backbone of Success of P,N-Hybrid Ligands: Some Recent Developments,” *Molecules,* vol. 27, no. 6293, 2022.

[3] G. von Koten and D. Milstein, Organometallic Pincer Chemistry, Springer, 2012.

[4] M. Stradiotto and R. J. Lungdren, Ligand Design in Metal Chemistry: Reactivity and Catalysis, Wiley, 2016.

[5] R. B. King, “Alkylaminobis(difluorophosphines): novel bidentate ligands for stabilizing low metal oxidation states and metal-metal bonded systems,” *Accounts of Chemical Research,* vol. 13, no. 7, pp. 243-248, 1980.

[6] D. S. Payne and A. P. Walker, “Tervalent phosphorus–nitrogen chemistry. Part III. Molybdenum carbonyl complexes of bis(diphenylphosphino)alkylamines,” *Journal of the Chemical Society C: Organic,* no. 0, pp. 498-499, 1966.

[7] A. Carter, S. A. Cohen, N. A. Cooley, A. Murphy, J. Scutt and D. F. Wass, “High Activity Ethylene Trimerisation Catalysts Based on Diphosphine Ligands,” *Chemical Communications,* vol. 2, no. 8, p. 858–859, 2002.

[8] C. M. Hert, J. B. Curley, S. P. Kelley, N. Hazari and B. W. H., “Comparative CO2 Hydrogenation Catalysis with MACHO-type Manganese Complexes,” *Organometallics,* vol. 41, no. 22, pp. 3332-3340, 2022.

[9] A. Mukherjee and D. Milstein, “Homogeneous Catalysis by Cobalt and Manganese Pincer Complexes,” *ACS Catalysis,* vol. 8, no. 12, p. 11435–11469, 2018.

[10] A. Mukherjee, A. Nerush, G. Leitus, L. J. W. Shimon, Y. Ben-David, N. A. Espinosa Jalapa and D. Milstein, “Manganese-Catalyzed Environmentally Benign Dehydrogenative Coupling of Alcohols and Amines to Form Aldimines

and H2: A Catalytic and Mechanistic Study," *Journal of the American Chemical Society,* no. 138, p. 4298– 4301, 2016.

[11] J. B. Curley, C. Hert, W. H. Bernskoetter, N. Hazari and B. Q. Mercado, "Control of Catalyst Isomers Using an N-Phenyl-Substituted RN(CH2CH2PiPr2)2Pincer Ligand in CO2Hydrogenation and Formic Acid Dehydrogenation," *Inorganic Chemistry,* vol. 61, no. 1, pp. 643-656, 2022.

[12] T. Zell and D. Milstein, "Hydrogenation and Dehydrogenation Iron Pincer Catalysts Capable of Metal–Ligand Cooperation by Aromatization/Dearomatization," *Acc. Chem. Res.,* no. 48, p. 1979– 1994, 2015.

[13] I. Bauer and H. J. Knolker, "Iron Catalysis in Organic Synthesis," *Chemical Reviews,* no. 115, p. 3170– 3387, 2015.

[14] P. A. Dub and J. C. Gordon, "The role of the metal-bound N–H functionality in Noyori-type molecular catalysts," *Nature Reviews Chemistry,* vol. 12, no. 2, pp. 396-408, 2018.

[15] T. Zell and R. Langer, "From Ruthenium to Iron and Manganese-A Mechanistic View on Challenges and Design Principles of Base-Metal Hydrogenation Catalysts," *ChemCatChem,* no. 10, pp. 1930-1940, 2018.

[16] X. Zhang, J. Zhang, Z. Hao, Z. Han, J. Lin and G.-L. Lu, "Nickel Complexes Bearing N,N,O-Tridentate Salicylaldiminato Ligand: Efficient Catalysts for Imines Formation via Dehydrogenative Coupling of Primary Alcohols with Amines," *Organometallics,* vol. 40, no. 22, pp. 3843-3853, 2021.

[17] B. M. Ramalingam, I. Ramakrishna and M. Baidya, "Nickel-Catalyzed Direct Alkenylation of Methyl Heteroarenes with Primary Alcohols," *The Journal of Organic Chemistry,* vol. 84, no. 15, pp. 9819-9825, 2019.

[18] S. Lapointe, E. Khaskin, R. R. Fayzullin and J. R. Khusnutdinova, "Nickel(II) Complexes with Electron-Rich, Sterically Hindered PNP Pincer Ligands Enable Uncommon Modes of Ligand Dearomatization," *Organometallics,* vol. 38, no. 22, pp. 4433-4447, 2019.

[19] S. J. Dossett, D. F. Wass, M. D. Jones, A. Gillon, A. G. Orpen, J. S. Fleming and P. G. Pringle, “Steric activation of chelate catalysts: efficient polyketone catalysts based on four-membered palladium(ii) diphosphine chelates,” *Chemical Communications,* vol. 2, no. 8, pp. 699-700, 2001.

[20] M. S. B. Harish S. Kunchur, “Platinum Assisted Tandem P–C Bond Cleavage and P–N Bond Formation in Amide Functionalized Bisphosphine o-Ph2PC6H4C(O)N(H)C6H4PPh2-o: Synthesis, Mechanistic, and Catalytic Studies,” *Inorganic Chemistry,* vol. 61, no. 2, pp. 857-868, 2022.

[21] Z. Han, L. Rong, J. Wu, L. Zhang, Z. Wang and K. Ding, “Catalytic Hydrogenation of Cyclic Carbonates: A Practical Approach from CO2 and Epoxides to Methanol and Diols,” *Angewandte Chemie - International Edition,* vol. 51, no. 52, pp. 13041-13045, 2012.

[22] F. A. Cotton and M. D. LaPrade, “The Crystal and Molecular Structures of [N,N-Bis (2-diphenylphosphinoethyl) ethylamine] - tricarbonylchromium,” *Journal of American Chemical Society,* vol. 91, no. 25, pp. 7000-7005, 1969.

[23] J. Ellermann, M. Moll and N. Will, “Chemie polyfunktioneller moleküle CV. Chrom-, molybdän- und wolframtricarbonyl-komplexe des bis(2-diphenylphosphinoethyl)amins,” *Journal of Organometallic Chemistry,* vol. 378, no. 1, pp. 73-39, 1989.

[24] I. R. A. Krossing, “Chemistry with weakly-coordinating fluorinated alkoxyaluminate anions: Gas phase cations in condensed phases?,” *Coordination Chemistry Reviews,* vol. 250, no. 21-22, pp. 2721-2744, 2006.

[25] A. J. Rucklidge, D. S. Mcguinness, R. P. Tooze, A. M. Z. Slawin, J. D. A. Pelletier, M. J. Hanton and P. B. Webb, “Ethylene Tetramerization with Cationic Chromium(I) Complexes,” *Organometallics,* vol. 26, no. 10, pp. 2782-2787, 2007.

[26] M. Brookhart, W. Chandler, R. J. Kessler, Y. Liu, N. J. Pienta, C. C. Santin, C. Hall, R. N. Perutz and J. A. Timney, “Matrix Isolation and Transient Absorption Studies of (Bis(bis(pentafluoroethyl)phosphino)ethane)tetracarbonylchromium:

Intermolecular Alkane Complexes and Intramolecular F-Coordination," *Journal of the American Chemical Society,* vol. 114, no. 10, pp. 3802-3815, 1992.

[27] L. E. McDyre, T. Hamilton, D. M. Murphy, K. J. Cavell, W. F. Gabrielli, M. J. Hanton and D. M. Smith, "A cw EPR and ENDOR investigation on a series of Cr(i) carbonyl complexes with relevance to alkene oligomerization catalysis: [Cr(CO)4L] + (L = Ph2PN(R)PPh2, Ph2P(R)PPh 2)," *Dalton Transactions,* vol. 39, no. 33, pp. 7792-7799, 2010.

[28] P. H. Rieger, "Electron paramagnetic resonance studies of low-spin d5 transition metal complexes," *Coordination Chemistry Reviews,* Vols. 135-136, no. C, pp. 203-286, 1994.

[29] L. McDyre, E. Carter, K. J. Cavell, D. M. Murphy, J. A. Platts, K. Sampford, B. D. Ward and W. F. Gabrielli, "Intramolecular Formation of a Cr I (bis-arene) Species via TEA Activation of [Cr(CO)4(Ph2P(C3H6)PPh2)]+ : An EPR and DFT Investigation," vol. 30, no. 17, pp. 4505-4508, 2011.

[30] C. M. Hert, J. B. Curley, S. P. Kelley, N. Hazari and W. H. Bernskoetter, "Comparative CO2Hydrogenation Catalysis with MACHO-type Manganese Complexes," *Organometallics,* vol. 41, no. 22, pp. 3332-3340, 2022.

[31] D. M. Murphy and R. D. Farley, "Principles and applications of ENDOR spectroscopy for structure determination in solution and disordered matrices," *Chemical Society Reviews,* vol. 35, pp. 249-268, 2006.

Chapter 6
Conclusions

The spectroscopic technique of Electron Paramagnetic Resonance (EPR) is certainly a powerful, but frequently under-utilised tool in study of paramagnetism in catalysis. The role of paramagnetic states, defects or free radicals are certainly ubiquitous in catalytic reactions, and so EPR becomes the definitive technique to monitor and observe such species. In this Thesis, applications of EPR to provide a deeper understanding of these paramagnetic species relevant to Cr(I) centres is presented and discussed in detail. The motivation of this work was not to develop a new, highly active catalyst for ethylene oligomerisation, but rather to use EPR to explore the plethora of Cr(I) centres that can be formed with such complexes, either by chemical or photochemical treatment. Whilst these new Cr(I) 'intermediate' complexes may not in themselves be relevant to the catalysis, let alone the specific Cr(I) oxidation state, they do demonstrate the variety of centres that can easily form in solution, and thereby could offer insights into the variety of centres formed during the catalysis. The findings and context of this work will be briefly summarised below.

The chemistry of Cr(I) complexes has received sparce scrutiny and attention over the years compared to the other oxidation states of chromium. This is largely due to the combination of its inherent instability and the paramagnetic nature of this oxidation state which are two facets of the same issue. Furthermore in the specific field of ethylene oligomerization chemistry, it is known that both Cr(I) and Cr(III) precursors can deliver similar reaction performances in the catalysis, suggesting that the active species can be derived from either (Cr(I) or Cr(III). For this reason, there is an even lesser tendency to utilise and study the Cr(I) variants of the catalysts. Overall, from an EPR perspective this paramagnetic centre is ideally suited for this spectroscopic technique. With the exception of the initial starting complex $[Cr(CO)_4(dppp)]^+$ (where dppp = $Ph_2P(C_3H_6)PPh_2$) which produced a very weak and broad room temperature signal due to fast spin relaxation processes, most of the EPR spectra for all remaining complexes investigated in this Thesis produced a high quality isotropic spectra (298 K), thereby greatly facilitating the analysis of the low temperature spectra. In many

instances presented in this Thesis, the difficulty in analysing the spectra often arose from the quality of the sample itself rather than any potential difficulty with the spectroscopic setup. Indeed, it was possible to turn even the unfavourable room temperature EPR properties of (**1**) to an advantage as any new species formed was easily detectable even when present in low overall concentration (relative to the precursor). However, as this work and others have identified in Chapter 1, this metal centre is not so unstable as to be unusable and there are examples of catalytically active complexes employed in ethylene oligomerization.

Previous work from the Cardiff group showed how $[Cr(CO)_4(dppp)]^+$ (**1**) could be photochemically transformed into the $[Cr(CO)_2(dppp)_2]^+$ (**2**) and *mer*-$[Cr(CO)_3(\kappa^1$-dppp) $(\kappa^2$-dppp$)]^+$ (**3**) complexes following UV irradiation. By carefully tuning the sample concentration (since the reaction is known to be second order with respect to the starting complex) and wavelength of the UV light, it was possible to not only selectively produce complex (**3**) in this work, but also to obtain an unusual $[Cr(CO)_2(dppp\text{-}\eta^6$-arene$)]^+$ (**5**) complex. This latter complex was previously only ever observed as a very minor species when (**1**) was exposed to very low levels of TEA. However, it was never previously recorded in the photochemical transformations reported for (**1**) and these new results demonstrate for the first time the continuing and enormous potential for the UV photochemistry of (**1**) to form novel Cr(I) complexes by careful control and selection of the wavelength and reaction conditions. From previous published research there is some evidence to suggest that the complex (**1**) is, relatively speaking, not particularly catalytically active for the oligomerization reaction compared to some other Cr(I) diphosphine ligands. However, the ability of 1-hexene to spontaneously coordinate with $[Cr(CO)_4(dppp)]^+$ was somewhat unexpected and may have been facilitated by the large excess of 1-hexene in solution. Following UV irradiation at 400 nm, it was possible to promote the formation of $[Cr(CO)_3(dppp)(1\text{-hexene})]^+$ without displacing the diphosphine ligand. This indicates that formation $[Cr(CO)_3(dppp)(1\text{-hexene})]^+$ following UV radiation indicates that the complex (1) has, at the very minimum, the ability to form a bond with an olefin. This is, understandably, a necessary condition for the catalyst to be catalytically active towards ethylene oligomerization and, as discussed in Chapter 1, at least three of these molecules must be able to form a ring (metalacyclic process) which then detaches as 1-hexene. Therefore, these results offer a promising opportunity to explore further the use of UV

irradiation to enhance, or compliment, the catalysis by Cr(I) complexes use in the presence of other cocatalysts.

Similarly, with the new pincer type Cr(I) complex, $[Cr(CO)_3(Ph_2P(C_2H_4))_2NH)]^+$ (**6**) it was possible to demonstrate that these complexes can be successfully synthesized and that they can also chemically and photochemically react with 1-hexene. The synthesis of complex (**6**) and the unsuccessful synthesis of $[Cr(CO)_3(Cy_2P-(C_2H_4))_2NH)]^+$ offer another example of adapting well established synthetic procedures that proved successful with other metal centres and also give tangible evidence on the importance of steric hinderance for these species.

From these photoreactivity studies it is clear that narrowband UV irradiation has the potential to be selective with regards to which Cr-P or Cr-CO bonds are activated. In particular, 400 nm appears to be the optimal wavelength for activating selectively the Cr–CO bond in complex (**1**) without affecting the Cr-P bond in the diphosphino ligand. This is a very important finding, since the broadband UV light source is known to simultaneously break both Cr-CO and Cr-P bonds leading to a 'scrambling' of the ligands and the resulting formation of the homoleptic complex (**2**). For complex (**6**) by comparison it appears that at least one of the Cr–CO bonds can be activated with UV light at 505 nm, suggesting that the nitrogen atom can have a profound impact on the energy of photolabile Cr–CO bonds. As the formation of complex (**3**) has shown, the photolabile nature of the Cr–CO bonds can change even during the course of the reaction itself, as the wavelength dependency experiments in this Thesis have shown (*i.e.*, 380 nm versus 365 nm).

The catalytic reactions involving the Cr(I) complexes (**1**) and (**6**) were not investigated in this Thesis (the facilities to perform the catalytic test reactions were not available the laboratories). Clearly a logical continuation of the work presented in this Thesis would be to perform such catalytic studies under UV illumination conditions. As the studies with (**6**) have shown, unless the complex can perform intra or inter molecular reactions with itself there is no way to detect activated Cr – CO bonds as these will simply break and reform constantly if no other species can enter. This ultimately leads to degradation of the complex.

If a successful alternative to chemical activation with TEA or MMAO could be found, or even if simultaneous UV irradiation can enhance the catalytic activation step and

thereby reduce (rather than eliminate) the high quantities of TEA/MMAO required, it would possibly make ethylene oligomerization a far cleaner reaction by removing the necessity for a heavily polluting and pyrophoric reagent which cannot be easily reused. Investigations along this reaction might also yield a better understanding of the activation process as, unlike TEA which causes a wide range of reactions, it is possible to be more selective in the application of light, thus allowing the potential to study some of the steps individually.

Finally, and more generically, the application of EPR to better identify and characterise the variety of intermediate complexes that these Cr(I) centres can produce was clearly demonstrated in this Thesis. The outcome of this work illustrates the rich diversity of paramagnetic states, which could be critical for the function of the Cr(I) based catalysts. Through careful experimental design and execution, EPR is shown to provide a detailed understanding of the wavelength dependency to the photochemical reactions, and the facile ability of a simple alkene (1-hexene) to coordinate with the metal complex. This information would not be easily obtained by other spectroscopic techniques.